RISC-KIT

Resilience-Increasing Strategies for Coasts – Toolkit

www.risckit.eu

Improvement of physical processes

XBeach improvement & validation; wave dissipation over vegetated marshes and flash flood module

Deliverable No: D.3.2 – Updated physical models
Ref.: WP3 - Task 3.2
Date: April 2015

Grant Agreement No. 603458
DG Research –FP7-ENV-2013-two-stage

This project has received funding from the European Union's Seventh Programme for Research, Technological Development and Demonstration under Grant Agreement n° [603458]. This publication reflects the views only of the author's, and the European Union cannot be considered liable for any use that may be made of the information contained therein.

Deliverable Title	D.3.2 – Updated physical models
Filename	RISCKIT_D.3.2_Improvement of Physical Processes v11
Authors	Dano Roelvink (UNESCO-IHE) Ali Dastgheib (UNESCO-IHE) Tom Spencer (UCAM) Iris Möller (UCAM) Elizabeth Christie (UCAM) Marc Berenguer (UPC-CRAHI) Daniel Sempere-Torres(UPC-CRAHI)
Contributors	Jentsje van der Meer (UNESCO-IHE) Seyyedabdolhossein Mehvar (UNESCO-IHE) Kees Nederhoff (Deltares) Willem Vermin (SURF-SARA)
Date	30/04/2015

Prepared under contract from the European Commission
Grant Agreement No. 603458
Directorate-General for Research & Innovation (DG Research), Collaborative project, FP7-ENV-2013-two-stage

Start of the project: 01/11/2013
Duration: 42 months
Project coordinator: Stichting Deltares, NL

Dissemination level

X	PU	Public
	PP	Restricted to other programme participants (including the Commission Services)
	RE	Restricted to a group specified by the consortium (including the Commission Services)
	CO	Confidential, only for members of the consortium (including the Commission Services)

Deliverable status version control

Version	Date	Authors	Review
1.0	24/04/2015	Dano Roelvink (UNESCO-IHE) Ali Dastgheib (UNESCO-IHE) Tom Spencer (UCAM) Iris Möller (UCAM) Elizabeth Christie (UCAM) Marc Berenguer (UPC-CRAHI) Daniel Sempere-Torres(UPC-CRAHI)	Robert McCall (Deltares) Ap van Dongeren (Deltares)

2.0	30/04/2015	Dano Roelvink (UNESCO-IHE) Ali Dastgheib (UNESCO-IHE) Tom Spencer (UCAM) Iris Möller (UCAM) Elizabeth Christie (UCAM) Marc Berenguer (UPC-CRAHI) Daniel Sempere-Torres(UPC-CRAHI)	Ap van Dongeren (Deltares)

Table of Contents

1 INTRODUCTION 2

1.1 PROJECT OBJECTIVES 2
1.2 PROJECT STRUCTURE 3
1.3 DELIVERABLE CONTEXT AND OBJECTIVE 5
1.4 APPROACH 6
1.5 OUTLINE OF THE REPORT 9

2 IMPROVEMENT AND VALIDATION OF THE TWO-DIMENSIONAL MORPHOLOGICAL MODEL XBEACH 10

2.1 INTRODUCTION 10
2.2 IMPROVING THE COMPUTATIONAL EFFICIENCY 11
2.2.1 Improving MPI parallel implementation 11
2.2.2 Implementing cyclic lateral boundary conditions 17
2.2.3 Improving the efficiency of directional wave energy propagation 18
2.3 DEVELOPMENTS AND VALIDATION OF NON-HYDROSTATIC MODEL 19
2.3.1 Validation of wave run-up: Petten case 19
2.3.2 Validation with Clash database 28
2.3.3 Developing morphological non-hydrostatic model 32
2.4 DEVELOPMENTS AND VALIDATION (2D HYDRODYNAMIC FIELD VALIDATION) 36
2.4.1 Delilah field test 36
2.4.2 Praia de Faro, Vousdoukas et al. 43
2.4.3 Conclusions on 2DH hydrodynamic validation 50
2.5 DEVELOPMENTS AND VALIDATION (2D MORPHODYNAMIC) 51
2.5.1 Hurricane Sandy (2012) 51
2.5.2 Fire Island 52
2.5.3 Camp Osborne 54
2.5.4 Conclusions on 2DH morphodynamic validation 57
2.6 MAIN FINDINGS AND RECOMMENDATIONS 57
2.7 REFERENCES 58

3 DEVELOPMENT AND VALIDATION OF HIERARCHICAL MODELS OF STORM WAVE ENERGY DISSIPATION 60

3.1 INTRODUCTION 60

3.2 IMPLEMENTING A MODIFIED WAVE DISSIPATION MODEL DUE TO VEGETATION BASED ON EMPIRICAL FORMULAE 61
3.2.1 Modified SWAN-VEG module for saltmarsh 64
3.3 VALIDATION FOR THE MODIFIED SWAN-VEG MODULE 65
3.3.1 Validation of wave dissipation (intermediate spatial scale) due to vegetation within a wave flume 65
3.3.2 Validation of a wave dissipation due to vegetation along a salt marsh transect (large scale) 67
3.3.3 Validation of wave dissipation due to vegetation over three saltmarsh transects with different vegetation characteristics (small scale) 70
3.4 FINDINGS AND RECOMMENDATIONS 72
3.5 REFERENCES: 73
4 DESCRIPTION OF THE FLASH FLOOD MODULE FF-EWS 76
4.1 INTRODUCTION 76
4.2 FF-EWS 76
4.3 RAINFALL ESTIMATION AND FORECASTING 78
4.3.1 Rainfall estimation 78
4.3.2 Rainfall forecasts 78
4.4 RETRIEVAL OF THE DRAINAGE NETWORK 79
4.5 FLASH FLOOD HAZARD ASSESSMENT 80
4.5.1 Constructing a climatology of aggregated daily rainfall accumulations for FF hazard assessment. 80
4.5.2 Disaggregation of daily values 88
4.5.3 Flash flood hazard assessment 88
4.6 EXAMPLES IN THE TORDERA DELTA CASE STUDY SITE 88
4.7 RECIPE FOR THE EXTENSION OF THE MODULE TO A NEW DOMAIN – REQUIREMENTS FOR ITS APPLICATION TO THE BOCCA DI MAGRA CASE STUDY SITE 96
4.8 DESCRIPTION OF THE EXCHANGE PRODUCT TO BE DISPLAYED IN FEWS 97
4.9 SUMMARY AND CONCLUSIONS 100
4.10 REFERENCES 100

List of Figures

Figure 1.1: Conceptual drawing of the CRAF (top panel), the EWS (middle panel) and the DSS (bottom panel) 4

Figure 1.2: Case study sites (stars), RISC-KIT case study site partners (blue solid dots) and non-case study site partners (red open circles) 5

Figure 2.1 Communication of two rows and columns between domains using MPI. The areas within the thick drawn lines are where the full computations are carried out. 13

Figure 2.2 Predicted short wave pattern for the test case 'Port_fine' 15

Figure 2.3 Speedup of the new code compared to the original code. 16

Figure 2.4 Timing (in CPUs) of the new code compared to the old code. 16

Figure 2.5 Speedup for Port_fine_surfbeat case on Cartesius 17

Figure 2.6 Example of use of cyclic boundaries, non-hydrostatic wave model for Albufeira 17

Figure 2.7 Snapshots of slowly-varying wave height (top panels) and water level (bottom panels) for non-hydrostatic mode (left), single_dir mode (middle) and multi-dir mode 19

Figure 2.8 *Measured foreshore perpendicular to the Petten Sea-defense* 20

Figure 2.9 Schematized foreshore for model tests 21

Figure 2.10 Schematized structure for model tests 21

Figure 2.11 Predicted R2% by XBeach compared to the physical models of Petten tests, based on different wave conditions 22

Figure 2.12 Experimental setup of wave transformation and wave overtopping on the Wenduine sea dike (SWL =6.84m TAW, 1:25 scale) 23

Figure 2.13 Comparison of wave spectra for station 1 26

Figure 2.14 Comparison of wave spectra for station 5 26

Figure 2.15 Comparison of wave spectra for station 6 26

Figure 2.16 Model geometry (top panel), Hm0 wave height (middle panel) and peak period (bottom panel) for XBeach (drawn lines) and the physical model (dots); sensitivity for parmeter maxbrsteep. 27

Figure 2.17 Instantaneous overtopping discharge at end of the crest 27

Figure 2.18 Snapshot of water elevation during an overtopping event 28

Figure 2.19 Analysis of incoming, reflected and total wave heights in numerical experiment; Hm0 refers to total wave signal; Hm0tot is based on the sum of the incident and reflected wave energy. 30

Figure 2.20 Comparison of measured and simulated mean overtopping discharges for all selected cases; results scaled up to prototype scale. 31

Figure 2.21 Comparison of measured and simulated mean overtopping discharges for all cases in Victor et al. (2011); results scaled up to prototype scale. 31

Figure 2.22 Comparison of profile evolution between surfbeat and nonhydrostatic approaches, LIP11D test 2E. 33

Figure 2.23 Comparison of profile evolution between surf-beat and non-hydrostatic approaches, Tordera barrier, Spain. 34

Figure 2.24 Example calibration of profile behavior 36

Figure 2.32 The bathymetry and measurement locations of Delilah 38

Figure 2.33 Spatial plot of the room-mean-square short wave height for a multi_dir and single_dir simulation. 39

Figure 2.35 Comparison of the root-mean-square wave height (Hrms) for Delilah for both the high frequency part (upper panel) and the low frequency part (middle panel) for multiple simulation types as computed by XBeach (solid lines); default: multi-dir; single=2: single_dir, 2nd order scheme; single=1: single_dir with 1st order scheme; non-hydro: non-hydrostatic model. 41

Figure 2.36 The high frequency waves (top panel), low frequency waves (middle panel) and VLF waves (lower panel) presented for a single direction (single_dir=1) simulation in XBeach for Delilah 43

Figure 2.25 base, mildest and steepest profile for simulations 45

Figure 2.26 Simulations for Vousdoukas et al, 1D non-hydrostatic mode. Panels from top to bottom: Hs wave height, Tp wave period, mean wave direction (not used in 1D), water level, beach slope in swash zone, R2% run-up height 46

Figure 2.27 Observed vs simulated R2% run-up height and regression curves; 1D non-hydrostatic 47

Figure 2.28 Simulations for Vousdoukas et al, 1D surf-beat mode. Panels from top to bottom: Hs wave height, Tp wave period, mean wave direction (not used in 1D), water level, beach slope in swash zone, R2% run-up height 48

Figure 2.29 Observed vs simulated R2% run-up height and regression curves; 1D surf-beat. 48

Figure 2.30 Simulations for Vousdoukas et al, 2D surf-beat mode. Panels from top to bottom: Hs wave height, Tp wave period, mean wave direction, water level, beach slope in swash zone, R2% run-up height 49

Figure 2.31 Observed vs simulated R2% run-up height and regression curves; 2D surf-beat. 50

Figure 2.37 Track of Hurricane Sandy. Traveling from South to North Sandy interacted with a nontropical weather system transforming from hurricane to a post-tropical cyclone. Colors from blue to red represents hurricane intensity. [Sources: National Hurricane Center (2012) and Wikipedia 52

Figure 2.38 Aerial photo prior to (left; July 3rd 2012) and after (right; November 4th 2012)the hurricane (Source: Google Earth) 52

Figure 2.39 Spatial post bed levels and erosion/accretion plots after the storm event presented for the area of interest at Fire Island. Spots without data are marked grey. The black depth contours are provided at an elevation of 0 and 3m relative to NADV88.....53

Figure 2.40 Post bed levels for various cross-sections: pre-Sandy, post-Sandy and calculated for multi_dir and single_dir for Fire Island. The legend is valid for all individual subfigures. Note: the profiles for multi_dir and single_dir are quite similar. ..54

Figure 2.41 Pre- and post-storm oblique aerial photographs of the impact of Hurricane Sandy (2012). Pictured is a condo in the barrier of Camp Osborne, Brick, NJ. Pictures are taken on the 21st of May 2009 and the 05th of November 2012. Taken from the U.S. Geological Survey (USGS) website. 55

Figure 2.42 Spatial post bed levels and erosion/accretion plots after the storm event presented for the area of interest at Camp Osborne. Spots without data are marked grey. The black depth contours are provided at an elevation of 0 and 3m relative to NADV88. 55

Figure 2.43 Post bed levels for various cross-sections: pre-Sandy, post-Sandy and calculated for multi_dir and single_dir for Camp Osborne. The legend is valid for all individual subfigures. Note1: the peaks in the profiles (mainly y < 400m) seem unrealistic and are related to the avalanching algorithm. Note2: the profiles for multi_dir and single_dir are quite similar. 56

Figure 3.1 Upper panel: Experimental test-section in the Large Wave Flume (Grosser Wellenkanal, GWK) (from Möller et al., 2014). Lower panel: view of the vegetated test section at the mid-point in construction, looking towards the wave paddle (photo: I Möller).....65

Figure 3.2 Normalised significant wave height reduction across a saltmarsh under storm conditions in a wave flume. Wave height measurements (Moller et al. 2014) are compared against predicted values using a SWAN model with a fixed and varying drag coefficient.....66

Figure 3.3 Location of the Stiffkey saltmarsh, North Norfolk (from Möller et al., 1999) 66

Figure 3.4 Upper panel; View of 'low' marsh, Stiffkey, North Norfolk, looking seawards (photo: T Spencer). Lower panel: section across Stiffkey marshes. Transect lies between 'inner' and 'middle' station on the 'low' marsh (from Möller et al. 1999) 67

Figure 3.5 Black/white ground level, horizontal photograph of late summer (September) vegetation community structure on the 'low' marsh at Stiffkey, c. 100 m landward from the marsh edge (from Möller et al. 1999).....68

Figure 3.6 Normalized significant wave height reduction across a saltmarsh transect (Figure 3.4; 'Middle' to 'Inner' stations) with different wave conditions. Wave height measurements by Moller et al. (1999) are compared against predicted values from the adapted SWAN-VEG module 69

Figure 3.7 Spatially varying vegetation height over three saltmarsh transects in Tillingham, Essex. 70

Figure 3.8 Normalised significant wave height reduction across three transects with differing vegetation characteristics. Measured wave height by Moller (2006) are compared against predicted values using the adapted SWAN-VEG module. a) fixed vegetation height in SWAN, b) spatially varying vegetation height in SWAN. 71

Figure 4.1 Area where the FF-EWS module has been implemented. The small dark blue arrows indicate the retrieved drainage network. The thin yellow contour indicates the limits of the Tordera catchment (865 km^2). The coastal streams correspond to Riera de Calella, Riera de Pineda, Riera de Santa Susanna, Riera de Palafolls, Torrent de la Burgada, Torrent de can Rabasa, Riera de Passapera and Riera de Lloret (1-8). 79

Figure 4.2 First four principal components of the daily rainfall accumulations estimated over the analysis domain (normalized eigenvectors of the covariance matrix; arbitrary units). The explained variance is indicated in each panel. 81

Figure 4.3 Cumulative explained variance as function of the number of principal components. The red lines indicate the number of components (25) needed to explain a variance of 90%. 82

Figure 4.4 Description of a given rainfall field (daily accumulation for 10 May 2008) as a function of the number of principal components used in equation (4.4). (a) Estimated daily accumulation; (b-e) Filtered field for values of L=1, 4, 15, 78, respectively. The number on the upper right corner of panels b-e indicates the explained variance of the original rainfall accumulation. 83

Figure 4.5 Historical evolution (1940-2010) of the rain gauge network used for the reconstruction of an improved climatology of daily rainfall accumulations in the area of study. 83

Figure 4.6 Illustration of the reconstruction method for the rainfall accumulation of 20 April 2007. (a) Reference field obtained with the radar-rain gauge blending method of Velasco-Forero et al. (2009), which is used as reference. (b) Rainfall field obtained using the first L=25 principal components in equation (4.4). (c) Field obtained using thin-plate splines to interpolate the (k=15) observations in the locations indicated with the red dots. (d) Same as (c), but with the proposed reconstruction method. In the bottom right corner of panels (c) and (d), E and C indicate the values of Nash efficiency and correlation obtained from the point-to-point comparison with the reference field of panel (a). 85

Figure 4.7 Example of the reconstruction of the daily accumulations for the flash-flood-producing precipitation events of 09 October 2002 (left) and 13 October 2005(right). Upper row: Reference daily accumulation obtained with the radar-rain gauge blending method of Velasco-Forero et al. (2009). Middle row: fields reconstructed with the proposed method (the white triangles indicate the locations of the available rain gauges). Bottom row: Scatter plots between the values of the reconstructed and the reference fields. 86

Figure 4.8 Rainfall accumulations for the two events analyzed (23-24 September 2010 and 23-24 October 2011). Left: Radar-based accumulations (the circles indicate the accumulations observed at rain gauge locations). Right: Scatter plot between collocated radar-based accumulations and rain gauge observations. 88

Figure 4.9 Pictures of the areas flooded in Malgrat de Mar (a, b) and Pineda (c, d) on 24 September 2010. Source: El Punt Diari (a, b), www.tv3.cat (c, d). 89

Figure 4.10 Summary of the performance of the FF-EWS module applied to the Tordera Delta case study site for the event of 23 September 2010. (a) Rainfall accumulation obtained with the radar-based QPE products. (b) Maximum return period estimated with the FF-EWS module along the event. 90

Figure 4.11 Estimated rainfall intensity and hazard level obtained with the FF-EWS module on 24 September 2010 at 16:00 (left) and 16:30 UTC (right). 91

Figure 4.12 Same as Fig. **4.10**, but for the event of 23-24 October 2011. 92

Figure 4.13 Pictures of the areas flooded in Blanes on 24 October 2011. Source: Dolors Ruiz and Victor Catalan Casas (www.facebook.com) 93

Figure 4.14 Same as Fig. **4.11**, but for 24 October 2011 at 05:00 and 05:30 UTC. 94

List of Tables

Table 2.1: Name of the table Characteristics of the prototype cases of Petten sea defense and the resulted wave run-up level predicted by XBeach 22

Table 2.3 Test characteristic for the physical model that is reproduced by XBeach 24

Table 2.4 Numerical parameters used in ''params.txt'' file for the preliminary scale case 1A 25

Table 2.5 Mean wave overtopping results in combined sensitivity analysis of Chezy coefficient and maximum wave breaking steepness parameter 28

Table 2.6 Comparison of the results for Delilah 40

Table 2.7 Comparison for the result for Delilah for the different wave breaking formulations 42

Table 3.1 Test conditions for the large-scale wave energy dissipation modeling from wave conditions measured at the Middle Station on the saltmarsh transect at Stiffkey, North Norfolk (Figure 3.4; Moller et al., 1999). 68

Table 3.2 Measured and derived vegetation characteristics at three saltmarsh transects in Tillingham, Essex (Moller 2006) 70

Executive and Publishable Summary

This report is part of D3.2 and consists of validation document and description for new XBeach developments, the description of the numerical formulation for storm wave energy dissipation modeling implemented in SWAN, and the description of the improved flash flood module and its integration in the Coastal FEWS platform.

In the framework of the WP3 of RISC-KIT project XBeach has been further developed to improve the computational speed of the model as well as the physical descriptions to enhance the accuracy and reliability. This includes:improving the MPI parallel implementation, implementing cyclic lateral boundary conditions, improving the efficiency of directional wave energy propagation, and developing a morphological non-hydrostatic model. The developments are validated and tested for field situations and engineering applications. In the second part, a new formulation for estimating the wave energy dissipation over vegetation in coastal areas is implemented in SWAN model and validated against flume tests and field measurements. Finally, the flash flood model developed in the FP7 project IMPRINTS is improved by increasing the resolution and better estimation of the hazard level. The improved model is applied around the Tordera Delta in Spain (a RISC-KIT case study site) successfully and an implementation recipe is made available. The flash flood hazard assessment products are now displayable in free-ware Coastal FEWS system which is developed as part of Work Package 3 of RISC-KIT project (Deliverable 3.1).

The improved physic based models and new developments (Codes) delivered in this task are made available through the open source and free software community web portal (www.oss.deltares.nl), with links from the project website www.riskkit.eu and will be used in case study sites in the WP5 of RISC-KIT Project.

1 Introduction

Recent and historic low-frequency, high-impact events such as Xynthia (impacting France in 2010), the 2011 Liguria (Italy) Flash Floods and the 1953 North Sea storm surge which inundated parts of the Netherlands, Belgium and the UK have demonstrated the flood risks faced by exposed coastal areas in Europe. Typhoons in Asia (such as Typhoon Haiyan in the Philippines in November 2013), hurricanes in the Caribbean and Gulf of Mexico, and Superstorm Sandy, impacting the northeastern U.S.A. in October 2012, have demonstrated how even larger flooding events pose a significant risk and can devastate and immobilize large cities and countries.

These coastal zone risks are likely to increase in the future (IPPC, AR5) which requires a re-evaluation of coastal disaster risk reduction (DRR) strategies and a new mix of prevention (e.g. dike protection), mitigation (e.g. limiting construction in flood-prone areas; eco-system based solutions) and preparedness (e.g. Early Warning Systems, EWS) (PMP) measures. Even without a change in risk due to climate or socio-economic changes, a re-evaluation is necessary in the light of a growing appreciation of ecological and natural values which drive ecosystem-based or Nature-based flood defense approaches. In addition, as free space is becoming sparse, coastal DRR plans need to be spatially efficient, allowing for multi-functionality.

1.1 Project objectives

In response to these challenges, the RISC-KIT project aims to deliver a set of open-source and open-access methods, tools and management approaches to reduce risk and increase resilience to low-frequency, high-impact hydro-meteorological events in the coastal zone. These products will enhance forecasting, prediction and early warning capabilities, improve the assessment of long-term coastal risk and optimise the mix of PMP-measures. Specific objectives are:

1. Review and analysis of current-practice coastal risk management plans and lessons-learned of historical large-scale events;
2. Collection of local socio-cultural-economic and physical data at case study sites through end-user and stakeholder consultation to be stored in an impact-oriented coastal risk database;
3. Development of a regional-scale coastal risk assessment framework (CRAF) to assess present and future risk due to multi-hazards (**Figure 1.1**, top panel);
4. Development of an impact-oriented Early Warning and Decision Support System (EWS/DSS) for hot spot areas consisting of: i) a free-ware system to predict hazard intensities using coupled hydro-meteo and morphological models and ii) a Bayesian-based Decision Support System which integrates hazards and socio-economic, cultural and environmental consequences (**Figure 1.1**, centre panel);
5. Development of potential DRR measures and the design of ecosystem-based and cost-effective, (non-)technological DRR plans in close cooperation with end-users for a diverse set of case study sites on all European regional seas and on one tropical coast (**Figure 1.1**; bottom panel);

6. Application of CRAF and EWS/DSS tools at the case study sites to test the DRR plans for a combination of scenarios of climate-related hazard and socio-economic vulnerability change and demonstration of the operational mode;
7. Development of a web-based management guide for developing integrated DRR plans along Europe's coasts and beyond and provide a synthesis of lessons learned in RISC-KIT in the form of policy guidance and recommendations at the national and EU level.

The tools are to be demonstrated on case study sites on a range of EU coasts in the North- and Baltic Sea Region, Atlantic Ocean, Black Sea and Mediterranean Sea, and one site in Bangladesh, see Figure **1.2**. These sites constitute diverse geomorphic settings, land use, forcing, hazard types and socio-economic, cultural and environmental characteristics. All selected regions are most frequently affected by storm surges and coastal erosion. A management guide of PMP measures and management approaches will be developed. The toolkit will benefit forecasting and civil protection agencies, coastal managers, local government, community members, NGOs, the general public and scientists.

1.2 Project structure

The project is structured into seven Work Packages (WP) starting with WP1 on 'Data collection, review and historical analysis'.; WP2–4 will create the components of the RISC-toolKIT containing an 'Improved method for regional scale vulnerability and risk assessment' (WP2), 'Enhanced early warning and scenario evaluation capabilities for hot spots' (WP3) as well as 'New management and policy approaches to increase coastal resilience' (WP4). The toolkit will be tested through 'Application at case study sites' (WP5). WP6 will be responsible for 'Dissemination, knowledge transfer and exploitation' and 'Coordination and Management' are handled in WP7.

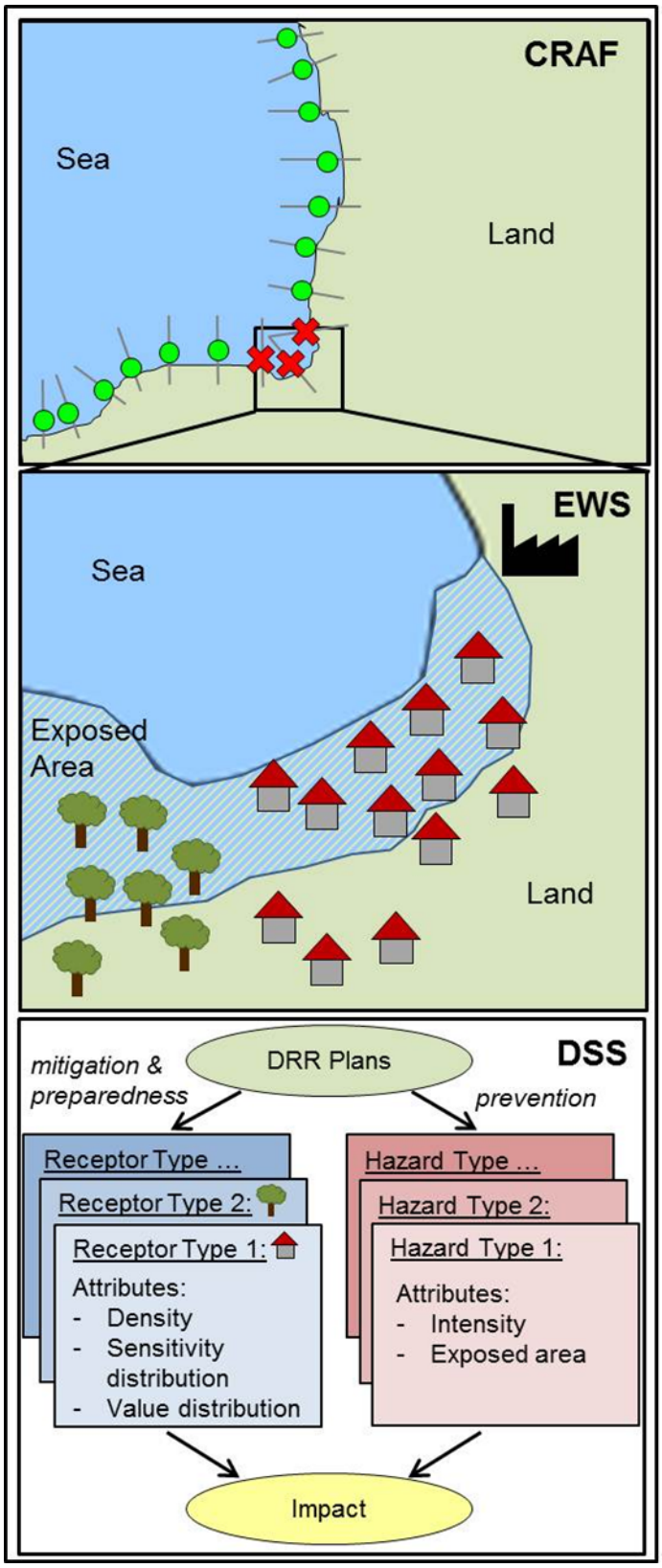

Figure 1.1: Conceptual drawing of the CRAF (top panel), the EWS (middle panel) and the DSS (bottom panel)

Figure 1.2: Case study sites (stars), RISC-KIT case study site partners (blue solid dots) and non-case study site partners (red open circles).

1.3 Deliverable context and objective

Deliverable D3.2 consists three components: a checked-in update of XBeach with accompanying validation document and description, a numerical formulation for storm wave energy dissipation with description in SWAN, and a checked-in flash flood module that can be integrated in the FEWS platform. This deliverable, D3.2, is part of WP 3. The objective of WP 3 is to develop a free-ware Coastal FEWS system (D3.1) based on Delft-FEWS as a platform to construct a model train to predict detailed spatially-varying hazard intensities, improve the physical based numerical models (D3.2) and develop Bayesian-based Decision Support System (D3.3) to predict socio-economic, environmental and cultural impacts of the hazard intensities. The combination of these deliverables is called the Early Warning System/Decision Support System (EWS/DSS) and will be used in WP5 (Application).

Specific to the current Deliverable 3.2, the Description of Work states that "In order to be applicable at the case study sites, some of the model physics will need to be expanded. We foresee the following activities:

a) Improvement and validation of the two-dimensional morphodynamic model XBeach. This activity will include the validation of XBeach for field situations and engineering applications such as overtopping. Furthermore, we will improve the computational efficiency necessary to run computationally-intensive models in operational mode.

b) Development of hierarchical models of storm wave energy dissipation at large, intermediate and small spatial scales, corresponding to <10m (effect of wetland surfaces), >10-30m (wave refraction and diffraction through creeks and salt pans), and 30m - 1,000m (role of mudflat and saltmarsh at the barrier island / tidal inlet scale) respectively.

c) Development of a flash flood module. This module will build upon the experience and advances made in the IMPRINTS and DRIHM projects. The module will work in two modes: a few days in advance of an event and a few hours in advance. For the first time scale, the proposed strategy will be to incorporate the high resolution precipitation forecasts over the Tordera Delta and Bocca di Magra sites to compute the real-time accumulated forecasts of rainfall over the drainage basin. For the second time scale, rainfall forecasts based on radar networks will provide high-resolution estimates that can be transformed into high resolution flash flood warnings.A hydrological multi-model approach will be explored into high resolution flash flood warnings at any location in the drainage system through the use of 2D models.

This task will deliver D3.2 that consists of a checked-in (in OpenEarth) update of XBeach with accompanying validation document and description, a numerical formulation for storm wave energy dissipation with description in SWAN, and a checked-in flash flood module that can be integrated in the FEWS platform with accompanying validation document and description."

This report is part of D3.2 and consists of validation document and description for new XBeach developments, the description of the numerical formulation for storm wave energy dissipation modeling implemented in SWAN, and the description of the improved flash flood module and its integration in the Coastal FEWS platform.

These new developments are made available through the open source and free software community web portal. (www. oss.deltares.nl) with links from the project website www.risckit.eu.

1.4 Approach

In order to apply at the case study sites, three physics-based models have been expanded:

XBeach:

XBeach is an open-source physics-based numerical model which is developed to simulate hydrodynamic and morphodynamic processes and impacts on coasts with a domain size of kilometers and on the time scale of storms in hydrostatic and non-

hydrostatic modes (Roelvink et al., 2009). XBeach has been applied to different types of coasts such as sandy, gravel and urbanized coasts. The model includes the hydrodynamic processes of short wave transformation (refraction, shoaling and breaking), long wave (infragravity wave) transformation (generation, propagation and dissipation), wave-induced setup and unsteady currents, as well as over-wash and inundation. The morphodynamic processes include bed load and suspended sediment transport, dune face avalanching, bed update and breaching. Effects of vegetation and of hard structures have been included. The model has been validated with a series of analytical, laboratory and field test cases using a standard set of parameter settings.

In the framework of the RISC-KIT project XBeach has been further developed to improve the speed of the model and changes are made in physical description to enhance the accuracy and reliability. Overall the newly developed XBeach is 4 times faster than the previous version and more reliable for field cases. The new developments and corresponding validations are reported in this document. These developments include: improving MPI parallel implementation, implementing cyclic lateral boundary conditions, improving the efficiency of directional wave energy propagation, and developing morphological non-hydrostatic model. The developments are validated for a 1D run-up case (Petten Sea Dike, the Netherlands), a case of over-wash with a shallow foreshore (Wenduine Sea Dike, Belgium), a set of laboratory overtopping cases (the EC FP5 CLASH project data base; Steendam et al., 2004), 2D hydrodynamic field cases (Praia de Faro, Portugal and Delilah in North Carolina, USA), 2D morphodynamic cases (Hurricane Sandy impacting Fire Island, Long Island and Camp Osborne, USA).

Storm wave energy dissipation hierarchical model:

The main approach to development of improved models of storm wave energy dissipation at different spatial scales in this study is to i) develop a new formulation for wave dissipation and ii) implement the new formulation in the existing wave modeling tools. For this study the widely used SWAN model (a third generation wave model; Booij et al., 1999) has been chosen as the base for implementation of the new wave dissipation formula.

Recent years have seen the increasing recognition of wave dissipation by vegetation in aquatic and coastal environments. This realization stems from growing field evidence of wave attenuation, both in saltmarshes, brackish marsh reed beds and other types of vegetation. The ability of vegetation, particularly saltmarsh, to dissipate waves is clearly important when storm surges inundate these shallow intertidal areas and storm waves propagate across hydraulically rough surfaces. Predicting this dissipation, however, relies on accurate representation of marsh vegetation canopies – in a spatial hierarchy from the scale of the individual saltmarsh plant stem to the variation in saltmarsh vegetation communities across an intertidal platform - within existing shallow water wave models.

The way to achieve a more accurate representation is by implementation, calibration and validation of formulations of drag as exerted by the vegetation canopy through comparison of model results with observed wave dissipation. Section 1.1 above identifies three scales of pattern to the wave energy dissipation process. These are nested within one another and therefore, in the real world, at any one point in space,

provide a hierarchy of effects. This hierarchy can be conceptualized as comprising: small (<10m), intermediate (>10-30m), and large scale (30m - 1,000m) components. Here we begin at the intermediate (>10-30m) scale. This is because the recent experiment reported by Möller et al. (2014) provides a first-ever opportunity to use observations of wave heights in front of, and behind, an approximately 40 m long experimental test section over transplanted (i.e. actual), floristically diverse salt marsh under realistic simulated storm surge wave trains. We then apply the model developed under these controlled conditions at both the large and small scales of the energy dissipation hierarchy. At the large scale (30m – 1,000 m), we apply the new model formulation to field data on wave energy dissipation collected over a saltmarsh transect at Stiffkey, North Norfolk coast, UK. Thus the application of the model to vegetation types found at this RISC-KIT case study site, and broadly typical of other NW European saltmarsh sites, becomes possible. Finally, at the small scale (< 10m), we use field data to evaluate the role of short-distance variations in vegetation height from very short (ca. 3m length) transects on the performance of the revised model.

In this study, we improve modeling of waves across vegetated intertidal platforms – saltmarsh- as found on many European shores (and at the North Norfolk case study site) by introducing i) a variable drag coefficient to the vegetation module of the SWAN model, and ii) the ability to spatially vary vegetation height.

The new formulation has the advantage that the vegetation part of the model does not need to be calibrated for each test condition or vegetation species. Although the studies reported here are primarily concerned with modeling at different spatial scales, it should also be noted that the new module can also be used for modeling situations over longer periods of time where the wave conditions are likely to vary significantly, such as during storms. This furthers the scope of the vegetation module for use in large scale and longer term storm surge modeling.

Flash Flood Model:

The development of a flash flood model in this project is built upon the experience and advances made in the IMPRINTS. The FP7 project IMPRINTS (FP7-ENV-2008-1-226555; Sempere-Torres et al., 2010) developed a module for flash-flood hazard assessment (named FF-EWS for “Flash Flood Early Warning System”). This FF-EWS module is based on the assumption that the rainfall accumulated upstream of a point of the drainage network can be used to characterize the flash flood hazard. In the RISC-KIT project, the FF-EWS is improved based on radar-based Quantitative Precipitation Estimates (QPE) to assess the flash flood hazard in the coastal area. The improvements made to the system are: (1) increased resolution (FF-EWS has now been implemented at 200 m resolution), and (2) better estimation of the hazard level (expressed in terms of the return period), based on the construction of a 70-year climatology of daily rainfall maps.

This module (FF-EWS) observed rainfall based on radar QPE and can use radar-based nowcasts (for lead times up to a few hours ahead), and NWP rainfall forecasts (for up to a few days ahead). The simplification of relating the probability of occurrence of rainfall with the probability of occurrence of discharges neglects some of the hydrological processes that have an important role in the catchment response (such as the initial moisture state of the catchment). On the other hand, the main advantage of

this approach is that it does not use parameters that require calibration. This is an important advantage for areas where the aim is to detect flash flood events in small and medium catchments that are often un-gauged.

The improved FF-EWS module uses 1-km radar-based QPE and QPF 30-minute accumulations (updated every 10 minutes). This resolution is very well adapted to flash flood monitoring, frequently triggered by rainfall extremes (for example due to stationary convective thunderstorms) at scales that are generally not well resolved by numerical weather prediction (NWP) models or low-resolution rain gauge networks [see, e.g., Alfieri et al. (2012) for a review of the benefits and limitations of the different rainfall inputs used for hazard assessment].

For each point of the drainage network, the high resolution rainfall inputs available at a given time are used to compute the rainfall accumulation aggregated over the upstream basin over a duration corresponding to the concentration time of the catchment. The computations are made for durations between 0.5 and 24 h, for catchments between 5 and 5000 km^2. The hazard assessment (expressed in terms of probability of exceedance, or as return period) is based on comparing the basin-aggregated rainfall accumulations with the values of the available Intensity-Duration-Frequency (IDF) curves for duration equal to the characteristic concentration time of the catchment. Every time a new QPE field is available, a series of rainfall forecasts is computed (with the nowcasting algorithm), and hazard assessment is performed with a resolution of 200 x 200 m^2 and for forecasting times between t+0 and t+3 hours.

This improved version of FF-EWS is applied around the Tordera Delta (RISC-KIT case study site) successfully. The implementation recipe of this improved FF-EWS is made available to be used in other case study sites prone to Flash Flood such as the Bocca di Magra. One of the main objectives of this implementation is the analysis of the multi-model approach, comparing the FF-EWS module (that will be implemented in the case study site of Bocca di Magra in WP5) with the hydrological tools developed as part of the DRIHM project for the same site.

The flash flood hazard assessment products can be displayed in free-ware Coastal FEWS system that is developed as part of Work Package 3 of this project (Deliverable 3.1).The FF-EWS implemented in the RISC-KIT case study site of Tordera Delta, has been adapted to output NetCDF files with the results of the flash flood hazard assessment. A new NetCDF file is created every time a new QPE map is available which is required by the free-ware Coastal FEWS system.

1.5 Outline of the report

This report is structured in 4 chapters. After the introduction in Chapter 1, each of remaining chapters is dedicated to the development, improvement and application/validation of a different physics-based model: XBeach, the SWAN wave energy dissipation model and the Flash Flood Model.

2 Improvement and validation of the two-dimensional morphological model XBeach

2.1 Introduction

Task 3.2a of the RISC-KIT project is the improvement and validation of the two-dimensional morphodynamic model XBeach. This activity includes the validation of XBeach for field situations and engineering applications such as overtopping. Furthermore, it includes improving the computational efficiency necessary to run computationally-intensive models in operational mode. This chapter addresses the result of Task 3.2a of the RISC-KIT project, including (1) how computational efficiency is increased, and (2) developments and validation of the model for engineering applications.

XBeach is an open-source numerical model which is originally developed to simulate hydrodynamic and morphodynamic processes and impacts on sandy coasts with a domain size of kilometres and on the time scale of storms. Since then, the model has been applied to other types of coasts and purposes.

The model includes the hydrodynamic processes of short wave transformation (refraction, shoaling and breaking), long wave (infragravity wave) transformation (generation, propagation and dissipation), wave-induced setup and unsteady currents, as well as over-wash and inundation. The morphodynamic processes include bed load and suspended sediment transport, dune face avalanching, bed update and breaching. Effects of vegetation and of hard structures have been included. The model has been validated with a series of analytical, laboratory and field test cases using a standard set of parameter settings.

XBeach has two modes: a hydrostatic and a non-hydrostatic mode. In the hydrostatic mode, the short wave amplitude variation is solved separately from the long waves, currents and morphological change. This saves considerable computational time, with the expense that the phase of the short waves is not simulated. A more complete model is the non-hydrostatic model which solves all processes including short wave motions, but with greater computational demand.

The original application, funded by the U.S. Corps of Engineers in the framework of the Morphos project and the U.S. Geological Survey, was to be able to assess hurricane impacts on sandy beaches. Since then with funding from the Dutch Public Works Department, the model has been extended, applied and validated for storm impacts on dune and urbanized coasts for the purpose of dune safety assessments. With support from the European Commission XBeach has been validated on a number of dissipative and reflective beaches bordering all regional seas in the EU, in the framework of the MICORE project, and is now being further validated, improved and field-tested in the framework of the RISC-KIT project.

Beyond sandy coasts, the model has been applied to coral fringing and atoll reefs, in cooperation with and with funding by the University of Western Australia, the USGS

and the Asian Development Bank. The model now also includes vegetative damping effects, with support of the U.S. Office of Naval Research.

The non-hydrostatic model has been developed initially by the TU Delft (as a prototype version of the SWASH model). For the purpose of simulating the morphodynamic processes on gravel beaches, the model was extended and validated with support from Plymouth University.

Notwithstanding its wide application on a large range of coasts, there was obvious room for improvement in two main areas:

- Computational efficiency; for 2DH applications the runtime can be significant; since in a number of case studies within this project large numbers of runs are required, as serious effort was required to bring down the run time, through various means, including improvement of the parallel implementation using MPI, optimization of the code, better boundary conditions allowing to reduce the model size and a smarter short wave propagation scheme. These developments are described in Section 2.2.
- In a number of case studies there will be steep hard structures as part of the coastal defense. For such cases it is not likely that the 'surfbeat' approach focusing on infragravity wave run-up and overtopping is sufficient, and the recently implemented wave-resolving, non-hydrostatic approach has been tested both for applicability and for accuracy, against a range of run-up and overtopping data. It has also been tested for its morphological behavior. These activities are reported in Section 2.3.
- The application of XBeach to steeper beaches has been explored within the MICORE project but especially for run-up and overtopping further validation was deemed necessary, since in the present project inundation of the hinterland is one of the important hazards to be predicted by the system. Recent validation of the infragravity wave run-up against US field data (Stockdon et al., 2014) indicated a significant under prediction by XBeach, which further pointed to the need to analyze the prediction of the infragravity wave distribution in the surfzone and the subsequent run-up. A new scheme for propagation of directionally spread short waves has been validated against both hydrodynamic and morphodynamic field cases, as is described in Section 2.4 and Section 2.5, respectively.

The main findings and recommendations are summarized in Section 2.6.

2.2 Improving the computational efficiency

2.2.1 Improving MPI parallel implementation

In 2008, XBeach was parallelized, using MPI as parallelization tool. In 2013 it was decided that the XBeach code needed some improvements:

- cleaning up the code;
- re-arrange the parallelization strategy;
- use double borders to communicate. This simplifies the code and reduces the amount of communication;

- take care that only one process is creating the large output files, and take care that the compute processes do not wait for the completion of the output

The activities described in this framework were carried out by Willem Vermin at SURFSARA, in close collaboration with Dano Roelvink at UNESCO-IHE.

Cleaning up the code

Using gfortran as Fortran compiler, with the flags: '-Wall -fcheck=all', many instances of unused variables were found and a few array over-indexing errors were located and corrected.

Using Valgrind[1] we found some cases of the use of un-initialized variables. These were repaired.

Using a profiler (gprof) we found that an appreciable amount of time (5% and more) was spent in the Fortran intrinsic 'trim' function. This was fixed by using integer constants with meaningful names instead of character strings with meaningful values. After the conversion from strings to integers, no detectable time was spent in the 'trim' function.

Double borders

The code resulting from the parallelization in 2007–2008[2] is based on the 2D decomposition of the domain, using one shadow border on each side of the domains. However, for many of the equations solved in the model a wider stencil is used requiring communication of two adjacent rows/columns to and from bordering domains. When two rows and columns are exchanged, for standard XBeach applications only the following primary variables need to be communicated:

- ee (wave energy)
- rr (roller energy)
- zs (water level)
- uu (u-velocity)
- vv (v-velocity)
- cc (concentration)
- zb (bed level)

This is a large reduction compared to the thirty-odd variables that had to be communicated when only one row/column was exchanged. It simplifies the code, leads to much better accuracy of the coupling and is generally faster.

1 Valgrind is an instrumentation framework for building dynamic analysis tools. There are Valgrind tools that can automatically detect many memory management and threading bugs, and profile your programs in detail. http://valgrind.org/

2 https://surfsara.nl/sites/default/files/parallelization-report-63.pdf

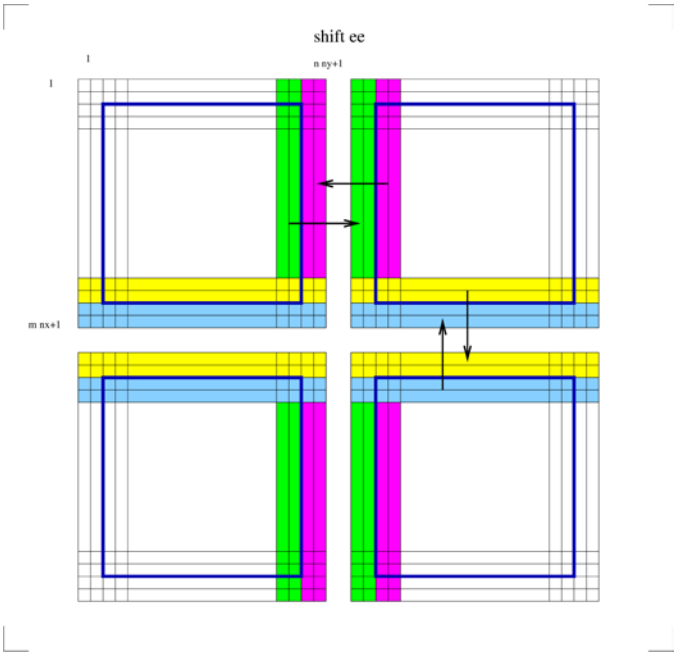

Figure 2.1 Communication of two rows and columns between domains using MPI. The areas within the thick drawn lines are where the full computations are carried out.

I/O by a dedicated process

In the 2008 version, (NetCDF) output is produced by one process, which also takes part in the computations. Since the program tends to produce rather large output files (often several Gigabytes), all computing stalls until the output is finished. Therefore we changed the code such that one process is dedicated to produce the large output files, and that the data for output is collected before output is actually done. So, while the output-process is creating the output files, the other processes continue computing. The implementation of this change, although conceptually trivial, was in practice quite complicated. Luckily, the scientific parts are unaffected, but the service subroutines used to distribute, collect and shift data were modified. The program is still in a state that the contributors of code can concentrate on the science and have little or nothing to bother about the parallelization.

The master process (process 0) is responsible for all major output, while process 1 is responsible, next to taking part in the computations, for the input at the start of the program, and for output to standard output and standard error (a few pages), and reading and writing small files during the computations. At this time, only the NetCDF output has been adapted, the plain-Fortran binary file output is more difficult to adapt because of its less modular approach.

Preventing CPU cycle waste

In most MPI implementations, waiting for a message is done in tight polling CPU-loops. This method is faster than waiting for interrupts. For the master process (responsible for the major output) this behavior can be undesirable: the process consumes 100% CPU between output cycles, and prevents an efficient use of the CPU by other processes. This has been repaired as follows: at the start of an output cycle,

process 1 sends a message to process 0. Process 0 is waiting for this message using a loop containing MPI_Test() and a call to sleep() for a few milliseconds. The resulting CPU usage between output cycles for process 0 is dropped from 100% to about 1%.

Rewrite of distribution and collecting subroutines

The subroutines used for distribution at the start of the program, and collecting at an output cycle, have been rewritten using MPI_Alltoallw for the communication and MPI_Type_create_subarry to define the derived types, describing what has to be sent or received. This resulted in a better readable code: the original code was based on quite hairy code using MPI_Isend and MPI_Irecv. It was possible that the collecting subroutine collected the same item more than once, depending on the input from the user. We made the collecting routine more intelligent: it remembers which data has been collected, and will not collect it again.

Improvement of the SIP solver[3]

When looking at the results of the 2008 code, minor differences were visible on the process-boundaries, comparing the output of the serial code and the output of the parallel code. These discrepancies are removed by adding a few MPI_Allreduce operations and one border shift operation inside the SIP solver that is used in groundwater.F90 and nonh.F90.

Single precision output

Originally, all output was done using double precision. This was changed: by setting the appropriate macro in the source code of the NetCDF-output (ncoutput.F90), one can choose between single precision and double precision output. Single precision output is for by far the most cases adequate, and has the advantage of speedier output and less file space: each improves by a factor of 2.

Speeding up compilation and execution time by using less pointers

In the 2008 code, many lines refer to members of derived types, containing a few hundred items, like s%nx and s%ny. Since this looks less friendly than simply nx and ny, most of the subroutines contained automatically generated include files which declared for example nx and ny as pointers, pointing to s%nx and s%ny. Simple experiments revealed that this construct results in less efficient code: about 5% to 10%. So it was decided to remove these constructs and use s%nx and s%ny. Also, in one place (indextos.F90) it appeared that the compiler spent too much time in generating code involving long select constructs containing pointers in derived types. This was solved by assigning first to a local pointer, and subsequently to the pointer in the derived type. With these changes, compilation using -O3 compilation is no problem anymore.

In summary, the improvements are:

- double borders implemented: less communication needed
- much fewer calls to shift routines

3 http://en.wikipedia.org/wiki/Stone_method

- better accuracy: no noticeable differences between a serial and a parallel run
- better scalability
- program runs faster, also the serial version
- better and more maintainable code for distributing and collecting data

Results

The code was tested with the 'Port_fine' case: grid = 500*1250, complete output of 5 fields: zs, zb, u,v,H at 300 time steps, output file is 3.6 Gbyte. The final water level picture is shown below. The case was run in non-hydrostatic mode resolving individual waves. Regardless of the number of parallel processes (and thus coupled domains), there are no significant differences between single-domain and multi-domain runs. The test case was selected because the non-hydrostatic wave model with iterative pressure solver was the most likely to give differences when using parallel domains.

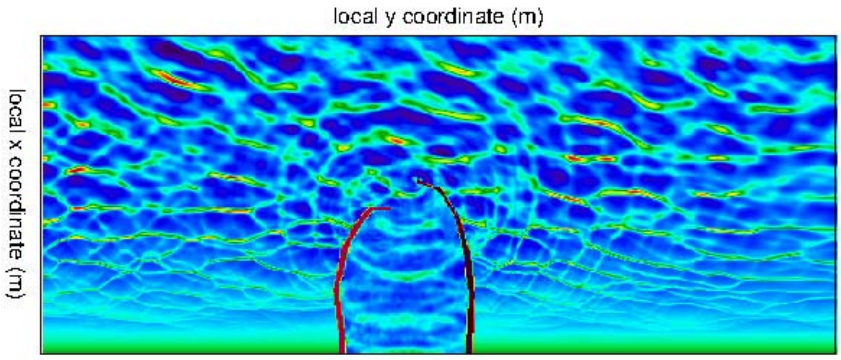

Figure 2.2 Predicted short wave pattern for the test case 'Port_fine'

Below are the speedup and timing results. Note that the new code uses at least 2 processes, one for computation, one for output. However, the extra process uses only a fraction of the CPU.

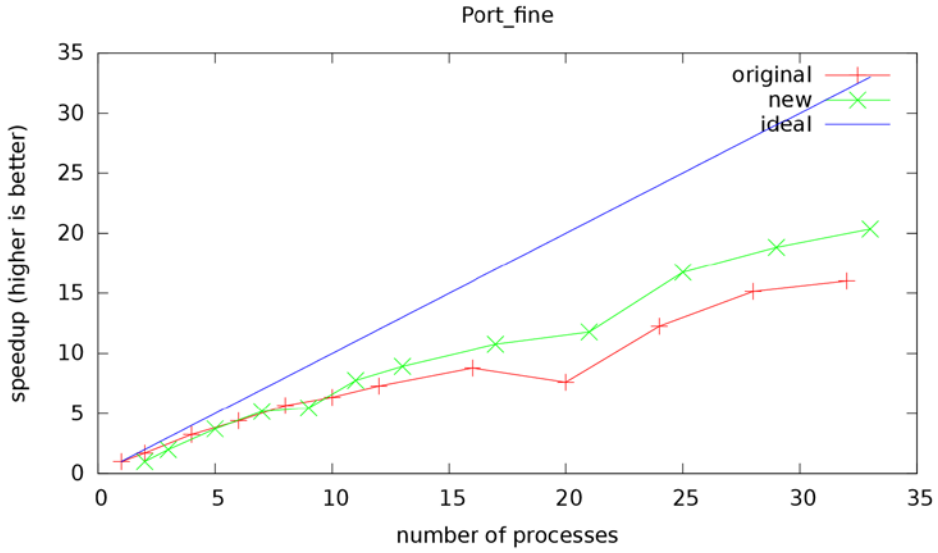

Figure 2.3 Speedup of the new code compared to the original code.

The new code shows a better speedup

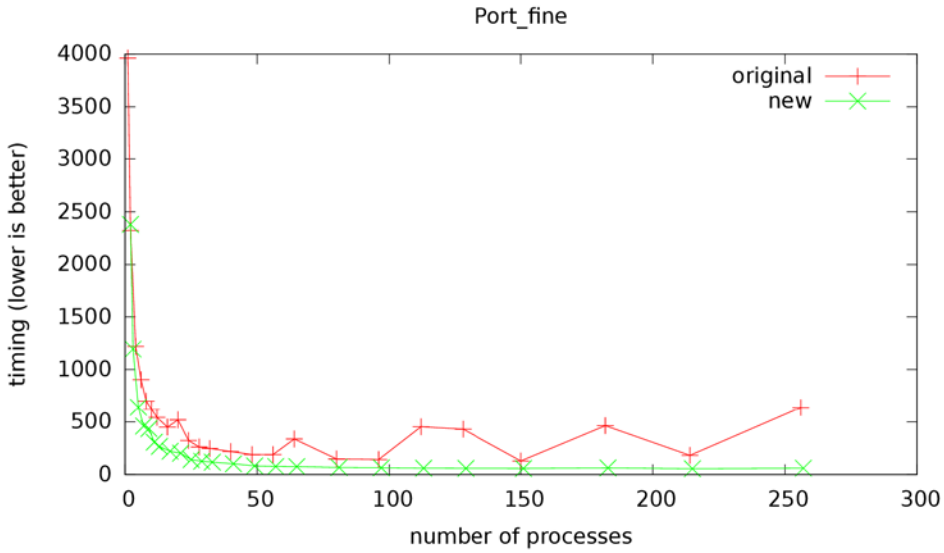

Figure 2.4 Timing (in CPUs) of the new code compared to the old code.

The old code clearly suffers from the delays that are caused by the wait times for completion of the output.

An additional test was carried out running the model in 'surfbeat' mode, as a realistic test of a standard large 2DH application. The speedup behavior was tested on the Cartesius supercomputer at SURFSARA, leading to the speedup as in the figure below, with approx. a factor 150 speedup on 250 processes.

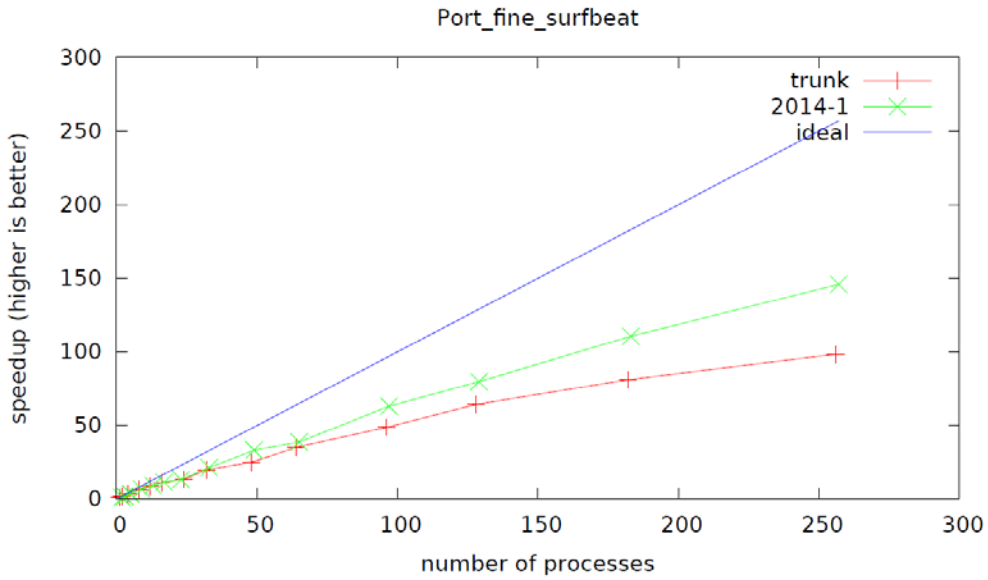

Figure 2.5 Speedup for Port_fine_surfbeat case on Cartesius.

2.2.2 Implementing cyclic lateral boundary conditions

With only minor changes the same MPI coupling scheme was extended to include cyclic boundaries. For cases without important longshore gradients (so excluding cases with important tidal longshore currents) this can lead to robust model behavior with negligible lateral boundary disturbances; particularly useful to limit the longshore extent of short wave resolving models and hence their computational demand. The implementation is such that the simple keyword cyclic = 1 overrides other wave or flow lateral boundaries and works throughout wave, flow, transport and bed update modules. The implementation was tested for a case-study in Albufeira, Portugal (Figure 2.6).

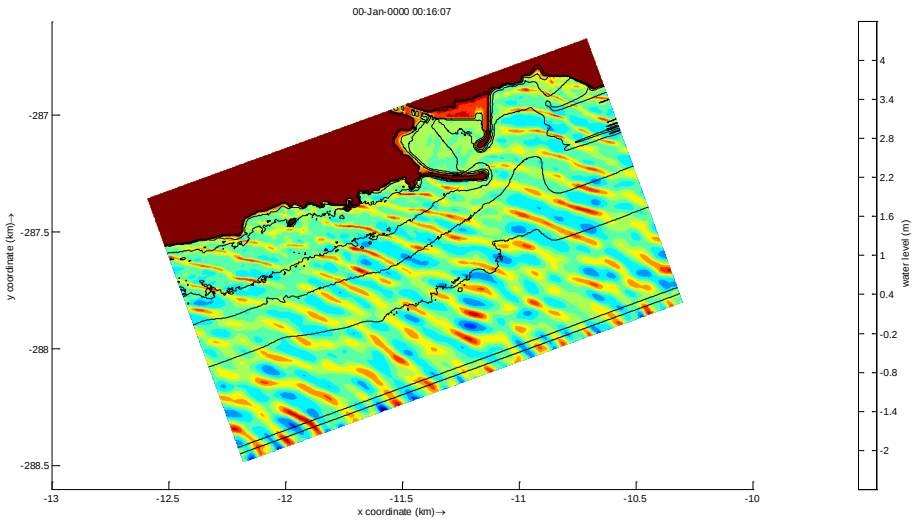

Figure 2.6 Example of use of cyclic boundaries, non-hydrostatic wave model for Albufeira

2.2.3 Improving the efficiency of directional wave energy propagation

The standard mode of solving the time-varying wave energy balance in XBeach is to compute the propagation of wave energy (or action) in x, y and θ space simultaneously, by solving the 3D advection equation:

$$\frac{\partial A}{\partial t}+\frac{\partial c_x A}{\partial x}+\frac{\partial c_y A}{\partial y}+\frac{\partial c_\theta A}{\partial \theta}=-\frac{D_w+D_f+D_v}{\sigma} \tag{0.1}$$

Here the wave action A is calculated as:

$$A(x,y,t,\theta)=\frac{S_w(x,y,t,\theta)}{\sigma(x,y,t)} \tag{0.2}$$

where θ represents the angle of incidence with respect to the computational x-axis, S_w represents the wave energy density in each directional bin and σ the intrinsic wave frequency. The intrinsic frequency σ and group velocity c_g is obtained from the linear dispersion relation. For each directional bin i the horizontal propagation speeds are equal to:

$$\begin{aligned} c_{x,i} &= c_g \cos\theta_i \\ c_{y,i} &= c_g \sin\theta_i \end{aligned} \tag{0.3}$$

The refraction of the waves is produced by the 'refraction speed' c_θ.

An alternative to this approach is to first calculate the mean wave directions and to propagate the short wave energy along these directions. This can be achieved by alternating a stationary run to obtain the mean wave direction with instationary runs where the following reduced equation is solved:

$$\frac{\partial A}{\partial t}+\frac{\partial c_g \cos\bar{\theta} A}{\partial x}+\frac{\partial c_g \sin\bar{\theta} A}{\partial y}=-\frac{D_w+D_f+D_v}{\sigma} \tag{0.4}$$

This effectively reduces the problem from a 3D to a 2D problem, where the occasional (say, every 10 min) stationary run to obtain the direction takes relatively little time.

Apart from saving time (approx. a factor 2), it turns out that it has an important additional advantage. With the standard XBeach scheme, the variability of the wave height on the wave group scale tends to reduce rather strongly. The reason for this is that the wave energy coming from different directions is added, but interference between the different wave trains is ignored. This can be especially problematic for rather wide directional spectra. In the figure below we compare the wave height fields and long wave fields for three situations:

1. Non-hydrostatic mode; we have filtered the results to obtain the short wave height field and the water level fields;
2. Single_dir mode, the new implementation;
3. Multi-dir, with a directional bin size of 10 deg.

From the figure below we can see that the single_dir wave height pattern retains much more variability of the wave height than the multi_dir standard version, in

comparison with the non-hydrostatic result. Obviously, the latter has interesting short wave reflection patterns that are not represented in the surf-beat mode, but apart from this the patterns between non-hydrostatic and single_dir are very comparable. As a side note, there are clear lateral boundary disturbances visible, especially at the northern boundary; the cyclic boundary option gets rid of these entirely. In the 2DH test case of Delilah we will validate and compare both approaches.

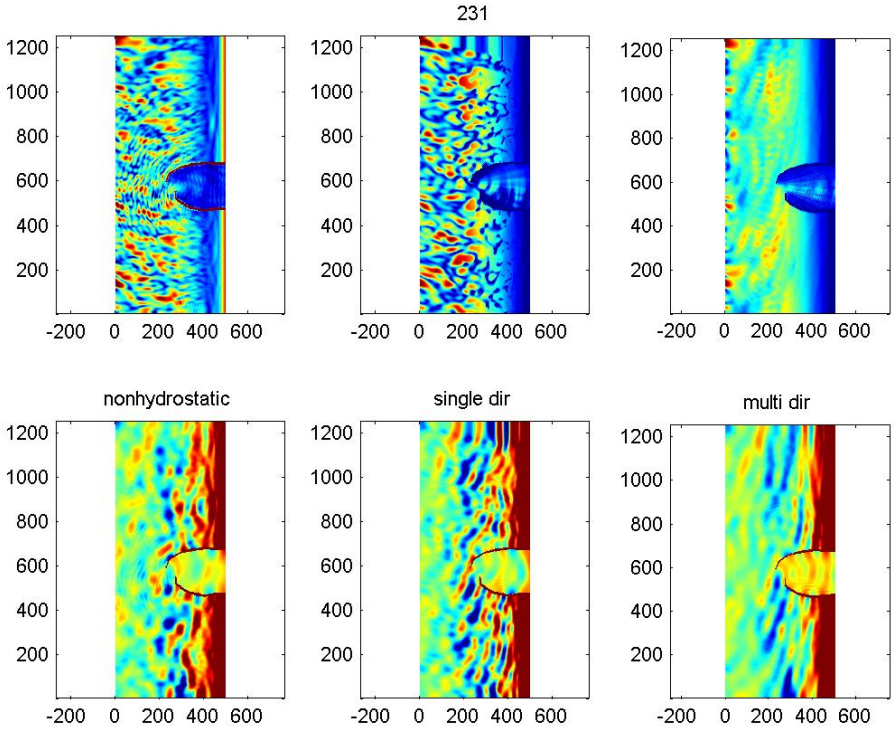

Figure 2.7 Snapshots of slowly-varying wave height (top panels) and water level (bottom panels) for non-hydrostatic mode (left), single_dir mode (middle) and multi-dir mode.

2.3 Developments and validation of non-hydrostatic model

2.3.1 Validation of wave run-up: Petten case

Introduction

Within the framework of the European MAST-OPTICREST project, prototype measurements are were performed on the Petten-sea defense. The main characteristic of this dike is a complex shallow foreshore which is a good case to investigate how it affects wave run-up height.

There are two types of measurements for these tests, of which well-controlled physical model tests have been used to see the response of the XBeach for different

wave conditions. The physical model tests were performed in the Scheldt Flume of Deltares in Delft

The main topic concerning the model set-up was the schematization of the foreshore. Figure 2.8. shows the measured foreshore perpendicular to the Petten Sea-defense. As it shows between 7 and 3 km offshore, the depth gradually decreases from NAP-20 m to NAP-10 m with an average slope of approximately 1:400. Then the foreshore shows an offshore bar with a crest at approximately NAP-6 m. Landward of the offshore bar, the depth increases again to NAP-12 m at about 1km from the dike. Figure 2.9 shows a more detailed graph of the foreshore in the last kilometer which could be modeled in the flume. A second bar with a crest at about NAP-3.5 m is present at about 500 m seaward from the crest of the dike. The toe of the dike is at a level of about NAP-0.5 m. Figure 2.10 shows the dike consisting of a 1:4.5 lower slope, a berm of about 1:20 from NAP +5.0 m to NAP +5.7 m and a 1:3 upper slope.

Wave run-up levels were measured relative to SWL at the upper slope by sensors, acting as a step-gauge within the smooth slope. Also in the physical model tests, the measurements were performed on this upper slope. It should be noted that the minimum water layer thickness on the upper slope is considered as 0.10 m for these prototype tests. The crest elevation is NAP+12.9 m and all slopes are considered to be smooth.

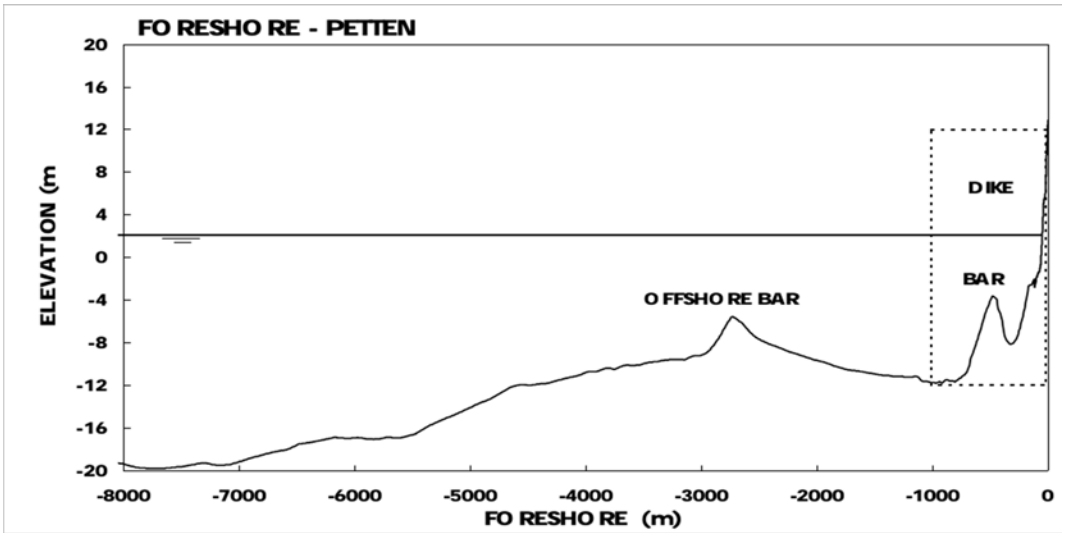

Figure 2.8 *Measured foreshore perpendicular to the Petten Sea-defense*

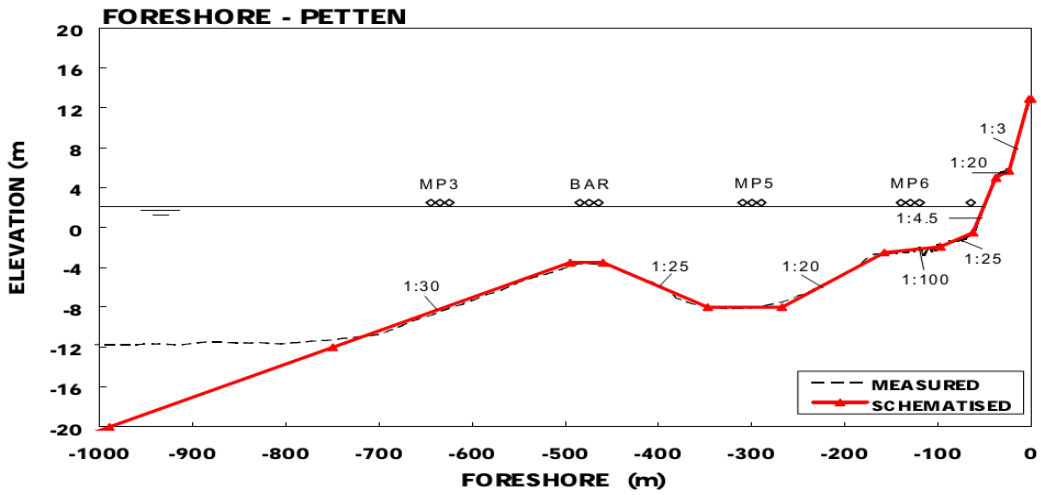

Figure 2.9 Schematized foreshore for model tests

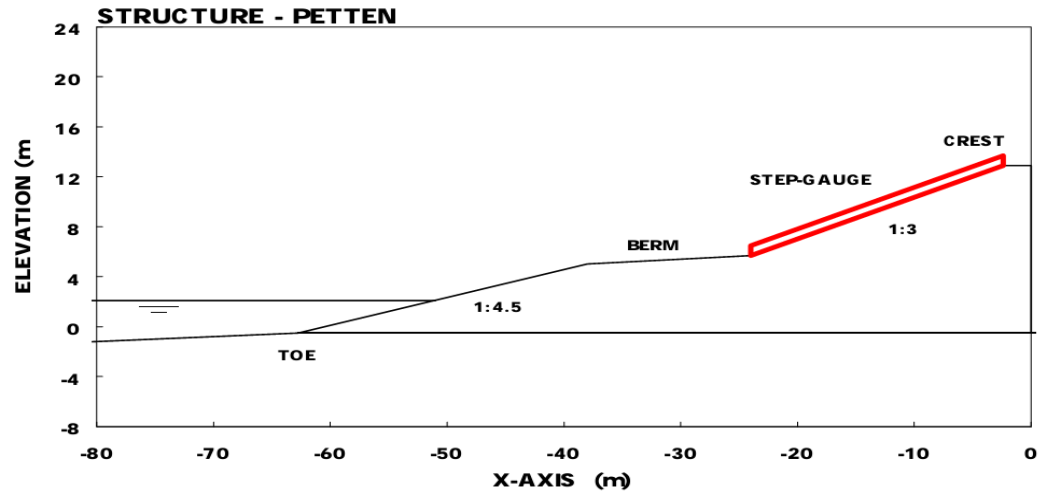

Figure 2.10 Schematized structure for model tests

Wave conditions

JONSWAP type wave conditions were specified using parametric spectra defined case by case. Physical models of Petten cases were analyzed based on specified peak period and significant wave height. Directional spreading coefficient 's' is set to 1000 (unidirectional waves). All data are given and all models were run at prototype scale. Table 1 presents a summary of all the physical model tests.

Simulation setup

A uniform grid with resolution of 1 m was applied. The simulation was run over a period of 2 hours to obtain a good statistical representation of the 2% run-up height.

Table 2.1: Name of the table Characteristics of the prototype cases of Petten sea defense and the resulted wave run-up level predicted by XBeach

Test	X (m)	Dike upper slope	Dike lower slope	Berm slope	Foreshore slope	h deep (m)	h toe (m)	Rc (m) , + NAP	Hm0 (m)	Rc/Hm0	Sop	S m-1,0	Tp (sec)	Tm-1,0 (sec)	R2% (m) +SWL, Measured	R2% (m) , Predicted by Xbeach (non-Hyd.)
1.01	1296	1 ; 3	1 ; 4.5	1 ; 20	complex (constant)	-26.10	-2.72	12.90	4.80	2.688	0.036	0.046	9.30	8.2	4.70	4.95
1.02	1296	1 ; 3	1 ; 4.5	1 ; 20	complex (constant)	-26.04	-2.66	12.90	4.50	2.867	0.038	0.044	8.70	8.1	4.80	4.62
1.03	1296	1 ; 3	1 ; 4.5	1 ; 20	complex (constant)	-26.24	-2.86	12.90	3.90	3.308	0.012	0.027	14.40	9.7	5.30	5.05
1.04	1296	1 ; 3	1 ; 4.5	1 ; 20	complex (constant)	-25.66	-2.28	12.90	4.40	2.932	0.011	0.025	16.20	10.700	5.30	5.11
1.05	1296	1 ; 3	1 ; 4.5	1 ; 20	complex (constant)	-25.60	-2.22	12.90	3.10	4.161	0.012	0.022	13.00	9.4	4.10	4.35
1.06	1296	1 ; 3	1 ; 4.5	1 ; 20	complex (constant)	-26.04	-2.66	12.90	4.00	3.225	0.030	0.035	9.30	8.600	4.70	4.60
2.12	1296	1 ; 3	1 ; 4.5	1 ; 20	complex (constant)	-26.10	-2.72	12.90	3.10	4.161	0.017	0.022	10.80	9.500	4.30	4.47
2.13	1296	1 ; 3	1 ; 4.5	1 ; 20	complex (constant)	-26.10	-2.72	12.90	4.10	3.146	0.019	0.022	11.80	10.900	5.00	5.00
2.14	1296	1 ; 3	1 ; 4.5	1 ; 20	complex (constant)	-26.10	-2.72	12.90	5.20	2.481	0.020	0.022	13.00	12.300	5.50	5.23
2.15	1296	1 ; 3	1 ; 4.5	1 ; 20	complex (constant)	-26.10	-2.72	12.90	6.20	2.081	0.019	0.023	14.40	13.100	6.30	5.42
2.21	1296	1 ; 3	1 ; 4.5	1 ; 20	complex (constant)	-28.70	-5.32	12.90	2.00	6.450	0.017	0.022	8.60	7.600	3.30	3.65
2.22	1296	1 ; 3	1 ; 4.5	1 ; 20	complex (constant)	-28.70	-5.32	12.90	3.10	4.161	0.017	0.022	10.80	9.500	5.30	5.34
2.23	1296	1 ; 3	1 ; 4.5	1 ; 20	complex (constant)	-28.70	-5.32	12.90	4.10	3.146	0.019	0.022	11.80	11.000	6.60	6.32
2.32	1296	1 ; 3	1 ; 4.5	1 ; 20	complex (constant)	-26.10	-2.72	12.90	4.20	3.071	0.036	0.040	8.60	8.200	4.40	4.50
2.33	1296	1 ; 3	1 ; 4.5	1 ; 20	complex (constant)	-26.10	-2.72	12.90	4.10	3.146	0.019	0.022	11.80	10.900	5.00	4.90
2.34	1296	1 ; 3	1 ; 4.5	1 ; 20	complex (constant)	-26.10	-2.72	12.90	3.90	3.308	0.007	0.009	18.50	16.300	5.40	5.13
2.41	1296	1 ; 3	1 ; 4.5	1 ; 20	complex (constant)	-28.70	-5.32	12.90	3.90	3.308	0.054	0.056	6.80	6.700	4.40	3.68
2.42	1296	1 ; 3	1 ; 4.5	1 ; 20	complex (constant)	-28.70	-5.32	12.90	4.20	3.071	0.031	0.040	9.30	8.200	5.30	5.45
2.43	1296	1 ; 3	1 ; 4.5	1 ; 20	complex (constant)	-28.70	-5.32	12.90	4.10	3.146	0.019	0.022	11.80	11.000	6.60	6.31
2.62	1296	1 ; 3	1 ; 4.5	1 ; 20	complex (constant)	-26.10	-2.72	12.90	4.10	3.146	0.019	0.022	11.80	10.900	5.00	4.90
2.63	1296	1 ; 3	1 ; 4.5	1 ; 20	complex (constant)	-26.90	-3.52	12.90	4.10	3.146	0.019	0.022	11.80	11.000	5.70	5.26

The R2% run-up height as measured in the physical model and predicted by XBeach is shown in the last columns of Table 1 and in Figure 2.11. The results show that for a typical 1D (cross-shore) application with a complex shallow foreshore and dike with berm, under controlled conditions with second-order steering and reflection compensation, non-hydrostatic XBeach predicts the run-up height with good accuracy, in these cases with a maximum deviation of 15%.

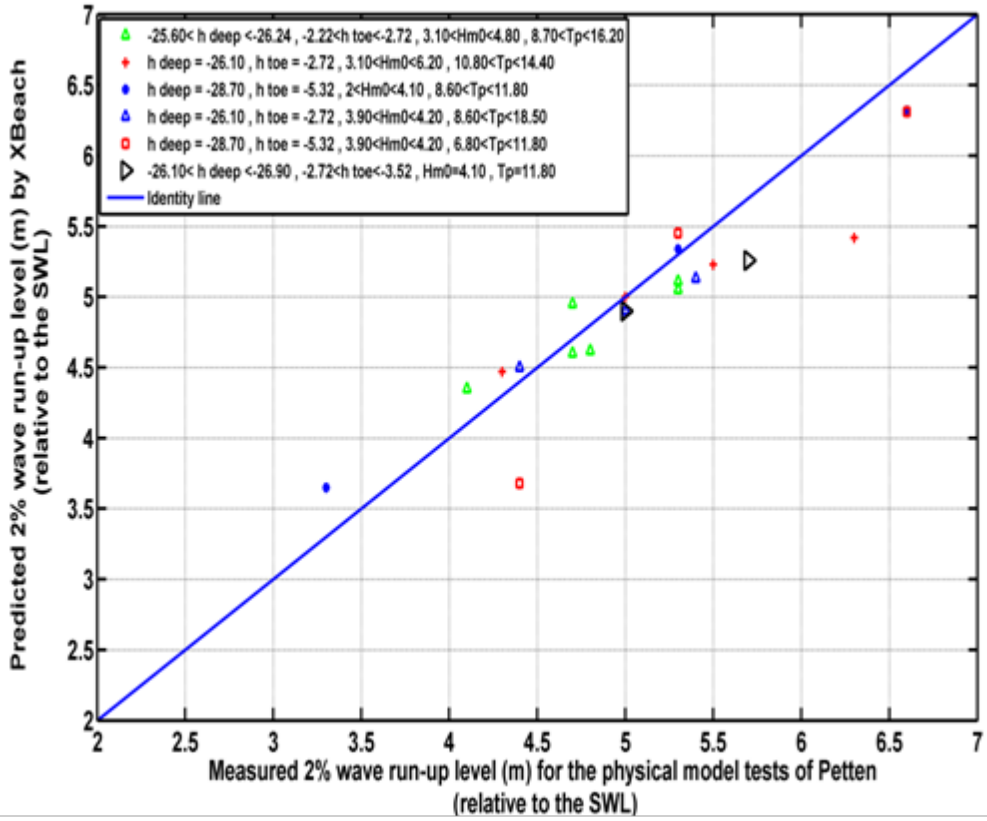

Figure 2.11 Predicted R2% by XBeach compared to the physical models of Petten tests, based on different wave conditions

In this section, a detailed case is modeled by XBeach to investigate the capability of XBeach in simulating wave overtopping and run-up for one of the weak links of the Flemish coastal town of Wenduine in Belgium. This town has been highlighted as one of the weak links in the Flemish master plan for coastal safety.

The model in this section is set based on a study that has been done for the capability of the SWASH model (Zijlema, et al., 2011) for wave transformation and overtopping discharge for four selected impermeable dikes with different characteristics, (T.Suzuki et al. 2011). The SWASH model was validated based on the comparison to the physical model measurements in terms of significant wave height, spectral analysis, maximum wave height, wave set-up, average period and peak period for one of the four cases. Also, wave overtopping discharge was obtained from SWASH and physical models for all the tests.

Figure 2.12 shows the geometry of this physical model including the pointed wave gauges for six stations starting from offshore to the toe of the structure in order to get the measurements. The topography and the dike, consisting of a shallow foreshore 1:35 and a relatively steep slope dike (1:2) represents the typical configuration of the coastline at Wenduine, Belgium. On the next page, table 2.1 indicates the detailed characteristics of the physical model tests for these four models. This case is a very specific case and has actually never been considered in coastal structure design. The water level at the toe of the dike is only a few decimeters, where the initial significant wave height in deep water is almost 5 m. The main difference with "conventional" coastal structure design is this very small water depth. A rule of thumb gives that the depth limited wave height is roughly half the water depth. That would mean one or two decimeter. Reality is much different, due to the transformation of a short wave spectrum to a spectrum which has only long waves.

Note that the long wave phenomena in this situation will likely be overestimated compared to reality since the short-crestedness of waves (2D-effect) will reduce the long wave energy.

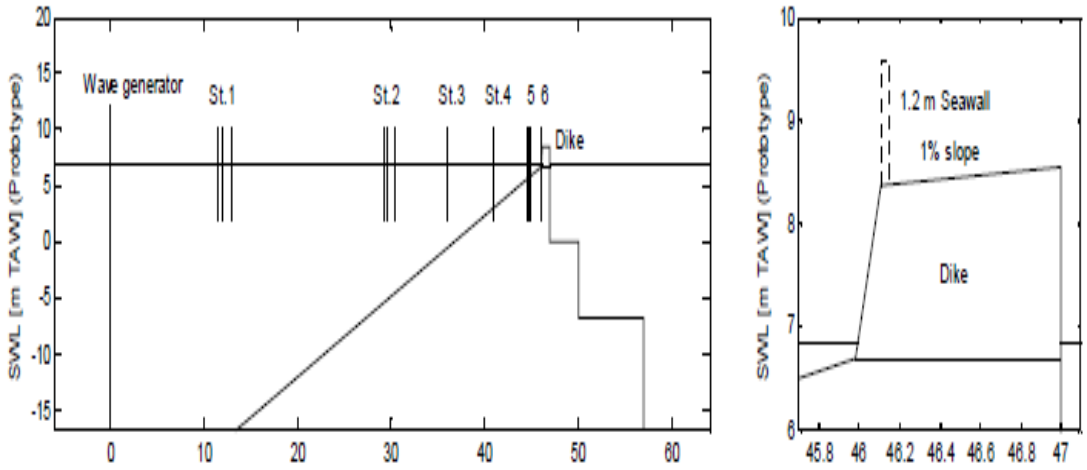

Figure 2.12 Experimental setup of wave transformation and wave overtopping on the Wenduine sea dike (SWL =6.84m TAW, 1:25 scale)

Case description

The physical model topography and sea dike were constructed at a Froude scale of 1:25 as is shown before in detailed in 2.12. The topography was simplified into a 1/35 foreshore slope starting 13.3 m from the wave paddle up to the toe of the sea-dike, and constructed from smooth concrete. The dike has a wide crest with a seaward 1/100 slope. In this section one test was conducted with irregular waves (Jonswap γ=3.3) with one storm condition and dike condition shown in the table 2.2.

In the physical model, the wave flume length is 70 m, width is 4 m and height is 1.45 m. As it is shown in the Figure 2.12, the vertical axis shows prototype scale while the horizontal axis is in model scale. When it comes to the prototype scale, the level of the bottom is set at -16.68 m, the toe and the dike were set at +6.70 m and 8.38 m, respectively. Also, the level at the end of the dike considering the dike slope of 1:2 m is set at +8.56 m TAW (Tweede Algemene Water passing, Belgium standard datum level, situated near MLLWS).

Table 2.2 Test characteristic for the physical model that is reproduced by XBeach

Test No.	Dike configuration	Prototype Scale			1:25 model scale		
		SWL	Hm0 (m)	T_p (s)	h (m)	Hm0 (m)	T_p (s)
1A	Dike only	6.84	4.75	11.70	0.940	0.190	2.34

Grid setup

Numerical modeling of the mentioned case has been carried out by XBeach model using a grid size of 0.04 m in the horizontal. The geometry mentioned in the Figure 2.12 was reproduced in the numerical domain at physical model scale. Regarding the grid size of 4 cm, the length of the numerical flumes was 52 m long with 1300 grid cells. The time duration of the numerical simulation was 40 minutes, the same as the physical model experiment.

Non-hydrostatic 1D boundary conditions and absorbing-generating (weakly-reflective) back boundary condition in 1D were applied for the front and back side of the numerical model, respectively.

Results

In Figure 2.13 through Figure 2.15 the measured wave spectra are compared with those simulated in XBeach. Obviously, there is a difference in the exact spectral shape at the offshore point, where XBeach shows a typical JONSWAP shape and the model is less peaked. Apparently, the model is not very sensitive to the exact spectral shape since in shallow water (points 5 and 6) the spectra are dominated by the infragravity waves and the shape and energy in these low-frequency spectra are reproduced well by the model.

The Hm0 distribution is also reproduced nicely as is shown in Figure 2.16. The most sensitive parameter here is *maxbrsteep*: the criterion determining when the nonhydrostatic correction is turned off and wave dissipation inherent in the nonlinear shallow water equations takes over for breaking waves. As shown in Figure

2.16, the optimum value for this case is 0.4, but the deviation for the default value of 0.6 is relatively small.

In the same figure, as could also be seen in the spectra, the peak period jumps to values in the range 20-40 s, indicating the dominance of infragravity waves in the very shallow area.

Table 2.3 Numerical parameters used in ''params.txt'' file for the preliminary scale case 1A

Numerical parameters	Value used for small scale test	Definition
nonh	1	Nonhydrostatic correction on
secorder	1	Second order wave propagation scheme
nhbreaker	2	Breaking model for nonh
maxbrsteep	varying	Wave height/water depth ratio where nonhydrostatic correction is turned off
CFL	0.9	Maximum courant number
C	varied	Chezy coefficient
tstop	2400	Stop time simulation (sec)
tintg	0.2	Time interval output point values (sec)
instat	jons	Offshore wave boundary conditions
bcfile	jonswap	Boundary conditions file
random	0	Random generator (off)
rt	2400	Record length (sec)
dtbc	0.1	Time step
front	nonh_1d	Seaward weakly-reflective boundary condition
back	abs_1d	Landward weakly reflective boundary condition

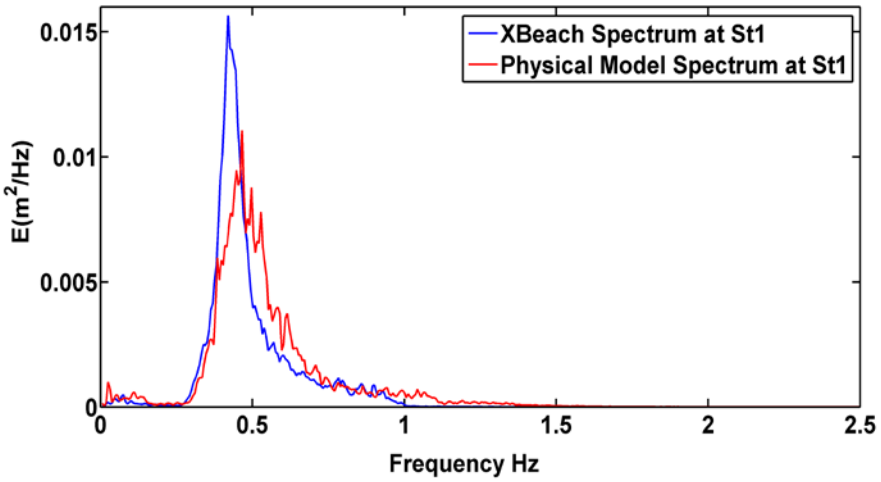

Figure 2.13 Comparison of wave spectra for station 1

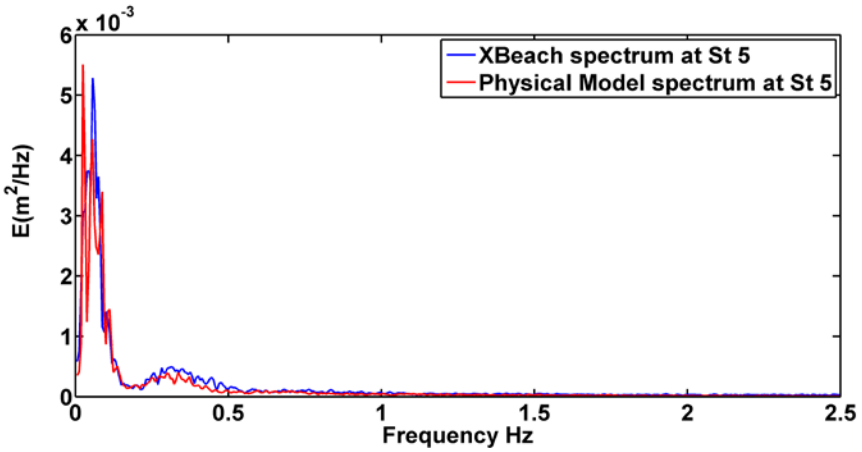

Figure 2.14 Comparison of wave spectra for station 5

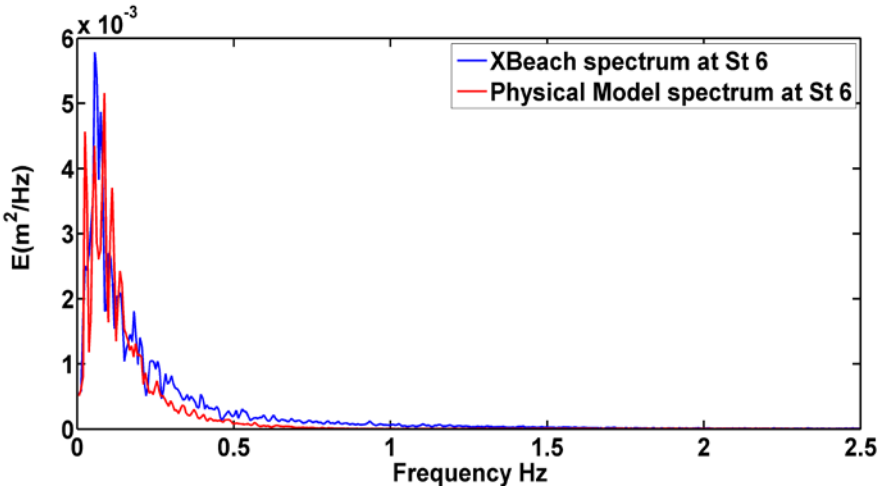

Figure 2.15 Comparison of wave spectra for station 6

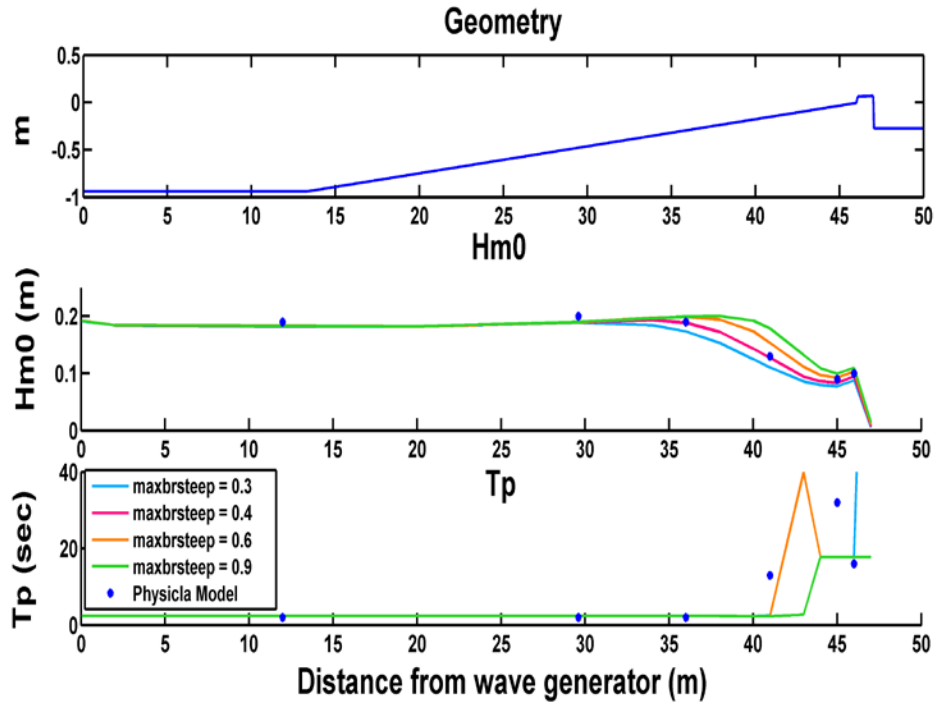

Figure 2.16 *Model geometry (top panel), Hm0 wave height (middle panel) and peak period (bottom panel) for XBeach (drawn lines) and the physical model (dots); sensitivity for parmeter maxbrsteep.*

Overtopping rate

The instantaneous discharge *qx* was monitored at the end of the crest and averaged over time. In Figure 2.17 the time series of the overtopping discharge is shown, indicating a situation of frequent overtopping. In Figure 19 a snapshot is shown of the water level during one of the overtopping events.

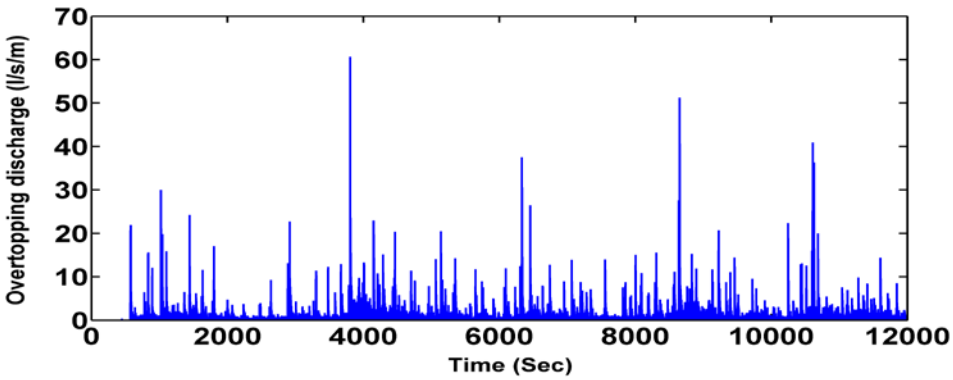

Figure 2.17 *Instantaneous overtopping discharge at end of the crest*

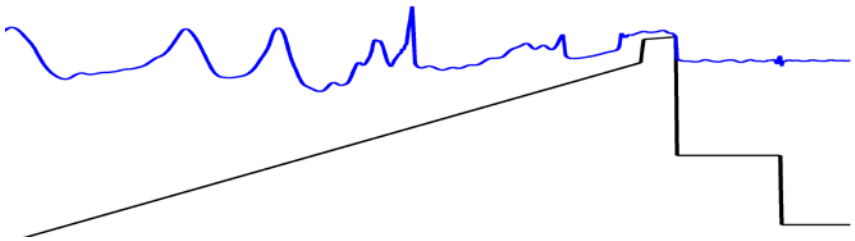

Figure 2.18 Snapshot of water elevation during an overtopping event

In Table 5 the mean overtopping discharge is given for different values of the roughness and *maxbrsteep* parameter. Values for a *maxbrsteep* value of 0.4 are close to the observed value of 0.58 l/s/m; for the default setting of 0.6 the values are somewhat overestimated.

Table 2.4 Mean wave overtopping results in combined sensitivity analysis of Chezy coefficient and maximum wave breaking steepness parameter

	Chezy coefficient				
maxbrst	45	49	55	66	99
0.3			0.41		
0.4	0.62		0.65		
0.6		0.9	0.95	1.01	1.05
0.9			1.49		

Conclusion

Overall the model shows correct behavior for this case; the transformation of wave spectra towards very shallow water is predicted correctly and the overtopping rate is predicted accurately for calibrated parameter settings that reflect the correct wave height decay; when default settings are applied the overtopping discharge is overestimated by a factor 1.5, which can be considered acceptable in view of the large scatter usually found in the measurements. The bed roughness has only a limited effect on the overtopping rate.

2.3.2 Validation with Clash database

Introduction

In many of the RISC-KIT case studies the problem area has a shallow foreshore; however, this is not always the case, especially during storm surge conditions. Therefore it is useful to test the applicability of XBeach for representing overtopping over dikes and breakwaters without a particularly shallow foreshore.

To this end, a collection of 551 relatively simple cases was taken from the CLASH database (Steendam et al., 2004), of which 366 points from very recent tests by Victor et al. (2011) with accurate second-order wave generation and active reflection compensation. Comparison of XBeach with this large number of data points provides an insight in the predictive capacity of the model and into the bias and scatter.

CLASH database

The CLASH database consists of an excel sheet with over 10,000 data points described by a name, 8 wave parameters (Hm0,Tp,Tm and Tm-1,0 at deep water and at the toe of dike or breakwater), 18 parameters defining the structure, two factors defining the reliability and the complexity, and the measured mean overtopping rate. With the help of Prof. J.W. van der Meer 511 reliable and simple cases were selected for this validation.

Setup of the simulations

An automated Matlab procedure was set up for this validation with the following simple structure:

- Read all records from the excel sheet
- For all records:
    - Separate incoming and outgoing waves and compare incoming wave height with target wave height
    - Adjust input wave height
    - Rerun XBeach for 500 waves
    - Analyze mean overtopping discharge
- Store results and produce scatter plot

With the help of the parameter *depthscale* which was set at 20 m divided by the water depth near the wave maker all possible scale effects in the numerical model were avoided, since all criteria such as the drying/flooding criterion *eps*, are scaled with depthscale.

The grid size varies from *dxmax=Ldeep/50* to *hdeep/50*; in deep water 50 cells per wave length are used and in shallow water and on the slope the grid size equals the offshore depth divided by 50; for small-scale tests in 50 cm this means the horizontal resolution on the slope is 1 cm; for Delta Flume conditions of approx. 5 m depth this is still a fine 10 cm resolution.

Separating the incoming and reflected waves in the numerical results was done using time series of water level and velocity, the short wave celerity and the local water depth, according to the formula:

$$z_{s,in} = \left(\frac{c}{h} z_s + u\right)\frac{h}{2c} \qquad z_{s,out} = z_s - z_{s,in}; \tag{0.5}$$

where z_s is the water level, u the velocity, c the celerity and h the water depth. The incoming wave height produced by XBeach was typically in the order of 10% below the target value; adjusting for this led to improved results. An example of the results of such an analysis is given in Figure 2.19. The incident wave height from this analysis

at half a wavelength from the boundary was made to match the observed Hm0deep from the CLASH database.

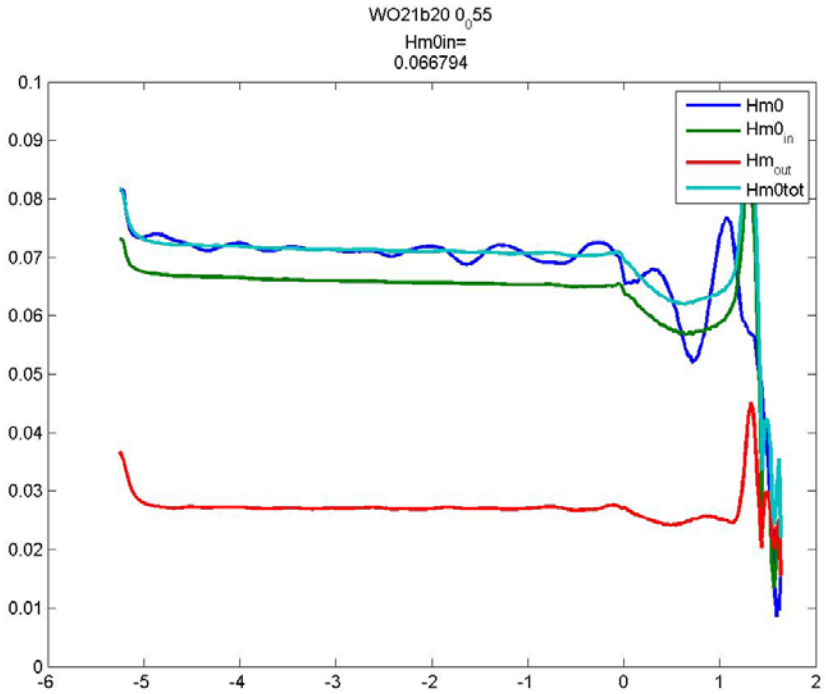

Figure 2.19 Analysis of incoming, reflected and total wave heights in numerical experiment; Hm0 refers to total wave signal; Hm0tot is based on the sum of the incident and reflected wave energy.

Results

The mean overtopping discharges for both measurements and simulations were converted to the same prototype scale, taking a 20 m offshore depth as prototype scale. This allows an easy comparison of the different tests related to the prototype overtopping discharge, regardless of the scale the tests were carried out at.

In Figure 2.20 the simulated discharge rates are plotted against the measured ones for all tests. Clearly, there is a good correspondence for the higher overtopping rates, with the model performance clearly suffering below values of 10-20 l/m/s. Part of the scatter may be explained by the fact that older tests are included, which for instance do not have reflection compensation. However, as the results for the cases from Victor et al (2011) show in Figure 2.21, there is still a problem in representing low overtopping rates.

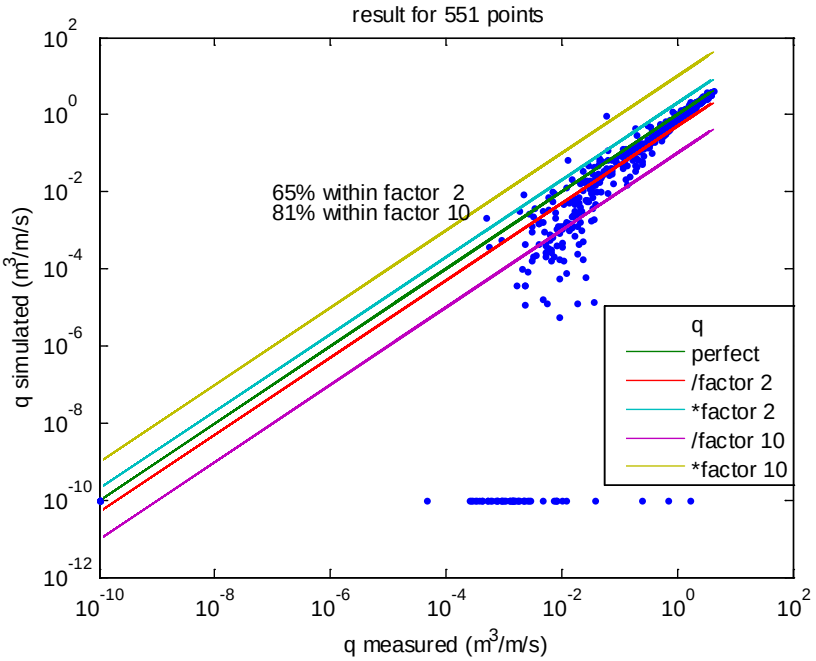

Figure 2.20 Comparison of measured and simulated mean overtopping discharges for all selected cases; results scaled up to prototype scale.

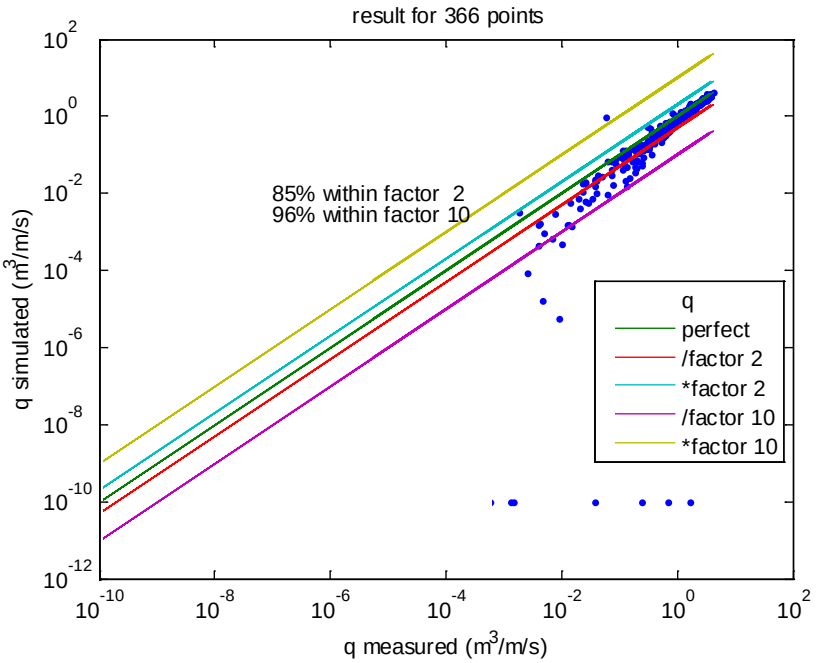

Figure 2.21 Comparison of measured and simulated mean overtopping discharges for all cases in Victor et al. (2011); results scaled up to prototype scale.

Conclusions

For relatively high overtopping discharges the non-hydrostatic XBeach performs quite well; recent, high-quality data are reproduced for 91% within a factor 10 and 85% within a factor 2. These rates improve for increasing overtopping rates.

However, for relatively low overtopping rates of less than 10-20%, the model systematically underestimates the overtopping rates. This will be the subject of further studies.

2.3.3 Developing morphological non-hydrostatic model

Introduction

For cases with relatively steep beach slopes or with combinations of hard structures and beaches, it can be desirable to use the non-hydrostatic mode of XBeach, including morphological changes.

For gravel beaches, McCall et al. (subm.) developed an entirely new coarse-sediment transport formulation to be used in combination with wave-resolving modeling. In the following we first do a preliminary check to test the differences between a surf-beat and a wave-resolving approach with respect to morphological change, if we just apply the same transport formulations. We then investigate theoretically where the models would differ and what changes, if any, would need to be made in order to synchronize the formulations between both formulations.

Test case LIP11D 2E

The first test case concerns one of the standard cases from the XBeach skillbed, the profile evolution over 8 hours of the LIP11D test 2E. In the figure below we see a surprisingly good agreement between the models and with the measurements. For this case, both the surf-beat and non-hydrostatic mode are valid, and apparently the sediment transport gradient differences are small. We'll analyse this further on.

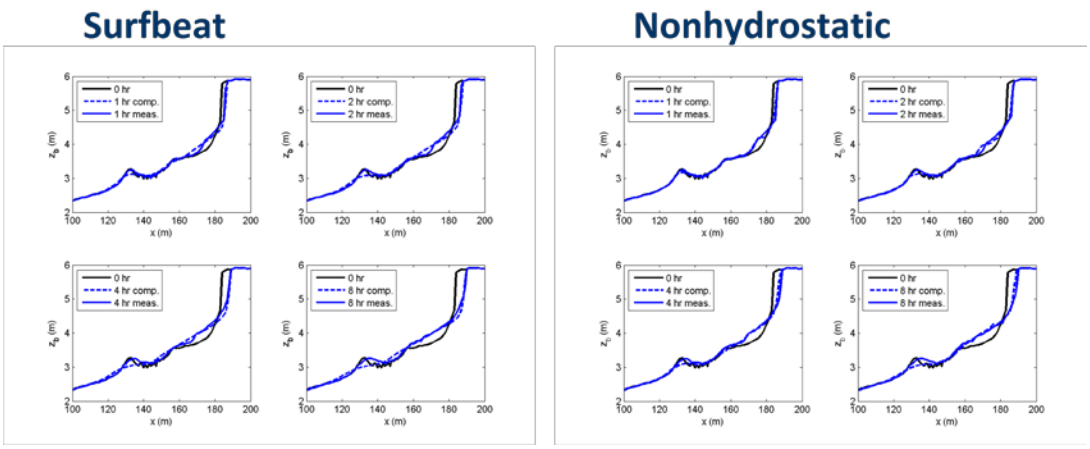

Figure 2.22 Comparison of profile evolution between surfbeat and nonhydrostatic approaches, LIP11D test 2E.

Test case Tordera sand barrier

The Tordera sand barrier on the Ebro delta is a typical example of a relatively steep profile, in the order of 1:10, where both a surf-beat and a wave-resolving approach can be considered. We compared both approaches for a storm (storm 215), with wave conditions at the peak of the storm Hm0=8.3 m and Tp=13.5 s, from a database of storms provided, with the initial profile, by J. Jimenez. The duration of the simulation was six hours. In **Figure *2.23*** we compare the results according to the surf-beat and non-hydrostatic approaches, for exactly the same model settings. Although there are subtle differences (e.g. in the non-hydrostatic mode the beach slope remains slightly milder and a rudimentary sandbar appears), the overall erosion pattern is quite similar. Here the differences may well be due to differences in the hydrodynamics, since for instance the run-up will generally be higher in the non-hydrostatic approach, since for this steep profile there is some energy in the incident-band swash.

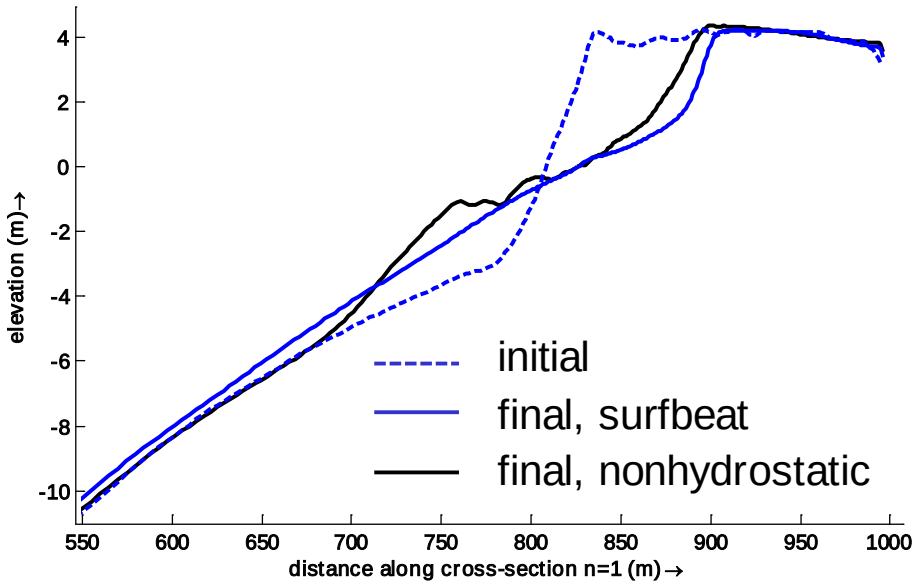

Figure 2.23 Comparison of profile evolution between surf-beat and non-hydrostatic approaches, Tordera barrier, Spain.

Analysis of the differences in the sediment transport

The suspended sediment transport (which is dominant) is computed by the advection-diffusion equation:

$$\frac{\partial hC}{\partial t}+\frac{\partial hC\left(u^{E}+u_{a}\right)}{\partial x}+\frac{\partial}{\partial x}\left[D_{h}h\frac{\partial C}{\partial x}\right]=\frac{hC_{eq}-hC}{T_{s}} \qquad (0.6)$$

The following differences can be noted between the surf-beat and non-hydrostatic modes:

- The concentration C varies on the scale of the wave groups in the surf-beat approach but within the wave period in the non-hydrostatic case.
- The term u^E stands for Eulerian-mean velocity. In the surf-beat case, this time-varying velocity varies on the wave group scale and the undertow due to the short waves is included in it. In the non-hydrostatic case it includes the undertow effect automatically, and also the skewness term; depending in how much the concentration lags behind the velocity, the asymmetry is also included automatically.
- The term u_a is an artificial advection velocity that is tuned to represent the effects of skewness and asymmetry on the transport. It is necessary in the surf-beat approach but set to zero in the non-hydrostatic case.
- The diffusion term D_v acts on the slowly-varying concentration in the surf-beat case, but on the intra-wave variations in the non-hydrostatic

case. This will tend to reduce the peakedness of the concentration and potentially could reduce the skewness/asymmetry effects.

- The equilibrium concentration C_{eq} depends on the slowly-varying velocity u^E and the orbital velocity u_{rms} in the surf-beat case:

$$C_{eq} = \frac{A_{sb} + A_{ss}}{h}\left(\left(|u^E|^2 + 0.64u_{rms}^2\right)^{0.5} - u_{cr}\right)^{2.4} \tag{0.7}$$

  In the non-hydrostatic case the orbital velocity is included in the u^E and therefore has a somewhat greater effect on the equilibrium concentration.

- The time scale in the source term T_s is given by:

$$T_s = \max\left(T_{sfac}\frac{h}{w_s}, T_{s\max}\right)s \tag{0.8}$$

  This means that the concentration lags from 0.5 to several seconds behind the velocity. This may well reduce the skewness/asymmetry effect, especially in deeper water, using the default settings of Tsfac=0.1 and Tsmin=0.5. To bring them more in line, the Tsfac could be reduced when running in non-hydrostatic mode.

All in all these differences are not spectacular and their effect can be reduced by calibration, comparing surf-beat and non-hydrostatic approaches. It is in principle possible to separate long and short waves in the non-hydrostatic mode in order to apply exactly the same formulations. Before doing more fundamental research on the actual response of the sediment concentrations to short and long wave motions, we do not recommend implementing such changes, due to their inherent uncertainties.

In the figure below we show the result of a simple calibration exercise to bring the non-hydrostatic and surf-beat results in line, in this case by calibrating the *facua* parameter used to scale the skewness and asymmetry effects. Assuming that the nonhydrostatic model provides the most accurate solution regarding the wave asymmetry and skewness effect, we can easily get the surf-beat solution to match closely by increasing the *facua* setting. However, the actual intra-wave transport processes related to skewness and asymmetry are much more complex than we currently account for, so calibration will be required for both model types.

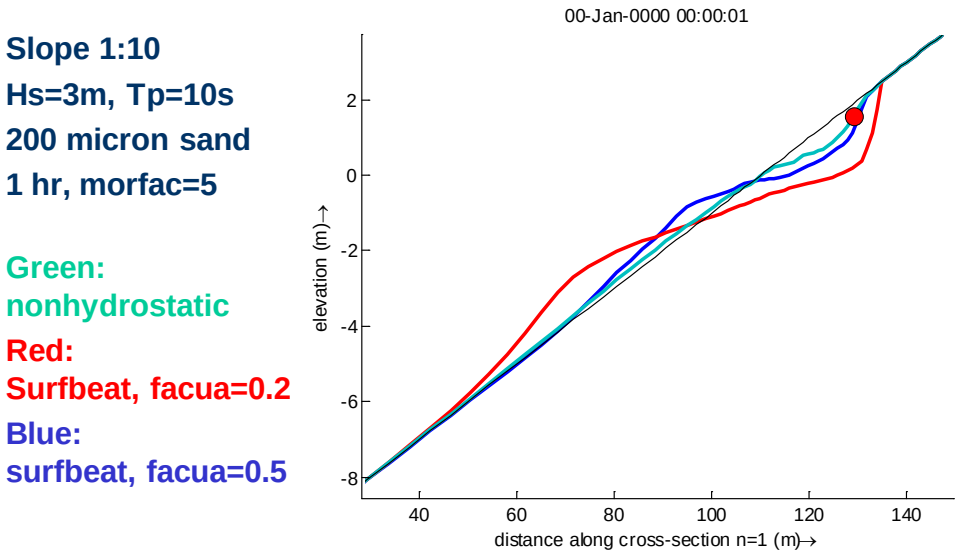

Figure 2.24 Example calibration of profile behavior

Conclusions

Inspection of some example test cases and of the sediment transport formulations reveals that there are relatively subtle differences in sediment transport between the surf-beat mode and the non-hydrostatic mode. Further research into the actual response of sediment concentrations to skewed, asymmatric short waves and long waves combined is advisable, but in the meantime applying the sediment transport formulation of Van Thiel - Van Rijn in the non-hydrostatic case appears to lead to acceptable differences between both modes of operation.

A recommendation we are likely to carry out in the near future is to recalibrate the model settings for the non-hydrostatic mode using the full XBeach skillbed.

2.4 Developments and validation (2D hydrodynamic field validation)

2.4.1 Delilah field test

In the surf-beat approach of XBeach the short-wave motion is solved using the wave action equation which is a time-dependent forcing of the HISWA equations (Holthuijsen et al., 1989). This equation solves the variation of the short-waves envelope (wave height) on the scale of wave groups. It employs a dissipation model for the use with wave groups (Roelvink, 1993) and a roller model (Svendsen, 1984) to represent momentum stored at the surface after breaking. These variations, through radiation stress gradients, exert a force on the water column and drive longer period waves (infragravity waves) and unsteady currents.

Using the surfbeat mode is necessary when the focus is on swash zone processes rather than time-averaged currents and setup. It is fully valid on dissipative beaches, where the short waves are mostly dissipated by the time they are near the shoreline,

on intermediate beaches and during extreme events where the swash motions are still predominantly in the infragravity band and so is the run-up.

Under the surf-beat mode there are basically two different options to deal with wave refraction:

1. Resolving the wave refraction 'on the fly' using the propagation in wave direction space. This option is possible for arbitrary bathymetry and any wave direction. The user must specify the width of the directional bins for the surfbeat mode (keyword: *dtheta)* This approach is in this memo referred to as '**multi_dir'** or '**default'**
2. Solving the wave direction at regular intervals using the stationary solver, and then propagating the wave energy along the mean wave direction (keyword: *single_dir = 1*). The user must now specify a single directional bin for the instationary mode (*dtheta = <thetamax-thetaminn>)* and a smaller bin size for the stationary solver (keyword: *dtheta_s)*. This approach is in this memo referred to as '**single_dir'**. A single_dir simulation is a factor 2 faster than the multi_dir approach.

In this section multiple XBeach simulations have been carried out in order give a verification of performance of both the hydrodynamic and morphologic results. The focus will be the differences between the multi directional and single directional simulations.

Area of interest

In order to verify the 2DH hydrodynamics of XBeach when forced by directionally-spread short waves, a simulation is set up to compare model results to field measurements. In this case the DELILAH field experiment at Duck, North Carolina is selected as a suitable test location. The period that is modelled is October 13th 1990, which was a stormy day, between 16:00 and 17:00 hours. The significant wave height at 8 m water depth was 1.81 m, with a peak period of 10.8 s and a mean angle of incidence of -16° relative to the shoreward normal. This period is selected because the wave conditions are energetic enough to generate a significant infragravity wave component and the incident wave spectrum is sufficiently narrow-banded to justify the assumptions in the model boundary conditions. The model is forced with the wave spectrum measured at 8 m water depth (Birkemeier et al., 1997). A measured tidal signal is imposed on the model boundaries of which the mean level is 0.69 m above datum.

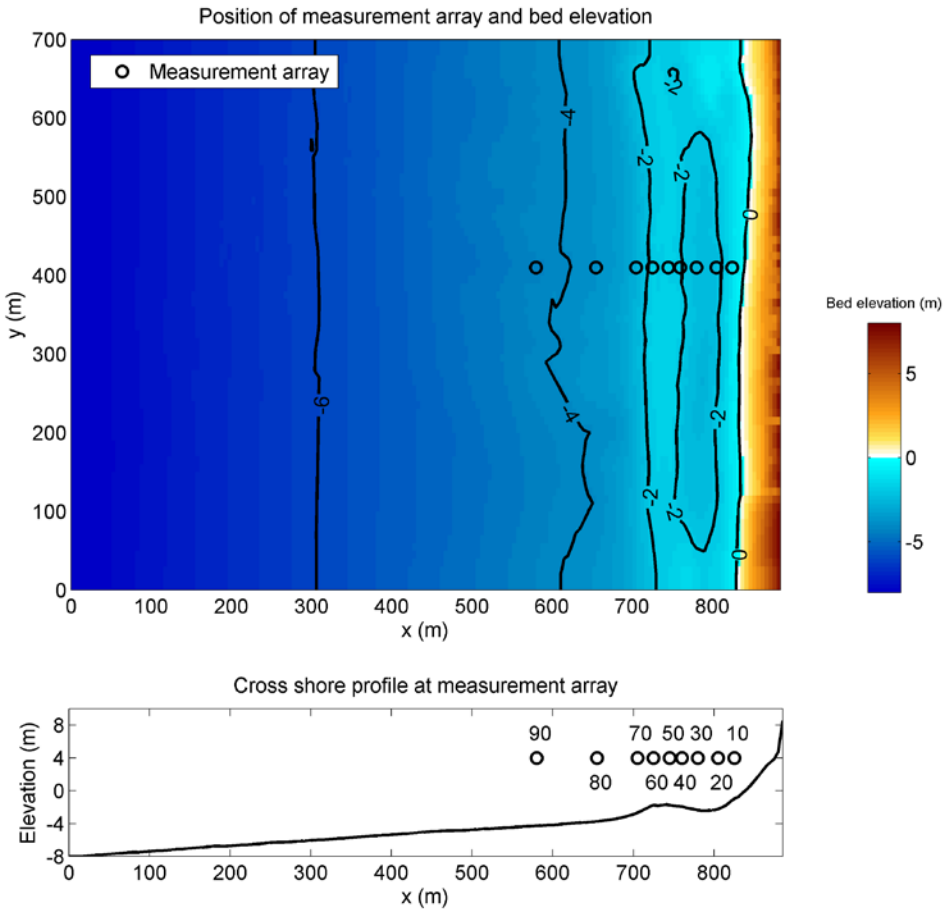

Figure 2.25 *The bathymetry and measurement locations of Delilah*

Model set-up

The model is directly taken from the skill bed (Deltares, 2013), but the settings other than the default values are presented:

- The model has been widened in order to limit the effect of the shadow zones.
  - For the surf-beat model this results in a grid of 177 x 200 cells with the dimensions of 850m in cross-shore and 2100m in longshore.
  - For the non-hydrostatic model the grid is made finer in order to reproduce the hydrodynamics accurately. A grid of 421 x 1252 cells with the dimensions of 2400m (till a depth of 20m for a kh>1) in cross-shore and 2100m in longshore is applied. This results in a resolution of 20 grid points per wave length.
- A CFL condition of 0.6 and a eps of 0.001m are applied
- The breaker formulation of Roelvink (1993) is applied with a gamma of 0.52 and gammax of 3.0.

Appling a frequency filter

When comparing the different results per formulation it is first of all important to address the fact that a filter based on a specific frequency band is applied and follows

the bands specified by van Dongeren et al. (2003). There are three different waves taken into account:

1. High frequency waves (HF): with a frequency higher than 0.5 s^{-1}
2. Low frequency waves (LF): with a frequency from 0.05 till 0.5 s^{-1}
3. Very low frequency waves (VLF): with a frequency lower than 0.05 s^{-1}

In the following we will only discuss the HF and LF bands as they are most relevant to the RISC-KIT project.

Spatial behavior: diffusive processes (spreading of energy)

In the comparison of the time and spatial behavior of both a multi_dir and a single_dir simulation, the wave group will spread out quicker (diffusion) in the simulation with multi_dir. In a single_dir simulation this is not the case. The result is twofold: 1) The long wave have higher forcing in a single_dir simulation and therefore the Hrms,LF will increase. 2) Short waves have higher peaks and lower troughs. The result can be found in Figure 2.33.

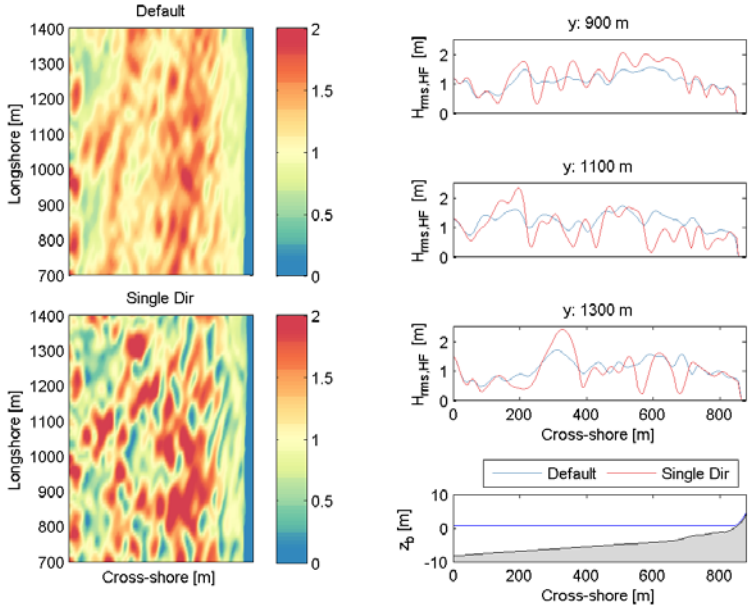

Figure 2.26 Spatial plot of the room-mean-square short wave height for a multi_dir and single_dir simulation.

Secondly, it is also possible to evaluate the performance per simulation type per time-averaged wave type compared to the measurement data:

> **HF waves:** multi_dir and single_both represent the short wave height with good accuracy (R2 > 0.85). Interestingly, the single_dir option has negative bias. This is related with the fact that the wave groups will not spread as much in a single_dir simulation. Therefore waves will be more peaked. High waves will break, but the lower troughs remain. The non-hydrostatic option does not reproduce shoaling as accurately for this case. A likely cause is offshore wind leading to stronger shoaling before breaking.

LF waves: the multi_dir underestimates the low frequency wave height. The single_dir and the non-hydrostatic simulation represent these waves with a higher accuracy (R2 > 0.4) .

The results are shown in ***Table 2.6*** and **Figure 2.35**. In the latter also a simulation is included with the single_dir option and a first-order propagation scheme; this is clearly too diffusive and reduces the wave groupiness and hence the long waves too much.

Table 2.5 Comparison of the results for Delilah

Simulation types	**Hrms,HF R2**	**bias**	**Hrms,LF R2**	**bias**
Multi_dir	0.85	-0.06	0.36	-0.12
Single_dir	0.85	-0.12	0.40	-0.06
Non-hydrostatic	0.84	-0.12	0.49	0.02

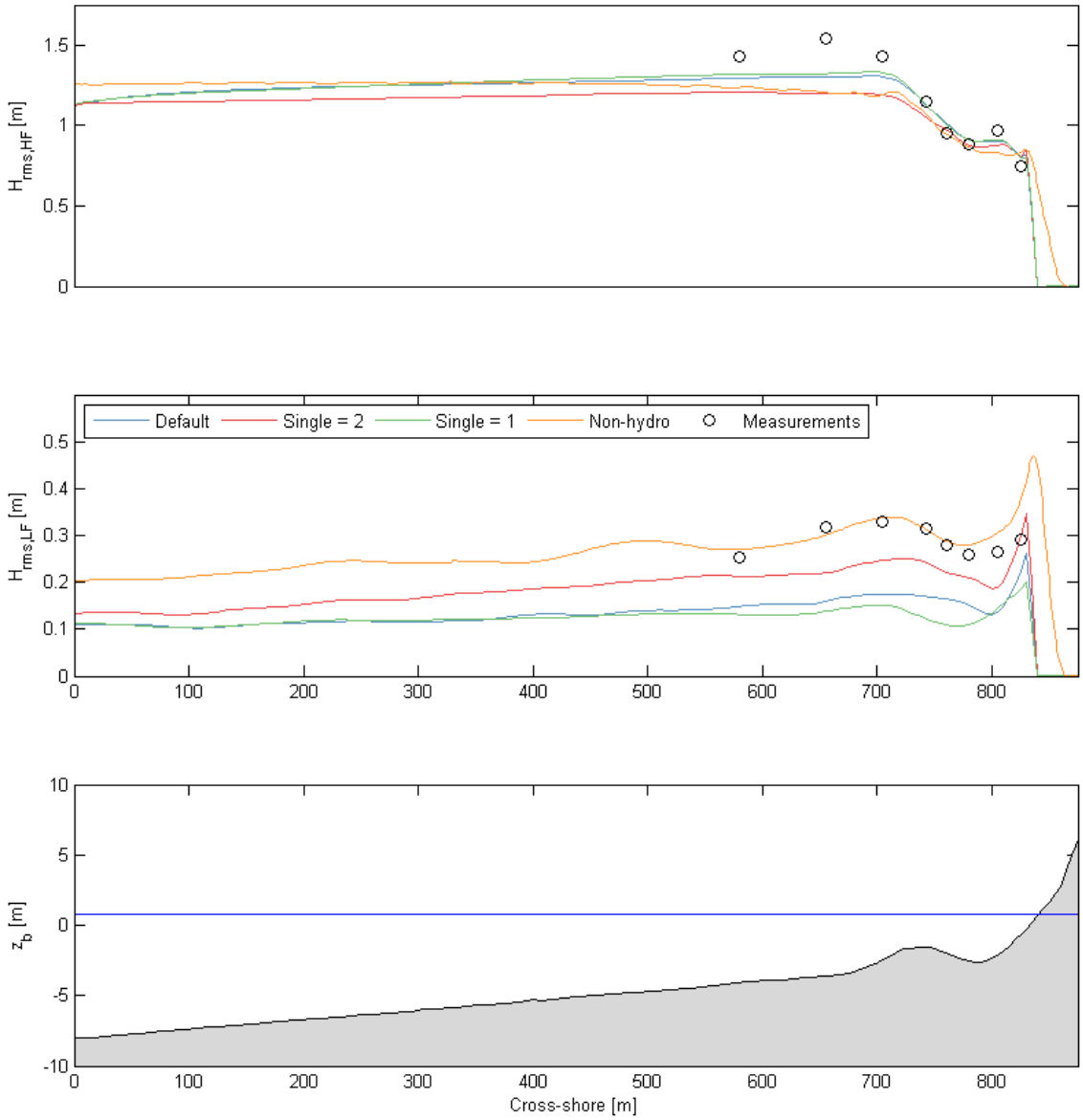

Figure 2.27 Comparison of the root-mean-square wave height (Hrms) for Delilah for both the high frequency part (upper panel) and the low frequency part (middle panel) for multiple simulation types as computed by XBeach (solid lines); default: multi-dir; single=2: single_dir, 2nd order scheme; single=1: single_dir with 1st order scheme; non-hydro: non-hydrostatic model.

Wave breaker formulations

In this paragraph different wave breaking formulations for both the multi_dir and single_dir are applied. The wave forcing in the shallow water momentum equation is obtained from a time-dependent version of the wave action balance equation.

There are in three different wave breaking formulations (D_w) implemented in XBeach which can be applied for non-stationary waves:

1 Formulation of Roelvink (1993)
2 Adaptation of first formulation (coded Roelvink1)

3 Adaptation of first formulation, according to Daly et al. (2012) (coded RoelvinkDaly)

For all the different simulations carried out (both multi_dir and single_dir) the following conclusions can be drawn (see Table 2.7 and Figure 2.35):

- The most accurate reproduction (in terms of R2) of the high frequency waves is found with the Roelvink1 (Roelvink, 1993) formulation. This is both the case for multi_dir and single_dir. The bias of the single_dir simulation is the highest, this is due to the fact the wave groups stay intact (lower wave trough level). The reason why Roelvink1 results in the best reproduction of the high frequency waves is probably a calibration issue.
- The most accurate reproduction (in terms of R2) of the low frequency waves is found with the Roelvink_Daly formulation (Daly et al, 2012) . This is both the case for multi_dir and single_dir. The long waves are underestimated by multi_dir and overestimated with single_dir. Probably for the generation of long waves the fact that waves stop breaking after some point is of importance.
- Combing both HF and LF waves the formulation of Daly et al. (2012) results in the closest fit with the measurement data, since the values for HF are all quite close, but there is quite some variation for the infragravity waves.

Table 2.6 Comparison for the result for Delilah for the different wave breaking formulations

Breaker formulation		**Multi_dir**		**Single_dir**	
		Hhf	**Hlf**	**Hhf**	**Hlf**
Roelvink1	R2	0.86	0.25	0.85	0.29
	Bias	-0.06	-0.09	-0.12	-0.03
Roelvink2	R2	0.84	0.28	0.84	0.30
	Bias	0.01	-0.08	-0.06	-0.00
Roelvink_daly	R2	0.82	0.34	0.84	0.35
	Bias	-0.05	-0.07	-0.08	0.03

The result per breaking formulation are:

- Roelvink1 results in a good reproduction of the wave heights in the surf zone, but shoaling is reproduced to a limited extent. On top of that long waves are not forced enough.
- Roelvink2 results in more shoaling and more long waves, however the wave heights in the surfzone are overestimated.
- Roelvink_daly results in the most shoaling and thus generates more long waves.

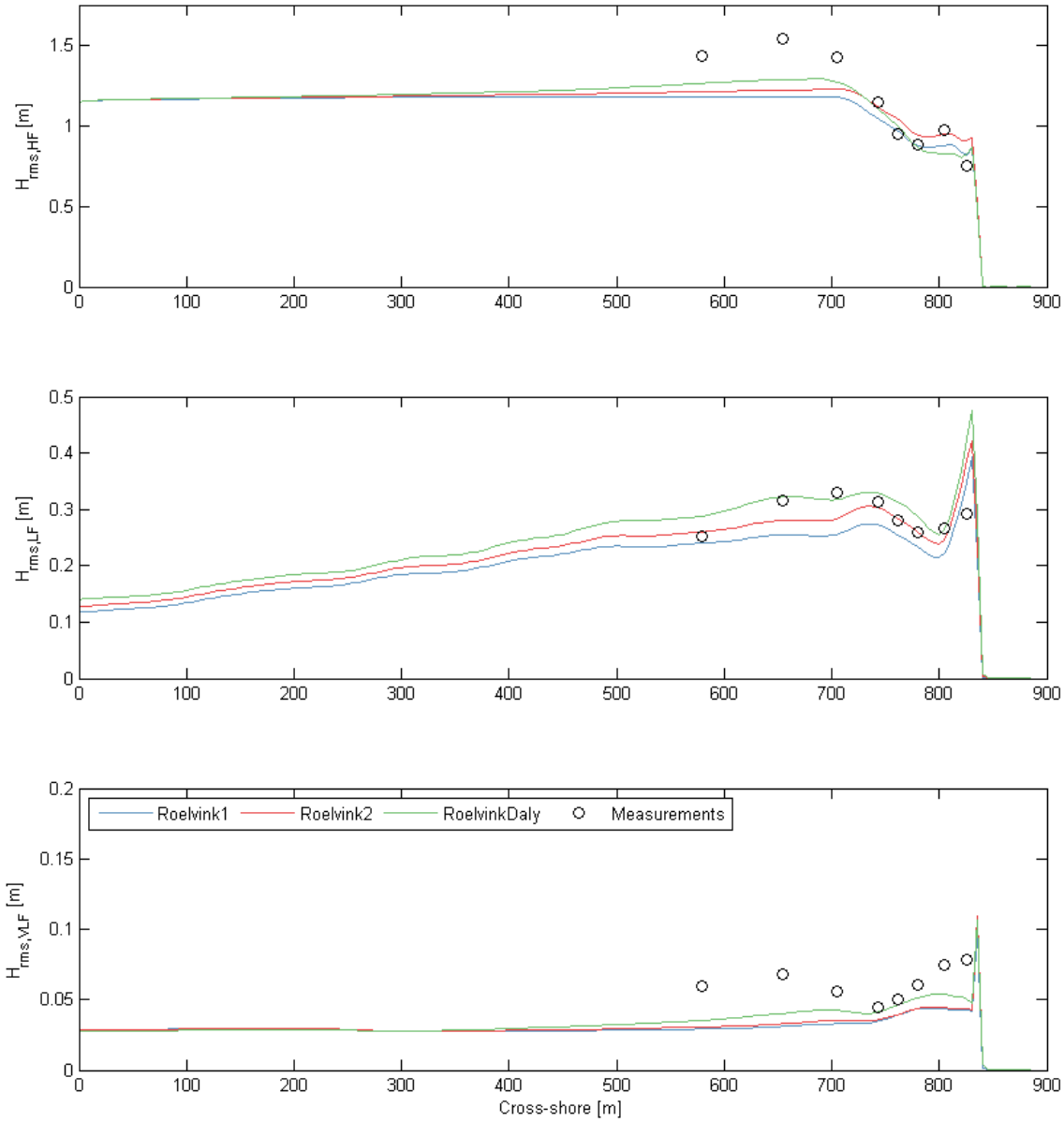

Figure 2.28 The high frequency waves (top panel), low frequency waves (middle panel) and VLF waves (lower panel) presented for a single direction (single_dir=1) simulation in XBeach for Delilah

2.4.2 Praia de Faro, Vousdoukas et al.

Introduction

Vousdoukas et al. (2012) carried out extensive fieldwork to measure wave run-up and beach slopes at Praia de Faro, Algarve, Portugal between September 2009 and April 2010. The run-up was measured using a video system from which time stacks of water lines were extracted; with the help of 40 accurate beach surveys the water line horizontal positions could be converted to vertical levels and the R2% run-up level could be determined. Simultaneous wave height, period and direction information

was obtained from a nearby wave buoy and water levels from a nearby tidal station. The details of the measurement procedures are given in Vousdoukas et al. (2012).

We obtained from Dr Vousdoukas a relevant selection of 301 data points where all this information was synchronized and quality checked. An important parameter included in this series was the slope of the intertidal beach.

Vousdoukas et al. (2012) investigated several possible empirical parameterizations starting from Stockdon et al (2006); we have used his optimum formulation as a reference to evaluate the XBeach results.

Setup of XBeach simulations

As in the previous section, an automated Matlab procedure was set up for this validation with the following structure:

- Read all records from the provided matlab datafile *data4Dano_2015_02_12.mat*
- For all records:
    - Create a schematized profile with the right swash zone slope; see the extreme mild and steep slopes in Figure 2.25;
    - Create a grid with grid sizes decreasing from 10 m at offshore end to 1 m in the swash zone;
    - Interpolate schematized values to the grid;
    - Write XBeach grid and profile files; in case of 2D runs extend the profile uniformly in longshore direction;
    - Generate params.txt and jonswap.txt input files;
    - Run XBeach for 30 minutes;
    - Analyze R2% run-up height
- Store results and produce time series and scatter plots with regression lines

All input data, observations and Matlab scripts to generate the results are stored on the XBeach repository, under folder *testcases/Vousdoukas2012_Praia_de_Faro.*

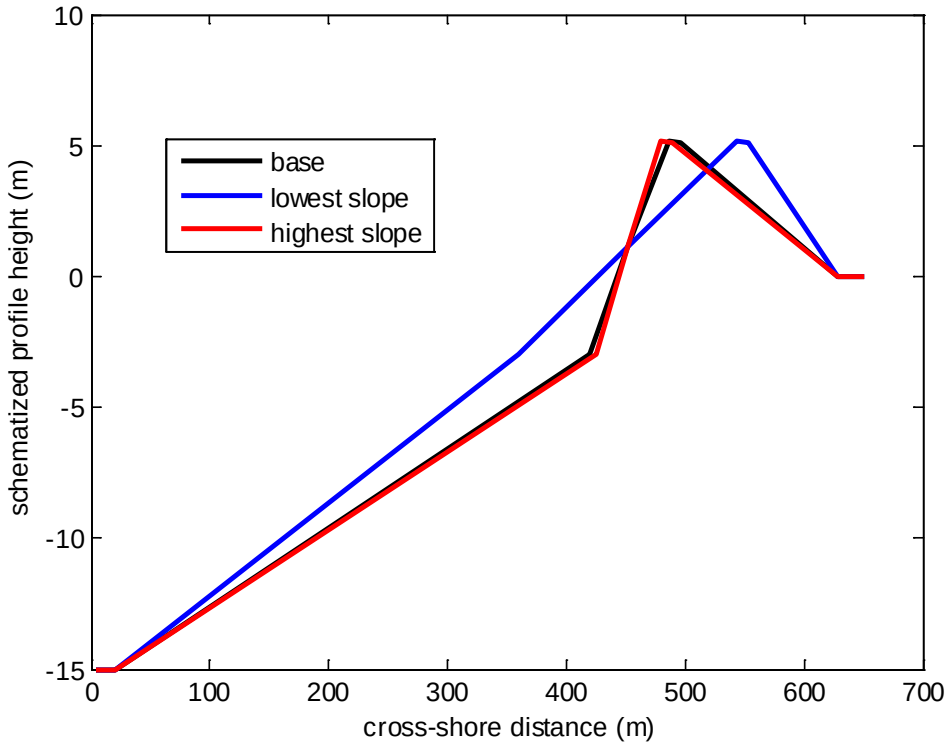

Figure 2.29 base, mildest and steepest profile for simulations

All cases were run in XBeach 1D (both non-hydrostatic and surf-beat mode) and in 2DH (surf-beat mode).

The beaches at Faro have a relatively steep upper beach slope, following an approximately 1:30 slope from -15m to -3 m. Under such circumstances the assumption that most of the swash zone energy is in the infragravity band is questionable, as there will be some energy in the incident band. Therefore for the 1D runs we compared both with the non-hydrostatic and surf-beat mode.

The 1D runs were carried out without directional spreading and assuming the waves to be perpendicular to the beach. For the 2DH runs we could only carry out the simulations in surf-beat mode, as these runs would have required a very high resolution and hence computation time.

Results

In Figure 2.26 the wave conditions, water levels, beach slopes and resulting R2% run-up height computed with the non-hydrostatic mode simulations are shown and compared with the observed R2% and those predicted by Vousdoukas et al. (2012), eq. 7:

$$R_{2\%} = 0.53\beta\left(H_0 L_0\right)^{1/2} + 0.58\xi\sqrt{\frac{H_0^3}{L_0}} + 0.45 \qquad (0.9)$$

Here H_0 is the deep water Hm0 wave height, L_0 the deep water wave length and ξ the Iribarren parameter.

The comparison of the series of measurements, the empirical predictions and the non-hydrostatic model results shows a significant overestimation of the run-up heights for this case, very likely due to the absence of directional spreading and because the waves were modeled as perpendicular to the beach.

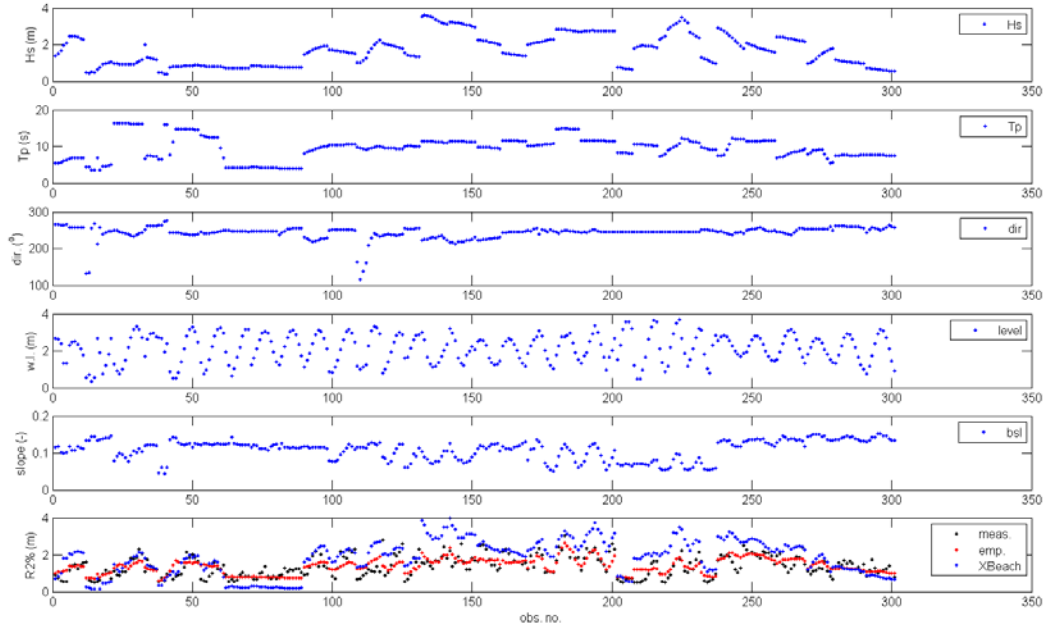

Figure 2.30 Simulations for Vousdoukas et al, 1D non-hydrostatic mode. Panels from top to bottom: Hs wave height, Tp wave period, mean wave direction (not used in 1D), water level, beach slope in swash zone, R2% run-up height.

The scatter plots for this situation, shown in Figure 2.27, show a trend line for the simulations against the predictions with a slope that is 28% too steep if the trend line is forced through zero; if the zero intercept is free, the slope of the trend line is only overestimated by 6%.

By comparison, the empirical relationship slightly under predicts the trend in case the regression line is forced through zero; when the zero intercept is let free, we see that the regression line has a slope of 0.51, thus severely underestimated; this is particularly important for extreme conditions.

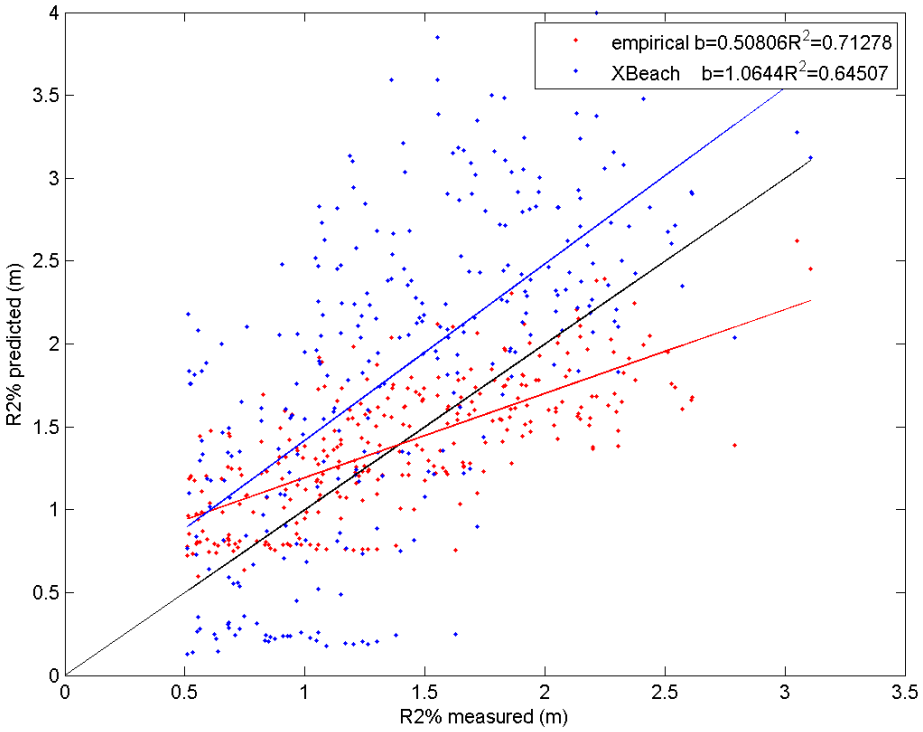

Figure 2.31 Observed vs simulated R2% run-up height and regression curves; 1D non-hydrostatic.

For the 1D surf-beat mode simulations the results are shown in Figure 2.28 and Figure 2.29. A similar pattern can be seen for this case, where the trend line for the XBeach results against the observations now has a slope that is 15% too high, both when the line is forced through zero and for the case of a free zero intercept.

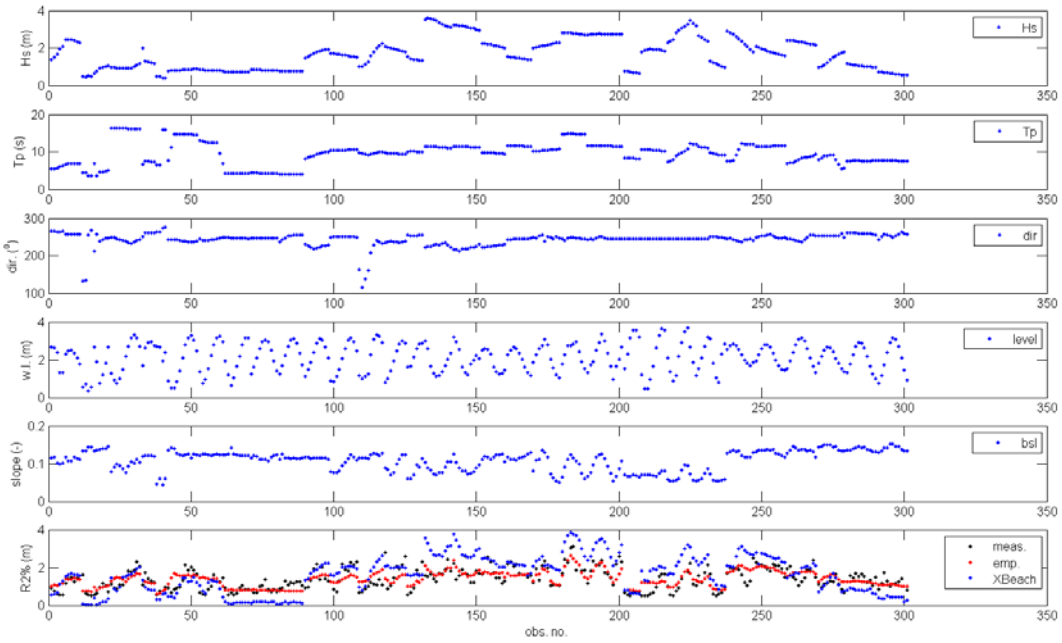

Figure 2.32 Simulations for Vousdoukas et al, 1D surf-beat mode. Panels from top to bottom: Hs wave height, Tp wave period, mean wave direction (not used in 1D), water level, beach slope in swash zone, R2% run-up height.

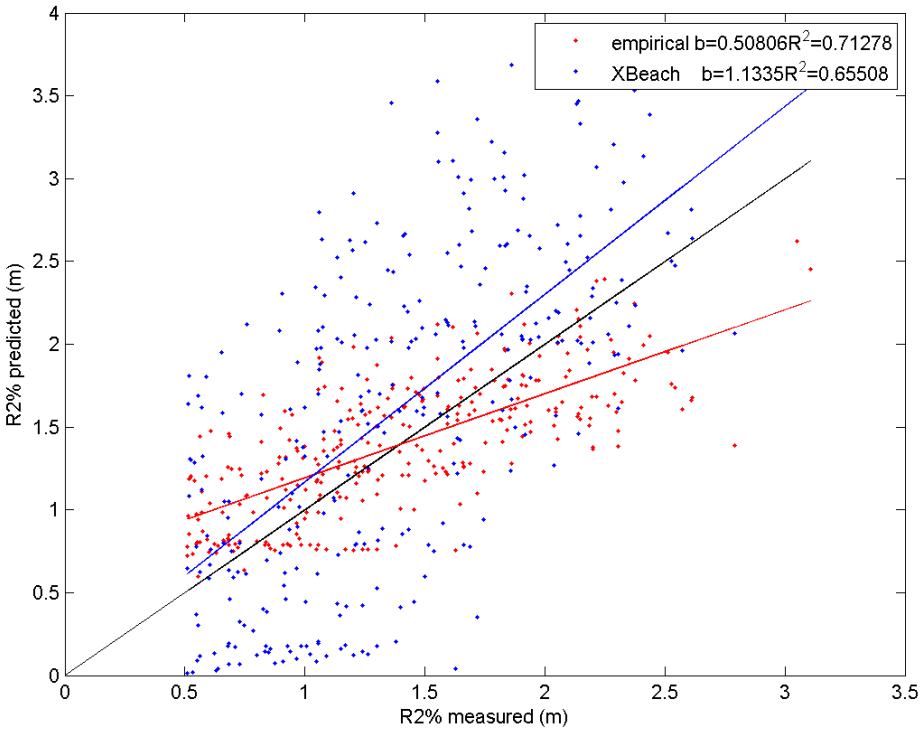

Figure 2.33 Observed vs simulated R2% run-up height and regression curves; 1D surf-beat.

The 2DH runs were carried out in 'single_dir' mode, where the short wave energy is propagated along the mean wave directions computed by stationary wave runs carried out only once. The main purpose of running in 2DH mode was twofold:

1. To take into account effects of directional spreading
2. To take into account the effect of wave refraction

Various experiments were carried out to find an optimum alongshore grid resolution and extent. The result of this was that a longshore grid size of 50 m and alongshore extent of 1000 m sufficiently captured the typical size and shape of the wave groups so further refinement or extension in longshore direction was not necessary. This is quite convenient since the simulation time for such runs of a 30-min duration is in the order of some minutes.

The results for these simulations are shown in Figure 2.30 and Figure 2.31. Clearly, the simulated R2% values much more closely match the observed ones. As the scatter plots show, though considerable scatter remains, the trend is quite accurate, both in the regression line forced through zero and the one with a free zero intercept.

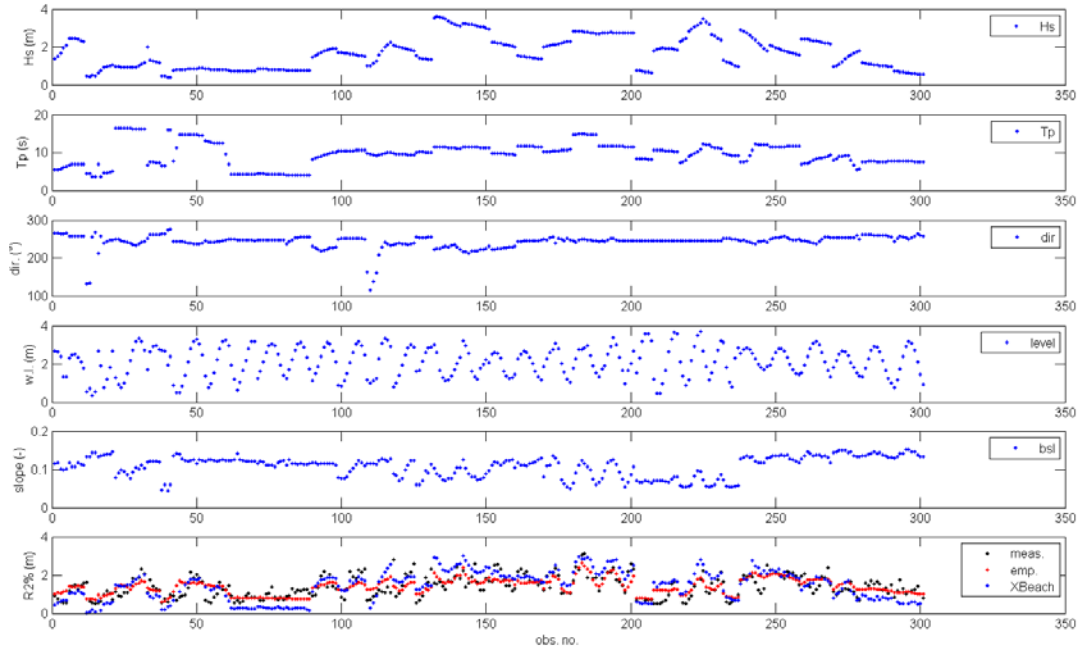

Figure 2.34 Simulations for Vousdoukas et al, 2D surf-beat mode. Panels from top to bottom: Hs wave height, Tp wave period, mean wave direction, water level, beach slope in swash zone, R2% run-up height.

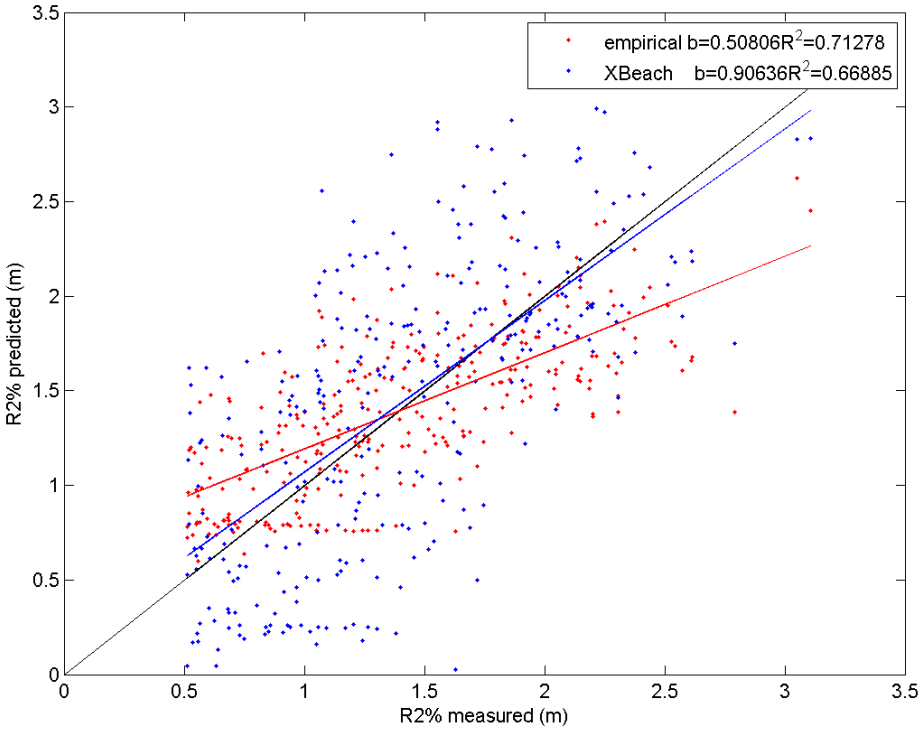

Figure 2.35 Observed vs simulated R2% run-up height and regression curves; 2D surf-beat.

2.4.3 Conclusions on 2DH hydrodynamic validation

For the hydrodynamic reproduction of **Delilah** the implementation of single_dir will result in a high frequency wave field that is much more 'peaked'. This is the result of the wave groups, since resolving the wave refraction with mult_dir can lead to some smoothing out of the wave groupiness since the waves from different directions do not interfere but their energy is summed up. A single_dir approach will preserves the groupiness of the waves better and therefore leads to more forcing of the infragravity waves. The effect for the Delilah case was a better reproduction of the LF waves than the multi_dir approach.

When varying over the different wave breaking formulations implemented in XBeach the formulation of Daly et al. (2010) represents both the HF and LF waves in the most accurate matter. This is both valid for multi_dir and single_dir. Variation of the breaking parameters in the formulations will have a limited impact in the total reproduction of the waves, since often a better reproduction of the HF waves will result in a worse reproduction of the LF waves and the other way around.

For the case of **Praia de Faro** a large number of observed R2% run-up values were compared with XBeach in three different modes. Intercomparison between non-hydrostatic and surfbeat-mode simulations in 1D showed that both lead to an overestimation of run-up values, by 30% and 15% respectively. An efficient 2DH mode of simulation was found with the 'single_dir' option and a relatively coarse

longshore resolution (50 m), which accurately reproduced the trend in the observations, with negligible bias.

2.5 Developments and validation (2D morphodynamic)

2.5.1 Hurricane Sandy (2012)

Simulations

In order to verify the 2DH morphodynamics of XBeach when forced by directionally-spread short waves via single_dir, two simulations are set up to compare model results to field measurements. In this memo two field cases during Hurricane Sandy are used:

- Fire Island, Long Island, NY. This area is not inhabited, but does have some vegetation on top of the barrier. This model is taken from De Vet et al. (2015).
- Camp Osborne, Brick, NJ. This area is residential area with multiple hard elements in the barrier. This model is taken from Nederhoff et al. (2015).

The wave conditions and surge level time series at the offshore boundary of the XBeach model were derived from a large-scale Delft3D model of Hurricane Sandy. The surge level in the bay is based on nearby measurement data. This is applicable for both models.

Hurricane Sandy originated from the Western North Atlantic Ocean in October 2012. The storm caused flooding, wind and wave damage. It first swept in the Caribbean and continued across the entire East Coast of the United States, as can be seen in Figure 2.37. During Hurricane Sandy the state of New York and New Jersey were most severely hit (National Hurricane Center, 2012). Sandy made landfall on October 29, 2012 at 12:00 PM UTC during spring tide near Atlantic City, NJ. Hurricane Sandy caused wide-spread erosion of the coastal system as well as barrier island breaching at several spots. Sandy was the second costliest hurricane in the United States history with a total of 68 billion dollar in property damage (National Hurricane Center, 2012)

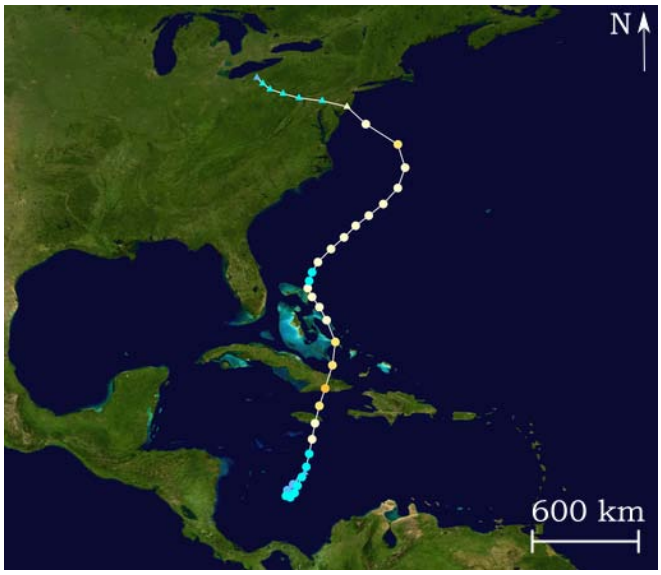

Figure 2.36 Track of Hurricane Sandy. Traveling from South to North Sandy interacted with a nontropical weather system transforming from hurricane to a post-tropical cyclone. Colors from blue to red represents hurricane intensity. [Sources: National Hurricane Center (2012) and Wikipedia

2.5.2 Fire Island

Area of interest

Fire Island, NY, was heavily impacted during this event, evidence by the formation of breach channels, large-scale washover and destruction of houses and infrastructure. De Vet et al. (2015) investigate and improve the capacity of XBeach to hindcast breaching and over-wash and dune erosion (eg. Sallenger, 2000) along a 2 km stretch of the coastline.

Figure 2.37 Aerial photo prior to (left; July 3rd 2012) and after (right; November 4th 2012)the hurricane (Source: Google Earth)

Model set-up

The Manning roughness formulation is introduced as the non-depth dependent Chézy formulation (default value of 55 $m^{1/2}/s$) since it was thought to be less realistic for large depth differences. Since some vegetation is present on top of the barrier island,

the bed roughness is locally increased to reduce the flow velocities at these locations to account for this vegetation. A Manning value of 0.04 is applied in the vegetated regions (determined by satellite imagery), a value of 0.02 is used elsewhere. On top of that the asymmetric onshore sediment transport component (*facua*) is enhanced from 0.1 to 0.2. The rest of XBeach parameters are left untouched (default).

Results

When the area of interest is simulated with XBeach, the morphological model is capable of reproducing the response of the barrier in a practical breaching case during Hurricane Sandy in an accurate way with a BSS in the order of 0.229 till 0.248 and a bias of 0.102 till 0.076m for respectively multi_dir and single_dir. The reason for this small shift is the fact that the single_dir model erodes 7.8% more (from 129 to 138 m3/m). The mean dune top level will also be 0.16m lower.

It is interesting to see the spatial bed level plot (Figure 2.39), since the increase in erosion volume from the single_dir simulation due to the increase in LF waves will result in a lot of spatial changes in the bed levels (see lower right panel). First of all the bar at NAVD88 -5m will erode more in a single_dir simulation. Secondly, over-wash fans develop differently. At some spots there is less development (y = 100-200 and 700m), but in other areas more (y = 500 m). Thirdly, the location of the breaching is reproduced with single_dir (y = 500 m). This in contrast to multi_dir and de Vet et al. (2015) where a breach at a major over-wash fan (y = 700m) occurred. For the development of the breach it is important that the area is 'weakened' enough during the peak of the storm since backwash will erode this area more which eventually can result in a breach. The exact reasoning for these features is not completely clear with the simple analysis in this report. It is hypothesized that in the single_dir simulation the (higher) HF waves will dissipate (break) on the sand bar. This will result in the erosion seen at this sand bar. However the higher LF waves will still be able to reach the shore. This will explain the extra erosion of 8%. It is however not clear why there is less erosion / less development of over-wash fans at some spots in the model.

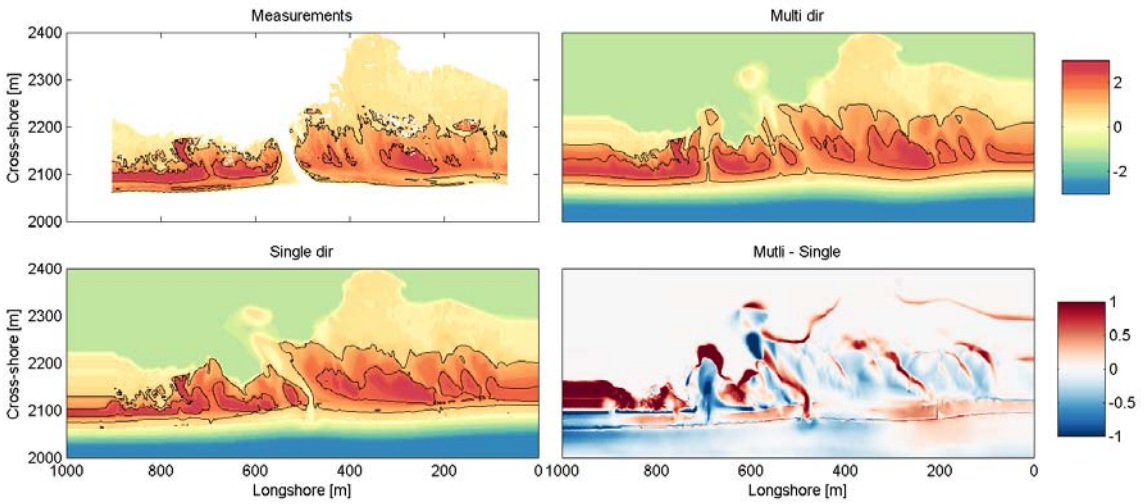

Figure 2.38 Spatial post bed levels and erosion/accretion plots after the storm event presented for the area of interest at Fire Island. Spots without data are marked

grey. The black depth contours are provided at an elevation of 0 and 3m relative to NADV88.

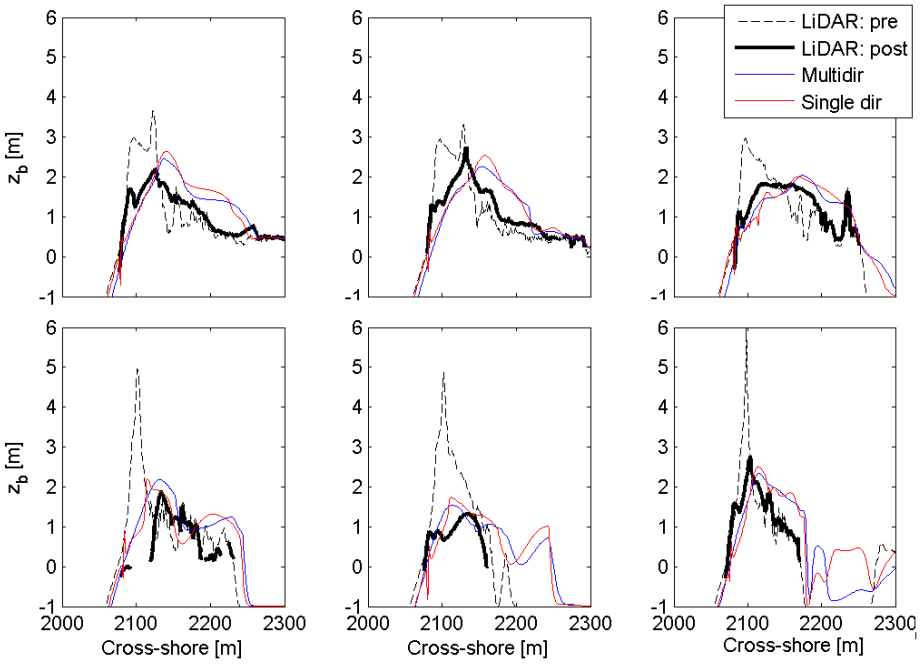

Figure 2.39 Post bed levels for various cross-sections: pre-Sandy, post-Sandy and calculated for multi_dir and single_dir for Fire Island. The legend is valid for all individual subfigures. Note: the profiles for multi_dir and single_dir are quite similar.

2.5.3 Camp Osborne

Area of interest

Camp Osborne is one of the well-developed beaches of Brick, NJ. However, in October 2012 nearly all 118 bungalows were either swept away by the Sandy storm surge or ravaged by a fire. The latter is suspected to be caused by a gas leak in the rubble. Only seven bungalows, a large condo and a parking lot were salvageable. The hypothesis that was proved with XBeach was that the condo had a longshore effect and resulted in an increase in erosion volume at adjacent locations (Nederhoff et al., 2015).

Figure 2.40 Pre- and post-storm oblique aerial photographs of the impact of Hurricane Sandy (2012). Pictured is a condo in the barrier of Camp Osborne, Brick, NJ. Pictures are taken on the 21st of May 2009 and the 05th of November 2012. Taken from the U.S. Geological Survey (USGS) website.

Model set-up

XBeach was calibrated for the over-wash regime by applying a two-step calibration approach, The first step is to increase the asymmetric onshore sediment transport component (*facua*). The second step is increasing the roughness of the barrier island.

- A value of *facua* of 0.25 (0.1 default) is applied.
- A good fit with the LiDAR was found when a Chezy value of 30 $m^{1/2}/s$ is applied on the barrier island and the default value of 55 $m^{1/2}/s$ is used in the rest of the model.

The rest of XBeach parameters are left untouched (default).

Results

When the condo area is simulated with XBeach, the morphological model is capable of reproducing the response of the interaction between hard-soft in a practical over-wash case during Hurricane Sandy in an accurate way with a $BSS_{erosive}$ in the order of 0.892 till 0.881 and a bias of -0.204 till -0.270 for respectively multi_dir and single_dir. The reason for this small shift is the fact that the single_dir model erodes 6.0% more (from 135 to 142 m3/m). The fact that the multi directional spreading simulation results in a higher skill score and lower bias is a matter of calibration. Compared to Fire Island, the hindcast of Camp Osborne is somewhat easier since there is only limited over-wash and no offshore sand bar.

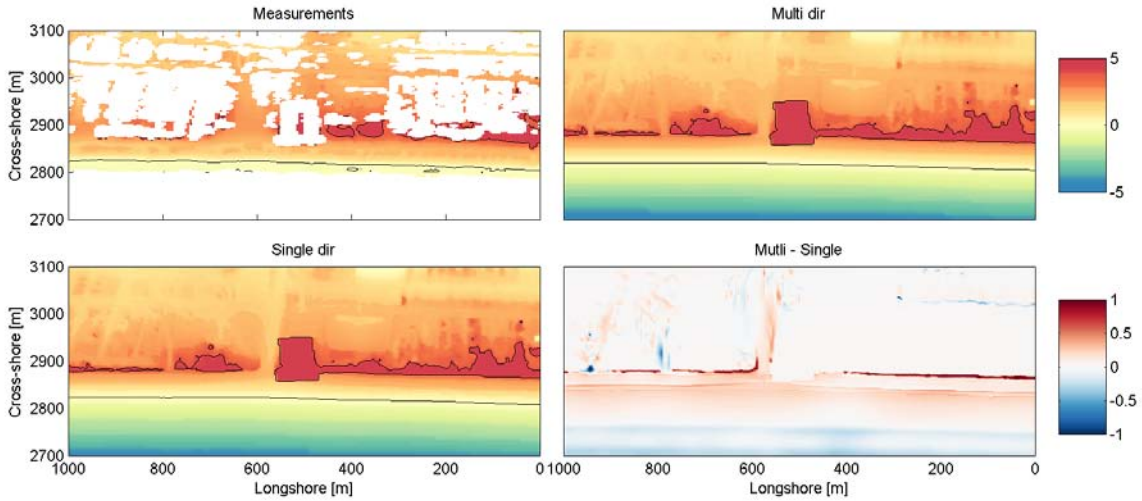

Figure 2.41 Spatial post bed levels and erosion/accretion plots after the storm event presented for the area of interest at Camp Osborne. Spots without data are marked grey. The black depth contours are provided at an elevation of 0 and 3m relative to NADV88.

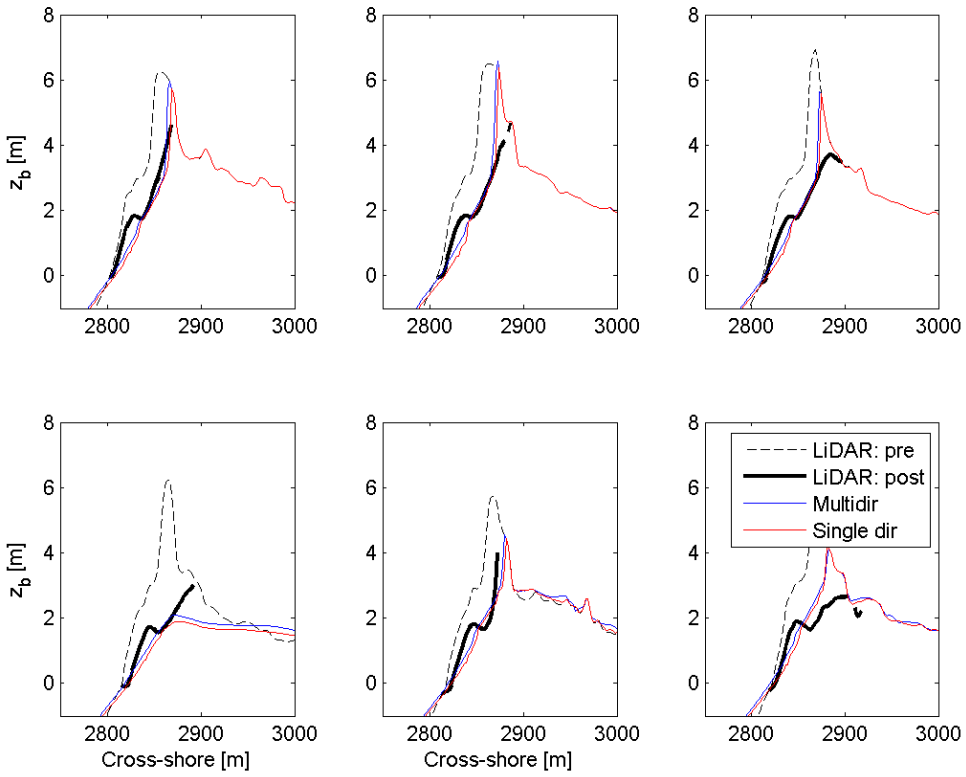

Figure 2.42 Post bed levels for various cross-sections: pre-Sandy, post-Sandy and calculated for multi_dir and single_dir for Camp Osborne. The legend is valid for all individual subfigures. Note1: the peaks in the profiles (mainly y < 400m) seem unrealistic and are related to the avalanching algorithm. Note2: the profiles for multi_dir and single_dir are quite similar.

2.5.4 Conclusions on 2DH morphodynamic validation

The main objective was to make a comparison between resolving the wave refraction 'on the fly' (*multi_dir*) or via the use of a stationary solver (*single_dir*). The main reason for the recent implementation of single_dir was the computational time, since a single_dir simulation is about two times as fast as a multi_dir simulation.

For the **morphodynamic reproduction** of two field cases of Hurricane Sandy (2012) one can conclude that the stronger wave groupiness in the single_dir simulation will result in more erosion. For Fire Island the erosion volume increased with 7.8%. This is the direct effect of the increase in long wave height. On top of that, there were some interesting changes in the bed levels. For example the location of breaching was correctly modelled with single_dir and *not* with the multi_dir simulation. For Camp Osborne the erosion volume increased with 6.0%. The reason for this lower percentile compared to Fire Island is the fact that only limited over-wash occurred.

Overall one can conclude that a single_dir simulation in XBeach will result in stronger wave groupiness than a multi_dir simulation. This will result in higher infragravity waves. For the field case of Delilah single_dir resulted in a better reproduction of the hydrodynamics. The effect of different wave breaking formulations and variations in breaking parameters resulted in a similar pattern for both multi_dir and single_dir. For

both types the formulation of Daly et al. (2010) resulted in the best reproduction of the wave heights. The erosion volume has increased with 6-8% when using single_dir instead of multi_dir. Models calibrated with multi_dir could result in a lower skill score when applying single_dir, however for Fire Island single_dir resulted in an increase of the predictive skill.

2.6 Main findings and recommendations

The XBeach model code has been critically reviewed and optimized. The implementation for parallel computing using MPI and domain decomposition has been made more accurate through the use of double border rows and columns, and more scalable due to the fact that less variables need to be communicated and the output is put on a separate process.

The development of the 'single_dir' short wave propagation scheme gives an additional speedup of roughly a factor of two. All in all the model has become significantly faster for most applications; the speed gain increases for increasing numbers of cores.

The non-hydrostatic model within XBeach was shown to perform adequately for run-up and overtopping, though for very small overtopping discharges XBeach tends to underestimate. The morphological behavior of the non-hydrostatic mode was shown to be remarkably similar to that of the 'surfbeat' mode for dune erosion and over-wash cases.

Finally, the model was validated hydrodynamicalle and morphodynamically against a number of field datasets in Praia de Faro (Portugal), Duck NC (USA), Fire Island (USA) and Camp Osborne (USA). The overall conclusion here is that the performance is strongly improved with the 'single_dir' scheme and that underestimation of wave run-up as experienced by Stockdon et al. (2014) is much reduced.

It is recommended to revisit the datasets used by Stockdon et al. (2014) with the new 'single_dir' option.

2.7 References

Birkemeier, W. A., Donoghue, C., Long, C. E., Hathaway, H. K., & Baron, C. F. (1997). 1990 DELILAH nearshore experiment: Summary report. Technical Report CHL-97-4-24, U.S. Army Corps of Engineers. Field Research Facility, 21.

Daly, C., Roelvink, J. A., van Dongeren, A. R., van Thiel de Vries, J. S. M., & McCall, R. T. (2012). Validation of an advective-deterministic approach to short wave breaking in a surf-beat model. Coastal Engineering, 60, 69–83. doi:10.1016/j.coastaleng.2011.08.001

De Vet, P. L. M., McCall, R. T., Den Bieman, J. P., Stive, M. J. F., & Van Ormondt, M. (2015). Modeling dune erosion, over-wash and breaching at Fire Island (NY) during Hurricane Sandy. Proceedings Coastal Sediments, San Diego, CA.

Deltares. (2012). XBeach skillbed (sep 2013), 2871.

Holthuijsen, L. H., Booij, N., & Herbers, T. H. C. (1989). A prediction model for stationary, short-crested waves in shallow water with ambient currents. Coastal Engineering, 13(1), 23–54. doi:10.1016/0378-3839(89)90031-8

National Hurricane Center. (2012). Hurricane Sandy Advisory Archive.

Nederhoff, C. M., Lodder, Q. J., Boers, M., Den Bieman, J. P., & Miller, J. K. (2015). Modeling the effects of hard structures on dune erosion and over-wash - a case study of the impact of Hurricane Sandy on the New Jersey coast. Proceedings Coastal Sediments, San Diego, CA.

Roelvink, J. A. (1993). Dissipation in random wave group incident on a beach. Coastal Engineering, 19, 127–150.

Sallenger, A. (2000). Storm impact scale for barrier islands. Journal of Coastal Research, 16(3), 890–895.

Stockdon, H.F., Thompson, D.M., Plant, N.G., and Long, J.W., 2014, Evaluation of wave run-up predictions from numerical and parametric models: Coastal Engineering, 92, 1-11.

Svendsen, I. A. (1984). Wave heights and set-up in a surf zone. Coastal Engineering, 8, 303–329. doi:10.1016/0378-3839(84)90028-0

Suzuki, Tomohiro, Toon Verwaest, Wael Hassan, William Veale, Johan Reyns, Koen Trouw, Peter Troch, and M. Zijlema. (2011) "The applicability of SWASH model for wave transformation and wave overtopping: A case study for the Flemish coast." In Proc. 5th Int. Conf. Advanced Computational Methods Engineering (ACOMEN 2011), Liège, Belgium, 11pp. 2011.

Steendam, G. J., van der Meer, J. W., Verhaeghe, H., Besley, P., Franco, L., & Van Gent, M. R. A. (2004). The International Database on Wave Overtopping. In Proceedings of the 29th International Conference on Coastal Engineering (Vol. 1–4, pp. 4301–4313). Singapore.

Van Dongeren, A. R. (2003). Numerical modeling of infragravity wave response during DELILAH. Journal of Geophysical Research, 108(C9), 3288. doi:10.1029/2002JC001332

Victor L., Troch P., (2011). Wave overtopping at smooth impermeable steep slopes with low crest freeboards. Journal of Waterway, Port, Coastal and Ocean Engineering.

Vousdoukas M.I., Wziatek D., Almeida L.P. (2012). Coastal vulnerability assessment based on video wave run-up observations at a mesotidal, steep-sloped beach. Ocean Dynamics (2012) 62:123-137. DOI 10.1007/s10236-011-0480-x

Zijlema, M., Stelling, G. S., & Smit, P. B. (2011). SWASH: An operational public domain code for simulating wave fields and rapidly varied flows in coastal waters. Coastal Engineering, 58(10), 992–1012. doi:10.1016/j.coastaleng.2011.05.015

3 Development and validation of hierarchical models of storm wave energy dissipation

3.1 Introduction

The objective of this Chapter (see also Section 1.3) is to develop an improved model for saltmarsh of storm wave energy dissipation across a hierarchy of small, intermediate and large spatial scales, corresponding to <10m, , >10-30m , and 30m - 1,000m respectively. We begin at the intermediate scale, then proceed to the large scale and finally discuss effects at the small scale.

Recent years have seen the increasing recognition of wave dissipation by vegetation in aquatic and coastal environments. This realization stems from growing field evidence of wave attenuation, both in saltmarshes (e.g. Möller et al. 1999, 2001), brackish marsh reedbeds (Möller et al. 2011) and other types of vegetation (Kobayashi et al. 1993; Mendez et al. 1999; Paul and Amos 2011; Bouma et al. 2014). The ability of vegetation, particularly saltmarsh, to dissipate waves is clearly important when storm surges inundate these shallow intertidal areas and storm waves propagate across hydraulically rough surfaces. Predicting this dissipation, however, relies on accurate representation of marsh vegetation canopies within existing shallow water wave models. One of the difficulties in doing so arises from the complex nature of these vegetation canopies. The success in modeling dissipation over assemblages of cylindrically shaped, relatively evenly spaced, plants (such as *Spartina* or *Juncus* spp.; see e.g. Mendez and Losada 2004; and Ozeren et al. 2014) arises from the fact that such elements are relatively easily captured in mathematical models of (bulk) drag exerted on water flow. In reality, however, salt marsh vegetation often consists of mixed plant canopies with an arrangement of plant assemblages controlled by surface elevation and the related parameters of inundation frequency/duration ('hydroperiod') and salinity gradients. In addition, canopies are often characterized by vegetation 'clumps' forming spatially varied (on scales of metres) canopy characteristics, and are occupied, at least in the higher elevation zones of more mature marshes, by often complex (and woody/shrubby) vegetation types (such as *Atriplex* spp). It is thus necessary to find representations of these complex vegetated surfaces within existing numerical models that more accurately reflect the wave dissipation process across a hierarchy of scales. The key first step in the new model has been to introduce a variable drag coefficient to the vegetation module of the SWAN model. This reformulation, which can be compared against existing formulations of (bulk) drag, then needs to be both calibration and validated through the i comparison of model results with observed wave dissipation. Until recently, no studies have been available reporting on wave dissipation over salt marshes during extreme (greater than or equal to 2 m) water depths and waves (of the order of 1 m high) that can be expected to occur during storms in intertidal settings. The experiment reported by Möller et al. (2014), however, provides the opportunity to use observations of wave heights in front of and behind an approximately 40 m long experimental test section over a real salt marsh under simulated surge conditions. Model development and

calibration using the results of this study thus provide important insights into the wave energy dissipation process at the intermediate scale. In addition to this, field data from earlier studies is available for Stiffkey on the Norfolk coast, UK. Thus the application of the model to vegetation types found at this RISC-KIT case study site, and broadly typical of other NW European saltmarsh sites, becomes possible; the model can be 'scaled-up' to the larger scale. Finally, we can also 'scale-down' by exploring the finer scale controls (sub-meter) of variations in vegetation height. This is achieved by introducing the ability to spatially vary the vegetation height in the new model.

3.2 Implementing a modified wave dissipation model - due to vegetation based on empirical formulae

SWAN is a third generation wave model (Booij et al., 1999). It is based on the wave action balance equation and includes source and sink terms for energy generation, dissipation and non-linear interactions. The dissipation due to vegetation, $S_{ds,veg}$, is calculated within a vegetation module, SWAN-VEG. The current formulation for vegetation dissipation (Suzuki et al., 2011) uses a modified version of the Dalrymple (1984) wave dissipation formula by Mendez and Losada (2004).

The vegetation wave dissipation formula is based on the Morison equation, which assumes that the vegetation can be represented as a cylinder. The Morison equation describes the force of a wave on a cylinder which gives the energy dissipation due to the cylinder. The cylinder is inflexible; swaying and vibrations are not included explicitly in the model.

Mendez and Losada (2004) determined the energy dissipation based on the properties of the plants. The vegetation characteristics include the plant height, plant diameter, number of plants and the drag coefficient. The mean rate of energy dissipation due to vegetation per unit horizontal area (Mendez and Losada, 2004) is expressed as:

$$\langle \epsilon \rangle = \frac{1}{2\sqrt{\pi}} \rho \tilde{C_D} D_v N_v \left(\frac{gk}{2\sigma} \right)^3 \frac{\sinh^3 kH_v + 3\sinh kH_v}{3k\cosh^3 kh} H_{rms}^3 \tag{2.1}$$

where ρ is the water density, $\widetilde{C_D}$ is the bulk drag coefficient, D_v is the vegetation stem diameter, N_v is the number of plants per m², k is the mean wave number, $\tilde{\sigma}$ is the mean wave frequency, H_v is the vegetation height, and h is the water depth.

The bulk drag coefficient takes into account the approximations and physical processes not explicitly calculated by the formula. As such the drag coefficient is commonly used to calibrate the vegetation calculations.

In SWAN, the Mendez and Losada formula has been extended to include the full spectrum. The vegetation energy dissipation is expressed as a sink term:

$$S_{ds,veg} = -\sqrt{\frac{2}{\pi}} g^2 \tilde{C_D} D_v N_v \left(\frac{\tilde{k}}{\tilde{\sigma}} \right)^3 \frac{\sinh^3 \tilde{k}H_v + 3\sinh \tilde{k}H_v}{3k\cosh^3 \tilde{k}h} \sqrt{E_{tot}} E(\sigma, \theta) \tag{2.2}$$

where $S_{ds,veg}$ is the vegetation energy dissipation, g is the acceleration due to gravity, E_{tot} is the total wave energy, $E(\sigma,\theta)$ is the wave variance spectrum or energy density.

The SWAN vegetation module can differentiate between emergent and submerged vegetation, if emergent the height of the plant is specified as the water depth. The vegetation characteristics can be varied vertically, by dividing the vegetation into layers and specifying different vegetation characteristics for each layer. This allows the module to be used for vegetation which varies significantly with height, such as mangroves. In this case the energy dissipation for a layer i is defined as:

$$S_{ds,veg,i} = -\sqrt{\frac{2}{\pi}} g^2 \tilde{C_{D,i}} D_{v,i} N_{v,i} \left(\frac{\tilde{k}}{\tilde{\sigma}}\right)^3 \sqrt{E_{tot}} \frac{\left(\sinh^3 \tilde{k} H_{v,i} - \sinh^3 \tilde{k} H_{v,i-1}\right) + 3\left(\sinh \tilde{k} H_{v,i} - \sinh \tilde{k} H_{v,i-1}\right)}{3k \cosh^3 \tilde{k} h} E(\sigma,\theta) \quad (2.3)$$

$$S_{ds,veg} = \Sigma_{i=1}^{i} S_{ds,veg,i} \quad (2.4)$$

Whilst all the vegetation parameters can be varied vertically, only the number of plants can be varied spatially. If this is used with the height varying vegetation the number of plants changing with height is currently formulated so that only a factor of the number of plants can vary with height.

The drag coefficient is used to calibrate the model and is a fixed value in SWAN, this is typically a value that is species or situation specific. However, empirically the bulk drag coefficient has been shown to vary with the ambient wave conditions (Kobayashi et al. (1993), Mendez et al. (1999), Mendez and Losada (2004), Moller et al. (2014)). The drag coefficient has been expressed in terms of both the Keulegan Carpenter number, K_C:

$$K_C = \frac{U_m T}{D_v} \quad (2.5)$$

where T is the wave period.

and the stem Reynolds number, Re_v;

$$Re_v = U_m \left(\frac{D}{\nu}\right) \quad (2.6)$$

where U_m is the maximum bottom orbital velocity, D is the vegetation diameter, and ν is the kinematic viscosity ($\nu = 1 \times 10^{-6} m^2 s^{-1}$)

The drag coefficient expressed in terms of the stem Reynolds number, and is usually in the form:

$$C_D = a + \left(\frac{b}{Re_v}\right)^c \quad (2.7)$$

where a, b and c are empirically derived constants.

The empirical drag coefficient for various types of vegetation has been shown to vary with Re_v and K_C. Kobayashi et al. (1993), Mendez et al. (1999), and Paul and Amos (2011) found an empirical relationship between drag coefficient and the Re_v number for kelp, seaweed, and seagrass, respectively. Whilst Mendez and Losada (2004) and Jadhav et al. (2013) determined an empirical relationship between the drag coefficient and K_c number for kelp and saltmarsh, respectively.

Augustin et al. (2009) compared empirical relationships between Re_v and Kc over a saltmarsh, finding that the drag coefficient showed greater correlation with the Rev number under emergent conditions, whilst under near-emergent conditions the drag coefficient had a better correlation with K_C. Bradley and Houser (2009) found the drag coefficient is better described by the Re_v number in low energy conditions for seagrass. Whilst Sanchez-Gonzalez et al. (2011) showed the drag coefficient correlates closer to the K_C than Re_v over a seagrass meadow.

The recent study by Moller et al. (2014) has taken detailed wave dissipation measurements over a 39.44m section of saltmarsh in the large wave flume in Hannover. The experiment used storm surge conditions and a saltmarsh which is representative of those found in North West Europe. The drag coefficient was calculated using the Mendez and Losada (2004) formula and expressed as a function of the stem Reynolds number for regular and irregular waves.

Regular waves:

$$C_D = -0.046 + \left(\frac{305.5}{Re_v}\right)^{0.977} \tag{2.8}$$

Irregular waves:

$$C_D = 0.159 + \left(\frac{227.3}{Re_v}\right)^{1.615} \tag{2.9}$$

Existing studies have shown that submergence ratios are critical in determining wave dissipation over salt marshes (Mendez and Losada 2004; Möller et al. 2000). Vegetation height is thus a critical parameter. As mentioned above, vegetation canopies of salt marshes are characterized by spatially varying canopy characteristics, and particularly vegetation height. It thus makes good sense to allow the new SWAN vegetation module to work with spatially varying vegetation height.

3.2.1 Modified SWAN-VEG module for saltmarsh

The time varying drag coefficient and the spatially varying vegetation height are included in a new modified SWAN-VEG module. The Moller et al. (2014) formula for the drag coefficient for irregular waves is implemented in SWAN-VEG for calculating wave dissipation over a saltmarsh (under the option SALTMarsh). A user defined drag coefficient formula is also included, where the empirical coefficients a, b and c, (Equation 7) are defined in the SWAN steering file (under the option USER). This increases the use of the variable drag coefficient model modification for use with other vegetation and different types of saltmarsh.

The drag coefficient is calculated internally in the model using the Reynolds number which is calculated from the plant diameter and near bottom velocity. The near bottom velocity is dependent on the ambient wave conditions, and will vary across the vegetation. As the wave dissipates the bottom velocity will differ allowing the change in wave conditions to contribute to the calculation of wave energy dissipation.

The new modified SWAN-VEG module includes the previous formulation (under the option DALrymple), where the drag coefficient is fixed and specified in the steering file. This is the only SWAN-VEG option with vegetation characteristics that can vary by height.

Modified SWAN-VEG input data:

| -> DALrymple [height] [diamtr] [nstems] [drag]

|

VEGEtation < -> SALTMarsh [height] [diamtr] [nstems]

|

| -> USER [height] [diamtr] [nstems] [a] [b] [c]

The variables are defined as;

[height] the plant height (m). [height] is allowed to vary over the computational region to account for the zonation of the vegetation. If spatially variable, use the commands INPGRID VHEIght and READINP VHEIght to define and read the plant stand diameter. The value of [height] in this command will be multiplied with the horizontally varying plant density. If using the DALrymple option the height can be divided into different layers, and a value is then required for each layer.

Default: [height] =1

[diamtr] the diameter of each plant stand (m). If using the DALrymple option the diameter can vary with height, and a value for each layer is then required.

[nstems] the number of plant stands per square metre. [nstems] is allowed to vary over the computational region to account for the zonation of the vegetation. If spatially variable, use the commands INPGRID NPLANTS and READINP NPLANTS to

define and read the vegetation density. The value of [nstems] in this command will be multiplied with the horizontally varying plant density. If using the DALrymple option nstems can vary with height, and a value for each layer is then required.

Default: [nstems] =1

[drag] the drag coefficient per layer. Only used for the DALrymple option.

[a] empirically derived constant for the drag coefficient formula, $C_D = a + (b/Re_v)^c$

[b] empirically derived constant for the drag coefficient formula, $C_D = a + (b/Re_v)^c$

[c] empirically derived constant for the drag coefficient formula, $C_D = a + (b/Re_v)^c$

DALrymple – Wave damping due to vegetation is calculated by the modified Dalrymple (1984) formula by Mendez and Losada (2004).

SALTMarsh – Wave damping due to vegetation is calculated by the modified Dalrymple (1984) formula by Mendez and Losada (2004). The drag coefficient is calculated within the model according to the formula for irregular waves over a saltmarsh from Moller et al. (2014) $C_D = 0.159 + (227.3/Re_v)^{1.615}$.

USER – Wave damping due to vegetation is calculated by the modified Dalrymple (1984) formula by Mendez and Losada (2004). The drag coefficient is calculated within the model according to the formula $C_D = a + (b/Re_v)^c$. The parameters a, b and c are empirically derived coefficients that should be specified in the steering file.

New input grid:

VHEIght defines the input grid of the horizontally varying vegetation height (use with command VEGETATION)

3.3 Validation for the modified SWAN-VEG module

3.3.1 Validation of wave dissipation (intermediate spatial scale) due to vegetation within a wave flume

The new variable drag coefficient formulation within SWAN is validated against the Moller et al. (2014) large scale experiments. Moller et al (2014) used a 300m long, 5m wide, and 7m deep, wave flume to generate storm wave conditions and calculate dissipation over a 39.44m test section of saltmarsh (i.e. intermediate scale; Figure 3. 1). The vegetation used is typical of high southern North Sea saltmarsh, consisting of *Elymus athericus*, *Puccinella maritima*, *Atriplex prostrata.* The relevant plant characteristics are determined as mean values for the marsh section with, D_v = 0.00125m, H_v = 0.7m, N_v = 1225. The results presented here use test conditions with a water depth of 2m, and irregular waves with H_s=0.19 – 0.9m and T_p = 2 – 6s.

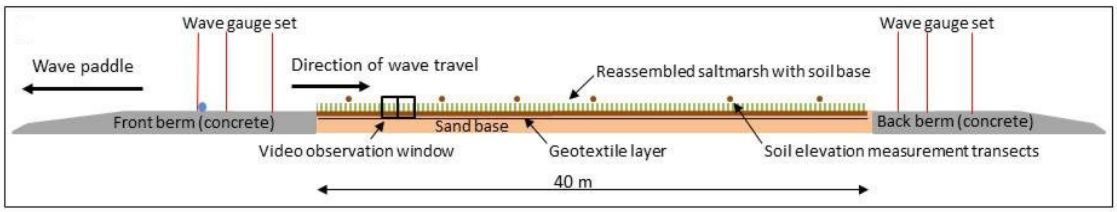

Figure 3.1 Upper panel: Experimental test-section in the Large Wave Flume (Grosser Wellenkanal, GWK) (from Möller et al., 2014). Lower panel: view of the vegetated test section at the mid-point in construction, looking towards the wave paddle (photo: I Möller)

The SWAN model was run in 1D mode with a JONSWAP spectrum waves, and one vegetation layer. The model input conditions were calibrated to produce the wave conditions at the initial wave gauge set. The model was run initially using the original SWAN-VEG module, with the drag coefficient having a fixed value for each test condition determined by Eq. 9. The value of U_m is defined at the front of the saltmarsh test section. The model was subsequently run using the new modified SWAN-VEG module where the C_D was calculated internally in the model using Eq. 9.

The measured and predicted normalised significant wave height reduction for the different wave conditions are presented in Figure 3. 2. The measured experimental values show the normalised significant wave height reduction is fairly constant over the different test conditions, with a value ≈ 0.25. The wave height reduction predicted by the original SWAN-VEG module, with a fixed C_D, underestimates the wave dissipation over all the test conditions. Whereas the new SWAN-VEG module, with varying C_D, slightly overestimates the wave dissipation. The new SWAN-VEG module gives a better fit to the experimental data, especially at high significant wave heights representing storm waves.

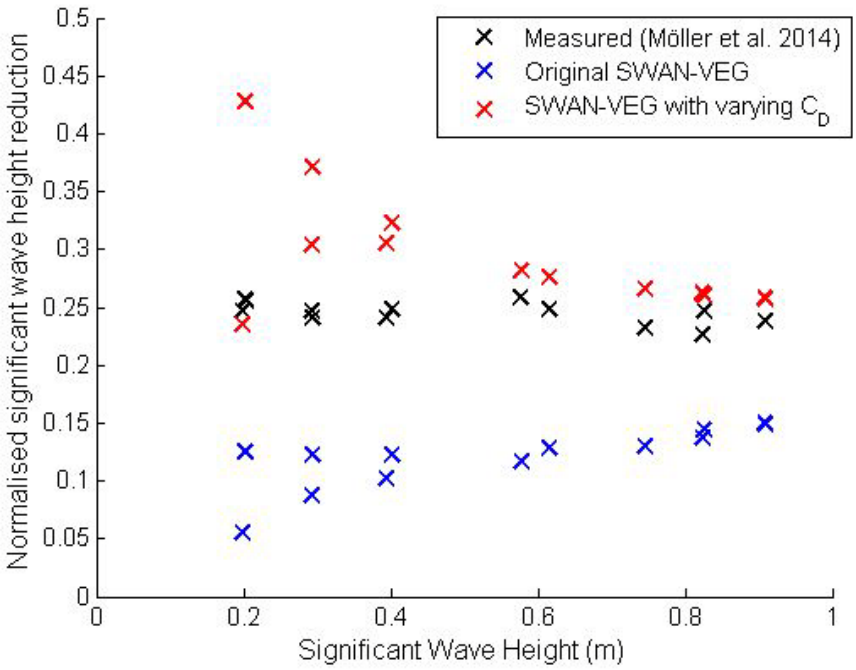

Figure 3.2 Normalised significant wave height reduction across a saltmarsh under storm conditions in a wave flume. Wave height measurements (Moller et al. 2014) are compared against predicted values using a SWAN model with a fixed and varying drag coefficient.

3.3.2 Validation of a wave dissipation due to vegetation along a salt marsh transect (large scale)

The modified SWAN-VEG module was then validated against the wave dissipation measurements of Moller et al. (1999), along a saltmarsh transect at Stiffkey, North Norfolk (Figure 3. 3). Moller et al. (1999) measured the wave conditions at the seaward margin of the saltmarsh (marked as "Middle station" in Figure 3.4) and at the end of a 197m (i.e. large scale of the wave energy dissipation hierarchy) saltmarsh transect (marked as the "Inner station"), which ran 44.5° from N. The experiment was carried out during September 1994 and May 1995. Along the transect the marsh consists of *Limonium vulgare*, *Aster tripolium*, *Atriplex portulacoides*, *Salicornia* spp. (several species) and *Spartina* spp. At the landward end the same species occur alongside *Suaeda maritima*, *Plantago maritima* and *Puccinella maritima*. The elevation varies over the transect with a slope of 0.00196.

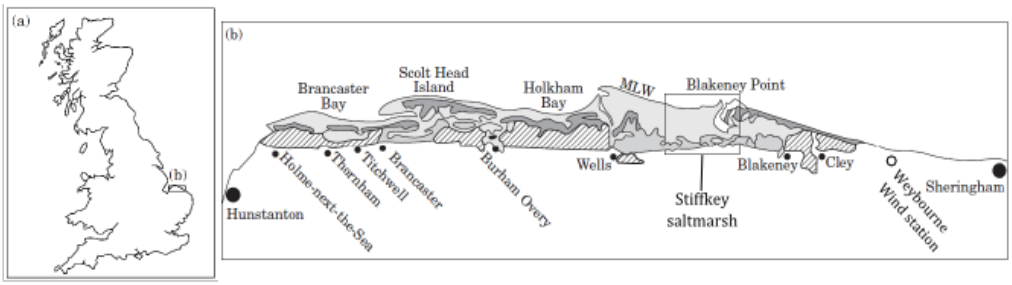

Figure 3.3 Location of the Stiffkey saltmarsh, North Norfolk (from Möller et al., 1999)

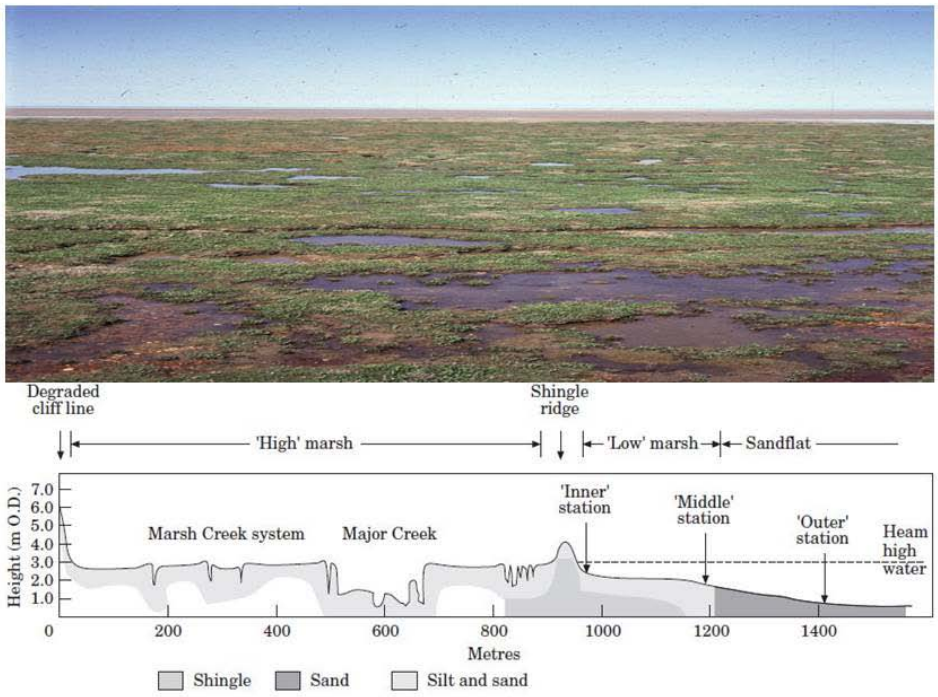

Figure 3.4 Upper panel; View of 'low' marsh, Stiffkey, North Norfolk, looking seawards (photo: T Spencer). Lower panel: section across Stiffkey marshes. Transect lies between 'inner' and 'middle' station on the 'low' marsh (from Möller et al. 1999)

Only the experimental data with onshore winds that run parallel to the transect are included in the validation here. It is assumed that when onshore wind directions deviate by less than ± 45° from the transect, the waves can be considered to be travelling along the line of the transect. The wind conditions were taken from the Weybourne meteorological station (Figure 3. 3), North Norfolk coast (16 km to the east of the study site) and were obtained from the BADC MIDAS wind database.

The vegetation characteristics required by the SWAN-VEG model were not all determined during the experiment. The vegetation height is derived from side-on photographs of the vegetation at Stiffkey (Moller et al. 1999), where H_v = 0.11m (Figure 3.5). The plant diameter is assumed to be D_v = 0.00125m, from the representative North West European saltmarsh used in Moller et al. (2014). The plant density is assumed to be similar to a saltmarsh transect at Tillingham, Essex (see section 3.3.3), N_v = 1061.

Figure 3.5 Black/white ground level, horizontal photograph of late summer (September) vegetation community structure on the 'low' marsh at Stiffkey, c. 100 m landward from the marsh edge (from Möller et al. 1999).

The modified SWAN-VEG model is run in 1D mode over 8 wave bursts with large waves, the test conditions are shown in Table 1.

Table 3.1 Test conditions for the large-scale wave energy dissipation modeling from wave conditions measured at the Middle Station on the saltmarsh transect at Stiffkey, North Norfolk (Figure 3.4; Moller et al., 1999).

Run	Water Depth (m)	Significant wave height (m)	Peak Period (s)	Mean wind direction (°)	Mean wind speed (ms^{-1})
1	0.77	0.29	6.83	60	15
2	0.76	0.28	5.39	60	15
3	0.74	0.27	1.86	60	15
4	0.96	0.3	2.73	90	14
5	0.98	0.45	2.73	80	22
6	1.19	0.52	4.18	70	25

The measured normalized significant wave height reduction is compared with the predicted wave height reduction by the modified SWAN-VEG module in Figure 3. 6. At the saltmarsh transect the measured wave height reduction between the 'Middle' and 'Inner' wave recording stations (Figure 3.4) decreases with increasing wave height. The SWAN-VEG estimates the same pattern as the experimental results. The predicted wave height reduction shows a very good agreement with the measured results, there is a slight overestimation of dissipation at observed conditions with small waves, which is consistent with the findings at the laboratory scale.

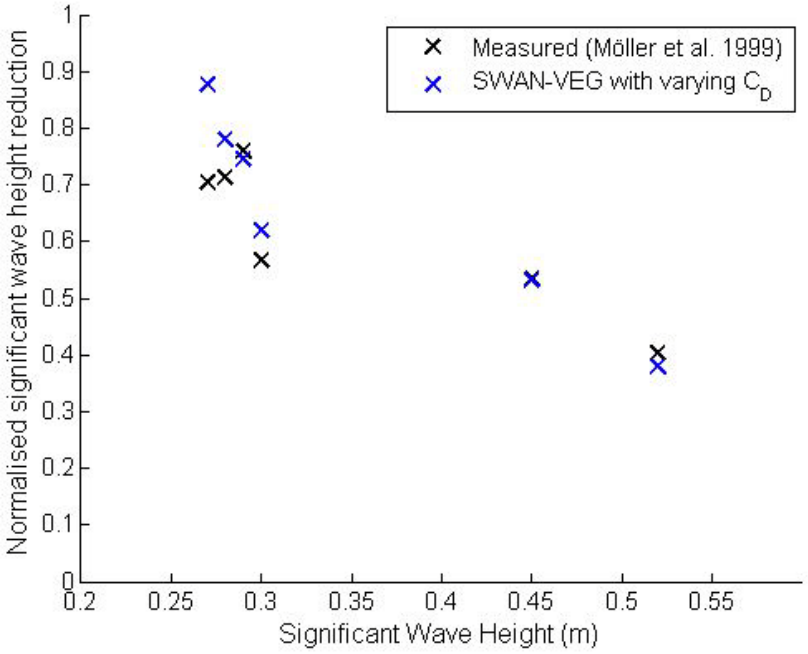

Figure 3.6 Normalized significant wave height reduction across a saltmarsh transect (Figure 3.4; 'Middle' to 'Inner' stations) with different wave conditions. Wave height measurements by Moller et al. (1999) are compared against predicted values from the adapted SWAN-VEG module

3.3.3 Validation of wave dissipation due to vegetation over three saltmarsh transects with different vegetation characteristics (small scale)

The new SWAN-VEG module is validated against the wave dissipation measurements of Moller (2006) at Tillingham, Essex coast, UK. Here, the SWAN-VEG module is used to predict wave dissipation using both a mean and a spatially varying vegetation height at the small scale (< 10 m).

Moller (2006) compared the wave dissipation over 3 short saltmarsh transects (length t1= 3.74m , t2 = 3.92m, t3=3.99m) with differing vegetation characteristics. The wave dissipation was measured at up to 6 different water depths (approx. 0.2m, 0. 3m, 0.4m, 0.5m, 0.6m, and 0.7m) on a rising tide. For the validation, the measured values over one tide during September 2004 are used (H_s = 0.05-0.16m, T_p =3.7-5.4s). The transects were located close to each other, and the same distance from the edge of the marsh so that wave conditions are similar across the transects. The three transects consist of the common saltmarsh species *Spartina* spp. and *Salicornia* spp. in differing proportions.

Stem heights and dry biomass were determined in the field study using side-on photographs (Möller, 2006). The mean stem height was taken for each transect. A spatially varying vegetation height over the short transects was extrapolated from the average of three side-on photographs which covered a distance of 0.5m, the spatially varying vegetation heights are presented in Figure 3. 7.

The vegetation diameter and number of plants per m² were not calculated by Moller (2006). For use in the SWAN model the mean vegetation diameter for *Salicornia* is taken as 3mm (mean diameter of 2-3mm, Kong and Zheng 2014; mean diameter of 2-4mm, Neumeier and Amos 2006). The mean diameter of *Spartina* is taken as 6.4mm (Anderson and Smith, 2014). The number of plants per m² is calculated from the dry biomass weight of the species from each transect. The dry biomass weight per stem for *Salicornia* is taken as 0.71g/plant (Kong and Zheng 2014), and 0.377g/plant for *Spartina* (mean value calculated from Alexander and Robinson 2006). The transect compositions and vegetation characteristics are given in Table 2.

Table 3.2 Measured and derived vegetation characteristics at three saltmarsh transects in Tillingham, Essex (Moller 2006)

Transect	Composition	Mean Vegetation Height (m)	Mean Vegetation Diameter (m)	Mean number of plants per m²
1	Spartina 86% Salicornia 11%	0.151	6.01×10^{-3}	1061
2	Spartina 73% Salicornia 25%	0.225	5.53×10^{-3}	1089
3	Salicornia 98%	0.059	3×10^{-3}	521

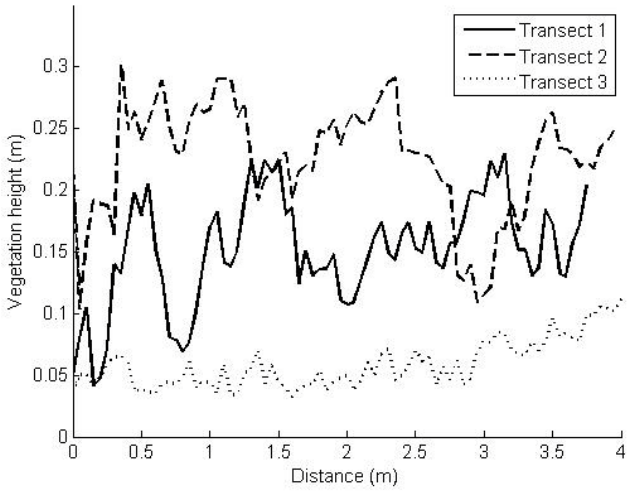

Figure 3.7 Spatially varying vegetation height over three saltmarsh transects in Tillingham, Essex.

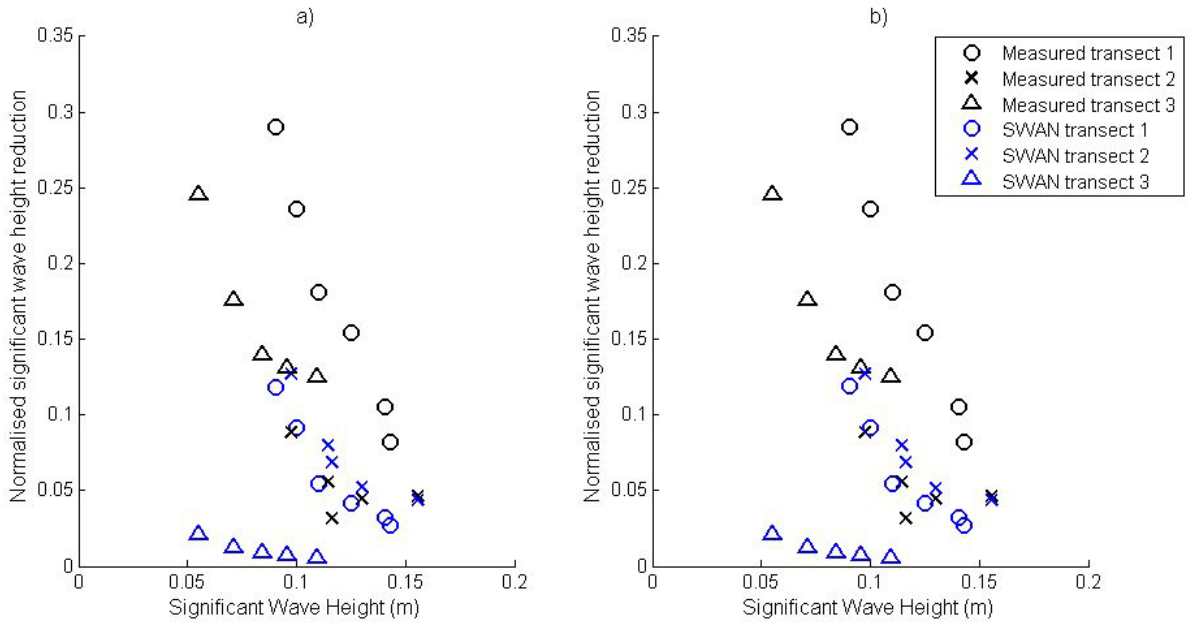

Figure 3.8 Normalised significant wave height reduction across three transects with differing vegetation characteristics. Measured wave height by Moller (2006) are compared against predicted values using the adapted SWAN-VEG module. a) fixed vegetation height in SWAN, b) spatially varying vegetation height in SWAN.

Figure 3.8 presents the measured wave height reduction over the three transects with the predicted wave dissipation by the SWAN model. Surprisingly, there is no difference between the SWAN results using a fixed vegetation height (Figure 3.8a) and a spatially varying vegetation height (Figure 3.8b). This could be due to the short transect length, and the fairly uniform plant height over it. The SWAN-VEG model shows good agreement with the measured dissipation over transect 2, but a large underestimation of wave dissipation over transects 1 and 3. This underestimation could be due to the short vegetation at transects 1 and 3. The drag coefficient formula (Eq. 9) used in the modified SWAN-VEG module is based on a saltmarsh with a mean height of 0.7m (Moller et al. 2014). The Mendez and Losada (2004) equation is also based on taller plants and is validated using experimental data of artificial kelp at a height of 0.2m (Dubi, 1995), and using kelp with a height of 1 and 3m (Løvås 2000). As the equations are based on vegetation with larger heights it may be necessary to use modified wave dissipation or drag coefficient formulae for short plants.

3.4 Findings and recommendations

The conceptual model suggests that wave energy dissipation across vegetated intertidal platforms, or saltmarshes, takes place across a nested hierarchy of scales, from the <10 m to >1,000 m. Here we breakdown those effects into three characteristics scales: small, intermediate and large scale. The modified SWAN-VEG module wave dissipation calculation has shown a good agreement with experimental data on saltmarsh vegetation from a wave flume under simulated storm surge conditions (Figure 3.2; intermediate scale) and when 'scaled up' for a typical NW European saltmarsh (Figure 3.6; large scale) . The new formulation has the advantage

that the vegetation part of the model does not need to be calibrated for each test condition or vegetation species. The new module can also be used for modeling situations over longer periods of time where the wave conditions are likely to vary significantly, such as during storms. This furthers the scope of the vegetation module for use in large scale and longer term storm surge modeling.

However, the 'scaling down' of the new model to investigate wave height reduction across three < 10 m long transects (i.e. short scale in the hierarchy of controls on energy dissipation) with differing vegetation characteristics was less successful. Whilst the new SWAN module predicted the wave dissipation well over the small scale transect with taller vegetation (>0.2m), it was not able to predict wave dissipation well over the shorter vegetation height. When scaling-down the vegetation characteristics by spatially varying the vegetation heightno differences in model outputs were seen when using a fixed vegetation height versus a spatially varying vegetation height. It is recommended that the drag coefficient formula is optimised for use with short plants; this may require an alternative formula. The impact of spatially varying vegetation characteristics should also be assessed further. The spatially varying vegetation is difficult to validate as there are limited studies which have measured the required vegetation characteristics, due to current labour intensive field sampling techniques. In addition, the vegetation characteristics could be further optimised by introducing a spatially varying vegetation diameter.

3.5 References:

Alexander, C. and Robinson, M. 2006. Quantifying the ecological significance of marsh shading: The impact of private recreational docks in coastal Georgia. *Coastal Resources Division, Georgia Department of Natural Resources, Brunswick, Georgia.*

Anderson, M. E. and Smith, J. M. 2014.Wave attenuation by flexible, idealized salt marsh vegetation. *Coastal Engineering,* 83, 82-92.

Augustin, L. N., Irish, J. L. and Lynett, P. 2009. Laboratory and numerical studies of wave damping by emergent and near-emergent wetland vegetation. *Coastal Engineering*, *56*(3), 332-340.

Booij, N., Ris, R. C. and Holthuijsen, L. H. 1999. A third-generation wave model for coastal regions: 1. Model description and validation. *Journal of Geophysical Research: Oceans, 104*(C4), 7649-7666.

Bouma, T. J., van Belzen, J., Balke, T., Zhu, Z. et al. 2014. Identifying knowledge gaps hampering application of intertidal habitats in coastal protection: Opportunities and steps to take. *Coastal Engineering*, *87*, 147-157.

Bradley, K. and Houser, C. 2009. Relative velocity of seagrass blades: Implications for wave attenuation in low-energy environments. *Journal of Geophysical Research: Earth Surface 114*(F1).

Dalrymple, R. A., Kirby, J. T. and Hwang, P. A. 1984. Wave diffraction due to areas of energy dissipation. *Journal of Waterway, Port, Coastal, and Ocean Engineering*, *110*(1), 67-79.

Dubi, A. M. 1995. Damping of water waves by submerged vegetation: A case study on *Laminaria hyperborean*. *Unpublished PhD Thesis, University of Trondheim.*

Jadhav, R. S., Chen, Q., and Smith, J. M. 2013. Spectral distribution of wave energy dissipation by salt marsh vegetation. *Coastal Engineering*, *77*, 99-107.

Kobayashi, N., Raichle, A. W. and Asano, T. 1993. Wave attenuation by vegetation. *Journal of waterway, port, coastal, and ocean engineering*, *119*(1), 30-48.

Kong, Y. and Zheng, Y. 2014. Hydroponic production of purslane as a sodium-removing vegetable in NaCl-rich nutrient solution. *HortScience*, *49*(2), 201-206.

Løvås, S.M. 2000. Hydro-physical conditions in kelp forests and the effect on wave damping and dune erosion: A case study on *Laminaria hyperborea*. *Unpublished PhD Thesis, Norwegian University of Science and Technology.*

Méndez, F. J., Losada, I. J. and Losada, M. A. 1999. Hydrodynamics induced by wind waves in a vegetation field. *Journal of Geophysical Research: Oceans*, *104*(C8), 18383-18396.

Mendez, F.J. and Losada, I.J. 2004. An empirical model to estimate the propagation of random breaking and nonbreaking waves over vegetation fields. *Coastal Engineering*, 51(2),103-118.

Möller, I. 2006. Quantifying saltmarsh vegetation and its effect on wave height dissipation: Results from a UK East coast saltmarsh. *Estuarine, Coastal and Shelf Science* 69.3, 337-351.

Möller, I., Spencer, T., French, J.R., Leggett, D.J., and Dixon, M. 1999. Wave transformation over salt marshes: A field and numerical modeling study from North Norfolk, England. *Estuarine, Coastal and Shelf Science* 49, 411-426.

Möller, I., Spencer, T., French, J.R., Leggett, D.J. and Dixon, M. 2001. The sea-defence value of salt marshes - a review in the light of field evidence from North Norfolk. Water and Environment Journal 15, 109–116.

Möller, I., Mantilla-Contreras, J., Spencer, T. and Hayes, A. 2011. Micro-tidal coastal reed beds: Hydro-morphological insights and observations on wave transformation from the southern Baltic Sea. Estuarine, Coastal and Shelf Science 92, 424-436

Möller, I., Kudella, M., Rupprecht, F., Spencer, T. et al. 2014. Wave attenuation over coastal salt marshes under storm surge conditions. Nature Geoscience, 7(10), 727-731.

Neumeier, U. R. S. and Amos, C.L. 2006. The influence of vegetation on turbulence and flow velocities in European salt-marshes. Sedimentology 53(2), 259-277.

Ozeren, Y., Wren, D. G., and Wu, W. 2013. Experimental investigation of wave attenuation through model and live vegetation. Journal of Waterway, Port, Coastal, and Ocean Engineering, 140(5).

Paul, M. and Amos, C. L. 2011. Spatial and seasonal variation in wave attenuation over Zostera noltii. Journal of Geophysical Research: Oceans, 116(C8).

Sánchez-González, J. F., Sánchez-Rojas, V. and Memos, C. D. 2011. Wave attenuation due to Posidonia oceanica meadows. Journal of Hydraulic Research, 49(4), 503-514.

Suzuki, T., Zijlema, M., Burger, B., Meijer, M. C. and Narayan, S. 2012. Wave dissipation by vegetation with layer schematization in SWAN. Coastal Engineering, 59(1), 64-71.

.

4 Description of the flash flood module FF-EWS

4.1 Introduction

The objective of this Chapter (see Section 1.3) is the development of a flash flood module. This module will build upon the experience and advances made in the IMPRINTS and DRIHM projects. The module will work in two modes: a few days in advance of an event and a few hours in advance. For the first time scale, the proposed strategy will be to incorporate the high resolution precipitation forecasts over the Tordera Delta and Bocca di Magra sites to compute the real-time accumulated forecasts of rainfall over the drainage basin. For the second time scale, rainfall forecasts based on radar networks will provide high-resolution estimates that can be transformed into high resolution flash flood warnings. A hydrological multi-model approach will be explored into high resolution flash flood warnings at any location in the drainage system through the use of 2D models

The flash flood module delivers hydrological warnings at any location in the drainage network discredited as a high-resolution 2D grid, and will enable the application of a hydrological multi-model approach. This will deliver a checked-in flash flood module whose products can be integrated in the FEWS platform with accompanying validation document and description.

This Chapter presents the improvements made to the flash flood modules developed in the IMPRINTS project (sections 4.2-4.5) and illustrates how it has been implemented in the Tordera Delta case study site in the frame work of RISC-KIT project (section 4.6). One of the main objectives of this demonstration is the analysis of the multi-model approach, comparing the FF-EWS module (that will be implemented in the case study site of Bocca di Magra in WP5) with the hydrological tools developed as part of the DRIHM project for the same site) and Section 4.7 describes the steps needed for the implementation of this module with the system developed in the DRIHM project.

Finally, section 4.8 provides a description of how the outputs of the developed module will be integrated in the FEWS platform.

4.2 FF-EWS

Flash floods in coastal areas are controlled by two main variables: heavy rains and short response times (of the order of 0.5-6 hours). The short response times of coastal basins affected by flash floods are usually the consequence of the combination of three ingredients (e.g. Sempere-Torres, 2001; Gaume et al., 2009): small catchment areas (typically 5-100 km^2), steep terrain, and strong urbanization degree (the latter reduces the capacity of infiltration and promotes the fast propagation of the flood wave). On the other hand, in these steep, mountainous coastal basins, the terrain frequently promotes the convection of warm wet air from the sea, resulting in

enhanced precipitation from convective storms and mesoscale convective systems (MCSs) with high spatio-temporal variability.

The FP7 project IMPRINTS (FP7-ENV-2008-1-226555; Sempere-Torres et al., 2010) developed a module for hydrological hazard assessment (named FF-EWS for "Flash Flood Early Warning System"; Corral et al., 2009; Alfieri et al., 2010; Alfieri and Thielen, 2011; Berenguer and Sempere-Torres, 2015). This FF-EWS module is based on the assumption that the rainfall accumulated upstream of a point of the drainage network can be used to characterize the flash flood hazard [specially for high return periods, for which the response of the catchment is mainly controlled by the amounts of rain, and the probability distribution function (pdf) of the discharges tends to have the same slope as the pdf of precipitation –Guillot and Duband, 1967].

Within the IMPRINTS project, this module was implemented in two different configurations (see, e.g., Versini et al. 2014): (1) based on the 16-member COSMO Limited-Area Ensemble Prediction System (COSMO-LEPS), ran over a 7-km grid with 3-hour accumulations, to characterize the flash flood hazard level at 1 km and for forecasting times up to 24 hours at European scale (this product is currently integrated as part of the operational European Flood Awareness System, EFAS, www.efas.eu); and (2) a local high-resolution very-short-term configuration, based on radar-based Quantitative Precipitation Estimates and Forecasts (QPE and QPF) with a resolution of 1 km and 10 minutes, and forecasting times up to 3 hours.

The objective of the work presented here is the implementation of an improved version of the FF-EWS based on radar-based Quantitative Precipitation Estimates (QPE) to assess the flash flood hazard in the coastal area around the Tordera Delta (RISC-KIT case study site; see Figure **1.2**). The improvements made to the system are: (1) increased resolution (FF-EWS has now been implemented at 200 m), and (2) better estimation of the hazard level (expressed in terms of the return period), based on the construction of a 70-year climatology of daily rainfall maps (as described in Section 4.5).

The newly-developed FF-EWS module uses 1-km radar-based QPE and QPF 30-minute accumulations (updated every 10 minutes). This resolution is very well adapted to flash flood monitoring, frequently triggered by rainfall extremes (for example due to stationary convective thunderstorms) at scales that are generally not well resolved by numerical weather prediction (NWP) models or low-resolution rain gauge networks [see, e.g., Alfieri et al. (2012) for a review of the benefits and limitations of the different rainfall inputs used for hazard assessment].

For each point of the drainage network, the rainfall inputs (rainfall observations and forecasts) available at a given time are used to compute the rainfall accumulation aggregated over the upstream basin (hereafter, referred to as the basin-aggregated rainfall) over a duration corresponding to the concentration time of the catchment. The computations are made for durations between 0.5 and 24 h, for catchments between 5 and 5000 km^2.

Hazard assessment (expressed in terms of probability of exceedance, or as return period) is based on comparing the basin-aggregated rainfall accumulations with the values of the available Intensity-Duration-Frequency (IDF) curves for a duration equal

to the characteristic concentration time of the catchment. Every time a new QPE field is available (see section 4.3.1), a series of rainfall forecasts is computed (with the forecasting systems presented in section 4.3.2), and hazard assessment is performed (section 4.5) with a resolution of 200 x 200 m^2 and for forecasting times between t+0 and t+3 hours (with the nowcasting system) or up to a few days (using NWP precipitation forecasts).

4.3 Rainfall estimation and forecasting

The system relies on the Quantitative Precipitation Estimates and Forecasts (QPE and QPF) produced with the Integrated Tool for Hydrometeorological Forecasting (EHIMI, Corral et al., 2009) based on weather radar observations.

4.3.1 Rainfall estimation

Ensuring the quality of radar QPE is fundamental to guarantee the good performance of the system. This requires processing radar observations with a chain of algorithms to reduce the effect of the sources of error affecting radar QPE (e.g., Germann et al., 2006; Corral et al., 2009; Villarini et al., 2009).

In EHIMI the production of QPE maps includes a chain of algorithms to (1) mitigate the effects of the interception of the radar beam with the terrain (Delrieu et al., 1995), (2) eliminate non-meteorological echoes (Sánchez-Diezma et al., 2001; Berenguer et al., 2006), (3) identify precipitation types in volumetric radar data, (4) extrapolate elevated radar observations to the surface with a Vertical Profile of Reflectivity that depends on the type of precipitation (as described by Franco et al., 2006; 2008), and (5) convert reflectivity into rain rate using a relationship also adapted to the type of precipitation. From instantaneous rainfall fields, rainfall accumulations are computed with a resolution of 1x1 km^2 considering the motion of precipitation systems and the evolution of rainfall intensities between consecutive radar scans (Fabry et al., 1994; Berenguer et al., 2005).

4.3.2 Rainfall forecasts

As mentioned above, the FF-EWS module works at two different time horizons (either separately or combinedly), depending on the rainfall inputs used to forecast rainfall:

a) A few hours ahead (nowcasting)

Rainfall nowcasting by Lagrangian extrapolation (i.e., advection of most recently observed rainfall field with the estimated motion field, neglecting the evolution of rainfall intensities) has proven to generate useful rainfall forecasts for lead times up to a few hours (see e.g., Germann and Zawadzki, 2006; Berenguer et al., 2012). The version of this algorithm used here (Berenguer et al., 2011) is composed of two modules for:

- Rainfall tracking: The algorithm implemented to estimate the motion field of precipitation is based on matching three rainfall fields within 24 minutes with a modified version of the COTREC algorithm (Li et al., 1995).
- Extrapolation of rainfall observations: The last observed rainfall field is advected in time according to the motion field estimated with the mentioned

tracking technique. The motion field is kept stationary in time along the series of generated forecasts.

b) A few days ahead (NWP)

At these time horizons, flash flood hazard assessment is based on rainfall obtained with a mesoscale NWP model. Typically, the grid size of these models is of the order of a few km (e.g. as mentioned above, the flash flood module implemented in EFAS is based on COSMO-LEPS, which is run over a 7-km grid). However, the effective resolution of NWP precipitation forecasts is known to be significantly coarser, and it is recommended to downscale them to scales closer to the resolution of the grid used for flash flood hazard assessment (e.g. Rebora et al., 2006; Silvestro et al., 2014).

4.4 Retrieval of the drainage network

The drainage network has been retrieved from the 200-m Digital Elevation Model (DEM) produced by the Cartographic and Geological Institute of Catalonia (www.icgc.cat) using the D8 algorithm (O'Callaghan and Mark, 1984). This is the simplest method for extracting drainage directions in grid-based DEMs from each cell to one of its eight neighbors to the direction with the steepest downward slope.

The drainage network is extracted with a resolution of 200 m. Figure **4.1** shows the resulting drainage network in the RISC-KIT domain in the domain considered in the RISC-KIT case study site around the Tordera Delta on the Catalan coast. The chosen area includes the Tordera catchment (865 km^2) and the coastal basins (from south to north, Riera de Calella, Riera de Pineda, Riera de Santa Susanna, Riera de Palafolls, Torrent de la Burgada, Torrent de can Rabasa, Riera de Passapera and Riera de Lloret).

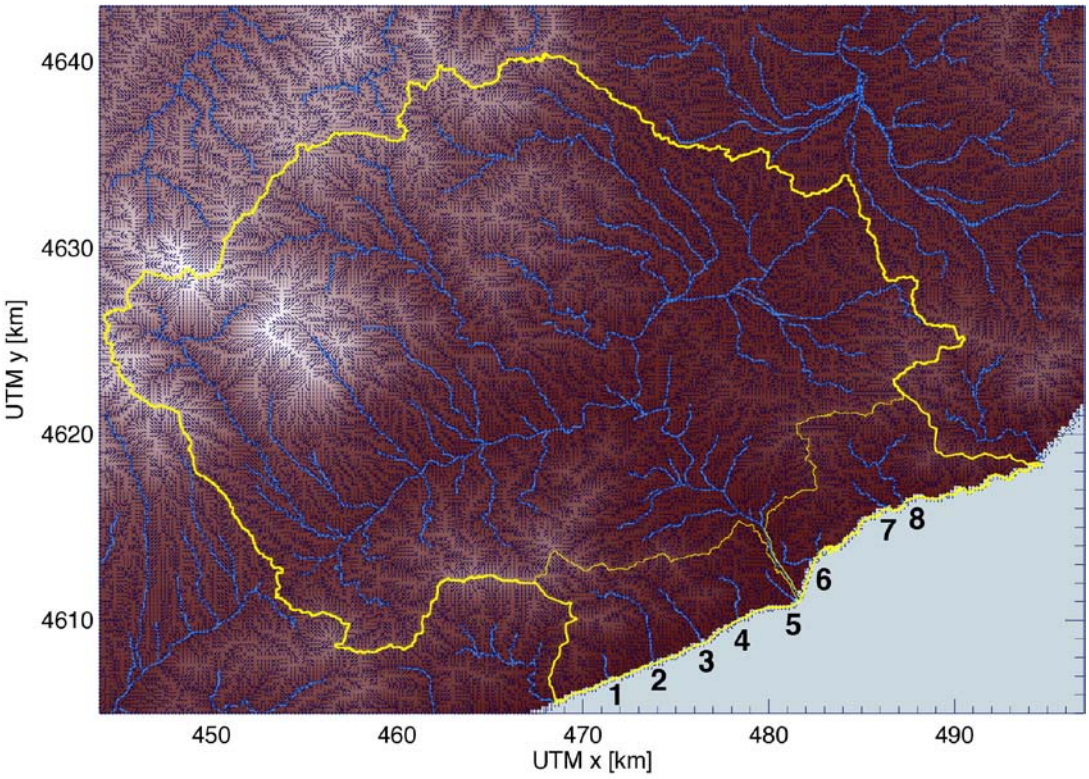

Figure 4.1 Area where the FF-EWS module has been implemented. The small dark blue arrows indicate the retrieved drainage network. The thin yellow contour indicates the limits of the Tordera catchment (865 km²). The coastal streams correspond to Riera de Calella, Riera de Pineda, Riera de Santa Susanna, Riera de Palafolls, Torrent de la Burgada, Torrent de can Rabasa, Riera de Passapera and Riera de Lloret (1-8).

4.5 Flash flood hazard assessment

As mentioned in section 4.2, flash flood hazard assessment is performed by estimating the return period of the rainfall aggregated over the catchment upstream of each grid point (basin-aggregated rainfall) and accumulated over the characteristic response time of the catchment.

Unlike IDF curves for point rainfall, which are available in many countries in Europe, information about the probability of exceeding basin-aggregated rainfall (the variable used for flash flood hazard assessment) does not exist in most of the cases. In the previous version of the FF-EWS module, this challenge was overcome by scaling the IDF values for point rainfall with a factor decreasing as the area of the catchment increases (e.g. Corral et al., 2009; Alfieri et al., 2011):

$$k_a = 1 - \frac{\log(A\,[km^2])}{15} \tag{4.1}$$

for catchment areas (A) larger than 1km².

Alternatively, in the framework of RISC-KIT, the probability of occurrence of basin-aggregated rainfall has been estimated from an improved climatology of precipitation maps obtained by interpolating point rainfall observations (from rain gauge historical records) with a new method focusing on the accurate representation of the spatial variability of the rainfall field. These rainfall maps have then been aggregated according to the drainage network to produce a climatology of basin-aggregated rainfall maps, which is the dataset used to estimate the probability of exceedance of a given value of the basin-aggregated rainfall at any point of the drainage network.

In many countries in Europe, rain gauge observation records are available at least since the first half of the 20th century. A large majority of these historical records are manual observations of daily-accumulated rain (historical observations over shorter durations –e.g. hourly data- are only available in very few number of points). Because of this, the construction of a climatology of rainfall maps based on the interpolation of historical rainfall records is typically based on daily rain gauge records. The method developed here aims at reconstructing the daily precipitation field from historical rain gauge observations while respecting the spatial structure of the rainfall field (section 4.5.1). Finally, daily rainfall values have been be disaggregated for shorter durations with a synthetic IDF function (as detailed in section 4.5.2).

4.5.1 Constructing a climatology of aggregated daily rainfall accumulations for FF hazard assessment.

A fundamental objective of the developed interpolation method is to respect the spatial structure of the rainfall fields. This is a requirement to guarantee the

hydrological representativeness of the basin-aggregated rainfall values at each grid point. With this aim, we have, first, analyzed the radar-based daily QPE fields available at regional scale around the Tordera Delta case study site (in Catalonia, NE of Spain) to infer the most descriptive spatial structure functions for the region, and these have then been combined to reconstruct the historical rainfall fields conditioned by the historical rain gauge observations.

a) Characterization of precipitation patterns in the area of study

One of the advantages of radar-based QPE maps is that, unlike the observations of rain gauge networks, they provide an accurate description of the spatial structure of the rainfall field with high resolution (of the order of 1 km) over large domains.

The method proposed here takes over this advantage by analyzing the radar-based 24-hour accumulations in Catalonia from March 2008 to February 2013. The precipitation product used for this analysis is the blended radar-rain gauge rainfall map, obtained with the method proposed by Velasco-Forero et al. (2009). This product benefits from the description of the structure of the precipitation field provided by with radar QPE while preserving the observed rain gauge accumulations.

These daily rainfall accumulations have been analyzed by means of Principal Component Analysis (PCA), to extract the most relevant precipitation patterns in the analysis domain. The advantage of PCA is that it obtains a basis of vectors under the constraint that each of them accounts for as much of the variability in the data as possible and is orthogonal to the preceding components.

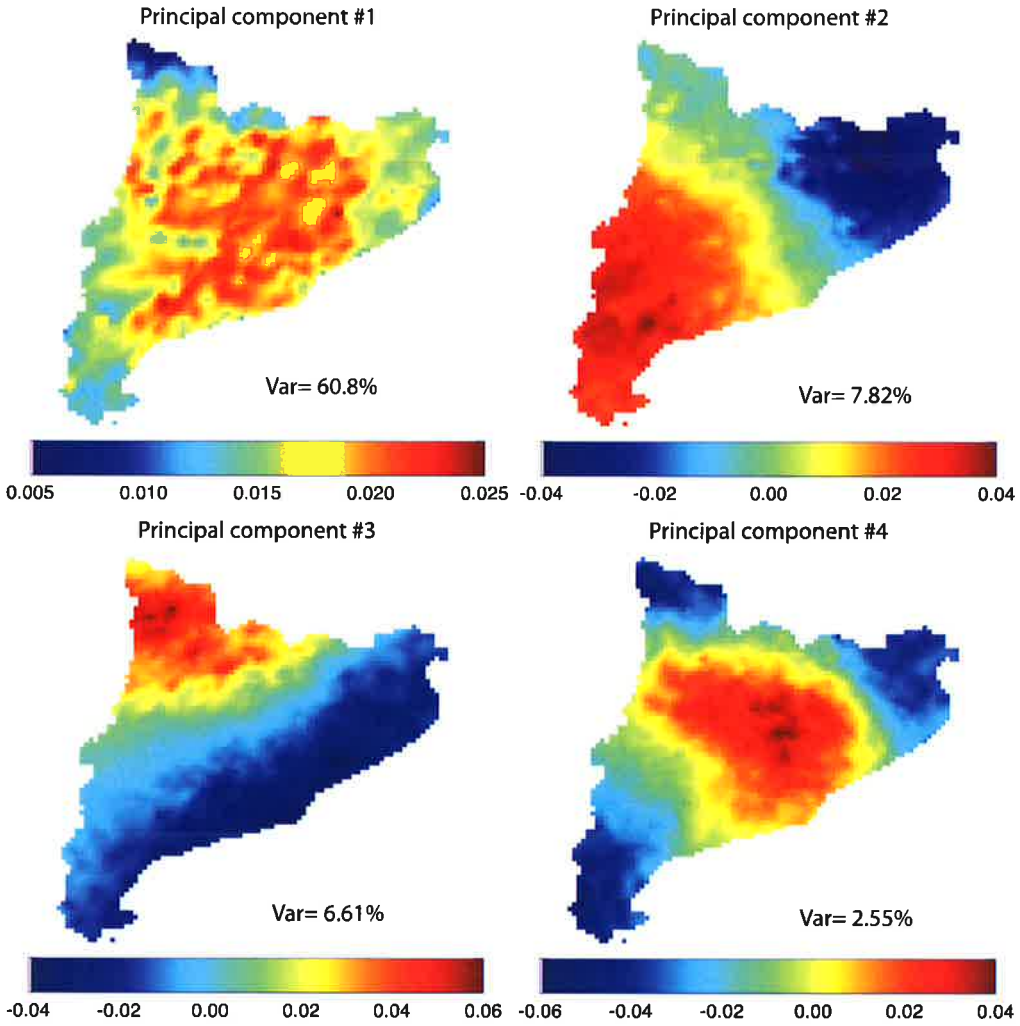

Figure 4.2 First four principal components of the daily rainfall accumulations estimated over the analysis domain (normalized eigenvectors of the covariance matrix; arbitrary units). The explained variance is indicated in each panel.

To reduce the skewness of daily rainfall accumulations, we have chosen to work with centered squared-root-transformed data,

$$\mathbf{x}_n = \sqrt{\mathbf{R}_n} - \frac{1}{N}\sum_i \sqrt{\mathbf{R}_i} \tag{4.2}$$

where $\mathbf{R}_n$ is the column vector of M grid point values of observed rain corresponding to day n and N is the total number of days.

PCA is carried out by diagonalizing the covariance matrix,

$$\mathbf{S}_x = \frac{1}{N-1}\sum_n \mathbf{x}_n \mathbf{x}_n^{\mathsf{T}} \tag{4.3}$$

Figure **4.2** shows the first 4 principal components obtained from the 5 years of $\mathbf{x}_n$. The first principal component explains 60.8% of the total variability and describes a rather

northeast and southeast-northwest (coast-mountain) gradients, and the fourth principal component represents precipitation variability in the central part of the domain. Figure **4.3** shows the dependence of the explained variance as a function of the number of principal components. It can be seen, for instance, that the first 25 principal components explain 90% of the variability of the analyzed daily rainfall accumulations.

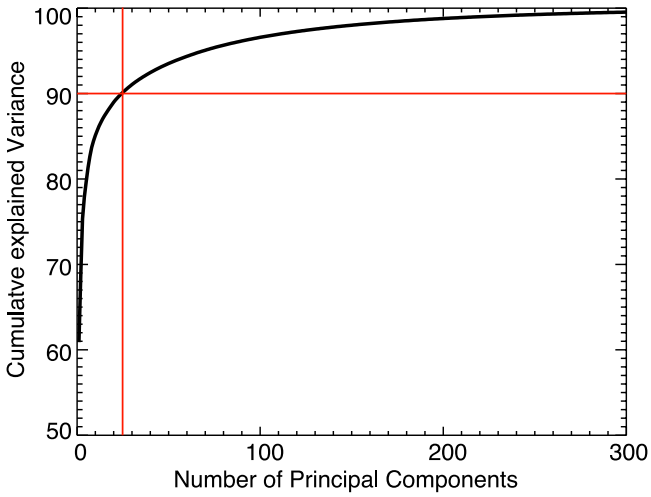

Figure 4.3 Cumulative explained variance as function of the number of principal components. The red lines indicate the number of components (25) needed to explain a variance of 90%.

Since the M eigenvectors of $\mathbf{S}_x$ (the principal components) form an orthogonal basis, any the precipitation field for a given day (x_n) can be fully reconstructed by linear combination of these eigenvectors. Similarly, x_n can be approximated by the first L principal components:

$$\mathbf{x}_n = \mathbf{E}a_n + \epsilon_n = \mathbf{x}_n^f + \epsilon_n \qquad (4.4)$$

where $\mathbf{E}$ is an (M x L) matrix, whose L columns are the first L eigenvectors of $\mathbf{S}_x$, and a_n is the (L x 1) column vector with the coefficients for these principal components. ε_n is the error due to the truncation (the fact that only the first L principal components are used), and x_n^f are the filtered observations of day n (i.e. neglecting the contribution of the principal components *L+1* to *M*). An example of the effect of this filtering is shown in Figure **4.4** for different values of L.

The first 25 principal components (which explain 90% of the variability of the daily accumulation dataset; red lines in Figure **4.3**) have been used to interpolate the historical rain gauge records (as described in section 4.5.1c).

b) Historical evolution of the rain gauge network

Figure **4.5** shows the evolution of the density of the rain gauge networks in Catalonia (operated by different meteorological and water authorities): in the 1940s, there were 58 rain gauges (one per 552 km^2), and the density increased up to 243 rain gauges in the early 2000s (one per 132 km^2). These historical records have been quality-controlled by means of double-mass analysis (Wilson, 1990) and the outliers have been rejected.

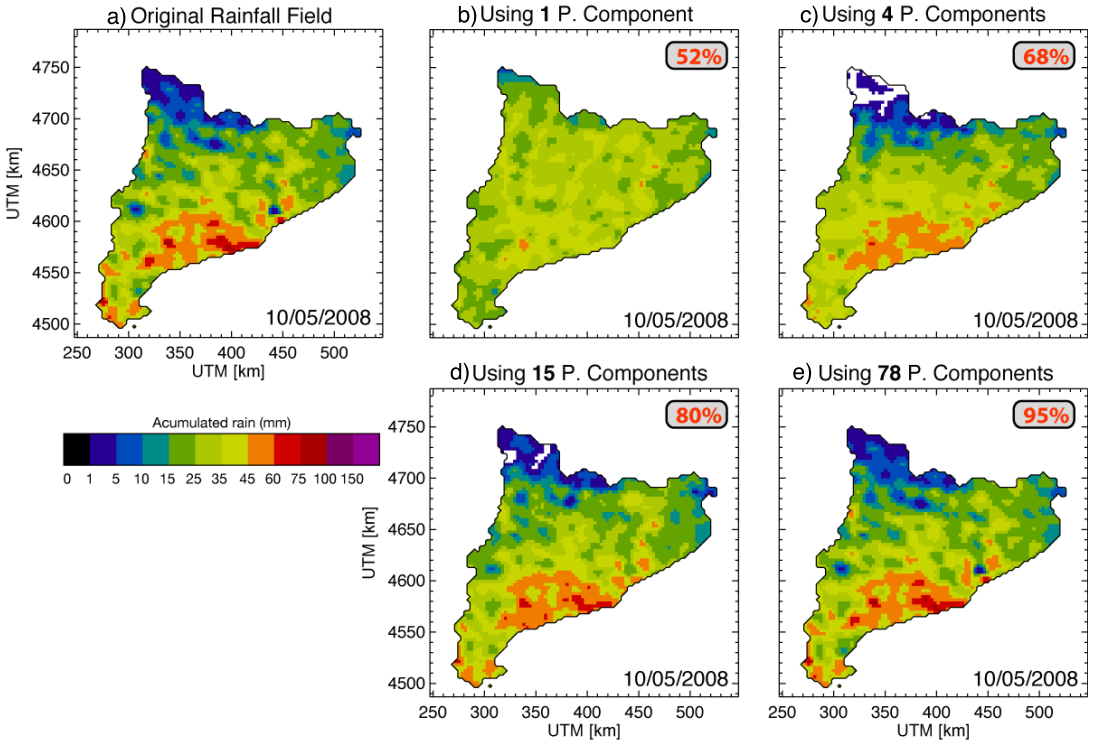

Figure 4.4 Description of a given rainfall field (daily accumulation for 10 May 2008) as a function of the number of principal components used in equation (4.4). (a) Estimated daily accumulation; (b-e) Filtered field for values of L=1, 4, 15, 78, respectively. The number on the upper right corner of panels b-e indicates the explained variance of the original rainfall accumulation.

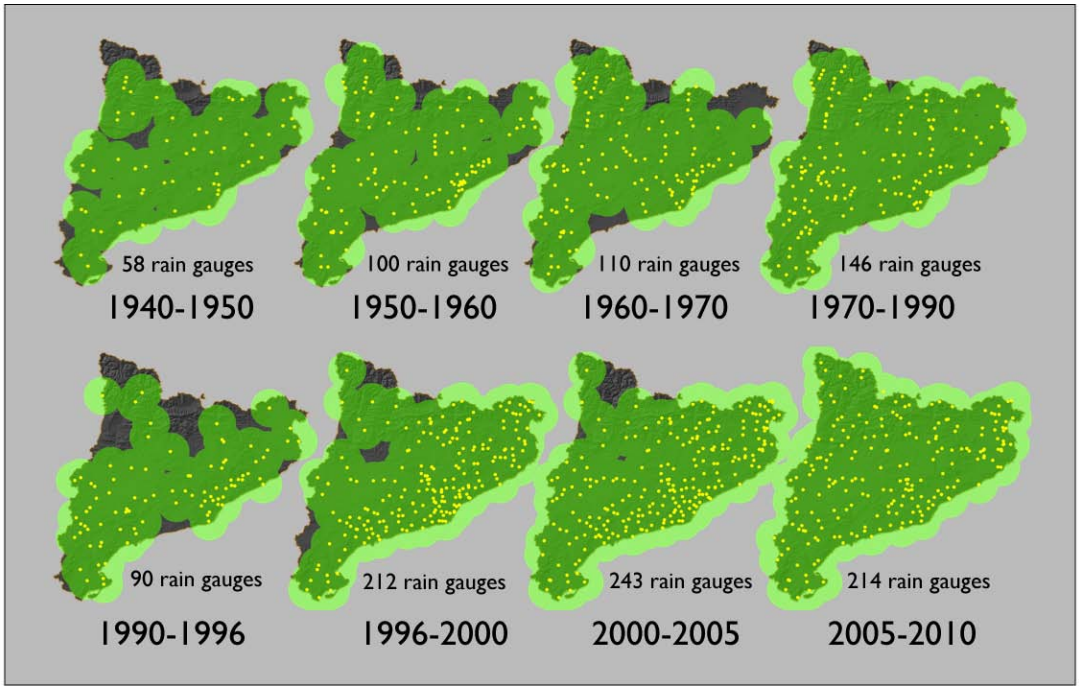

Figure 4.5 Historical evolution (1940-2010) of the rain gauge network used for the reconstruction of an improved climatology of daily rainfall accumulations in the area of study.

c) Reconstruction of daily rainfall accumulations

The objective of the developed method is to reconstruct the historical daily accumulation fields by combining the first 25 principal components retrieved from the daily radar-rain gauge blended maps (available in the period March 2008 – February 2013) given the historical daily rain gauge records. The final goal of this approach is to reconstruct the historical rainfall maps while preserving the spatial variability of the fields (i.e. avoiding the smooth accumulation fields obtained with traditional interpolation methods).

According to equation (4.4), the precipitation field can be approximated by linear combination of the first L principal components with the coefficients a_n. Consequently, to reconstruct the historical daily accumulation maps for a given day n, we need to estimate the column vector a_n for the first L (=25) principal components most compatible with the rainfall accumulation measured at the location of the available k rain gauges. This can be done by finding those coefficients a_n that result in optimal reconstruction of the values observed at rain gauge locations for day n, $\mathbf{x}_{\mathbf{g}n}$, which can be written as a version of equation (4.4) limited to rain gauge locations,

$$\mathbf{x}_{\mathbf{g}_n} = \mathbf{E}_{\mathbf{g}} a_n + \epsilon_{\mathbf{g}_n} \tag{4.5}$$

where $\mathbf{E}_{\mathbf{g}}$ is a matrix with the values of $\mathbf{E}$ at rain gauge locations, and $\boldsymbol{\varepsilon}_{\mathbf{g}n}$ is the error made at rain gauge locations. This is a linear system of k equations (as many as rain gauges) and L unknowns (the coefficients a_n). In general, the number of rain gauges is larger than the number of selected CP (k>L) and, thus, the system is over-determined. To solve it, we have used a Singular Value Decomposition (SVD) method to estimate the pseudo-inverse of $\mathbf{E}_{\mathbf{g}}$.

The result is the column vector a_n, with the coefficients necessary to combine the first L(=25) principal components of the precipitation field, which allows us to reconstruct the daily accumulation of day n given the k historical rain gauge observations for that day.

It has to be noted that, since equation (4.5) is an over-determined linear equation system, the solution is found in a root-mean-squared-error sense and, consequently, the retrieved rainfall map does not perfectly respect the observed rainfall accumulations at rain gauge locations. To prevent this, a final step has been applied consisting in applying the blending method of Velasco-Forero (2009), which imposes the values of rain gauge observations while respecting the structure of the reconstructed precipitation field.

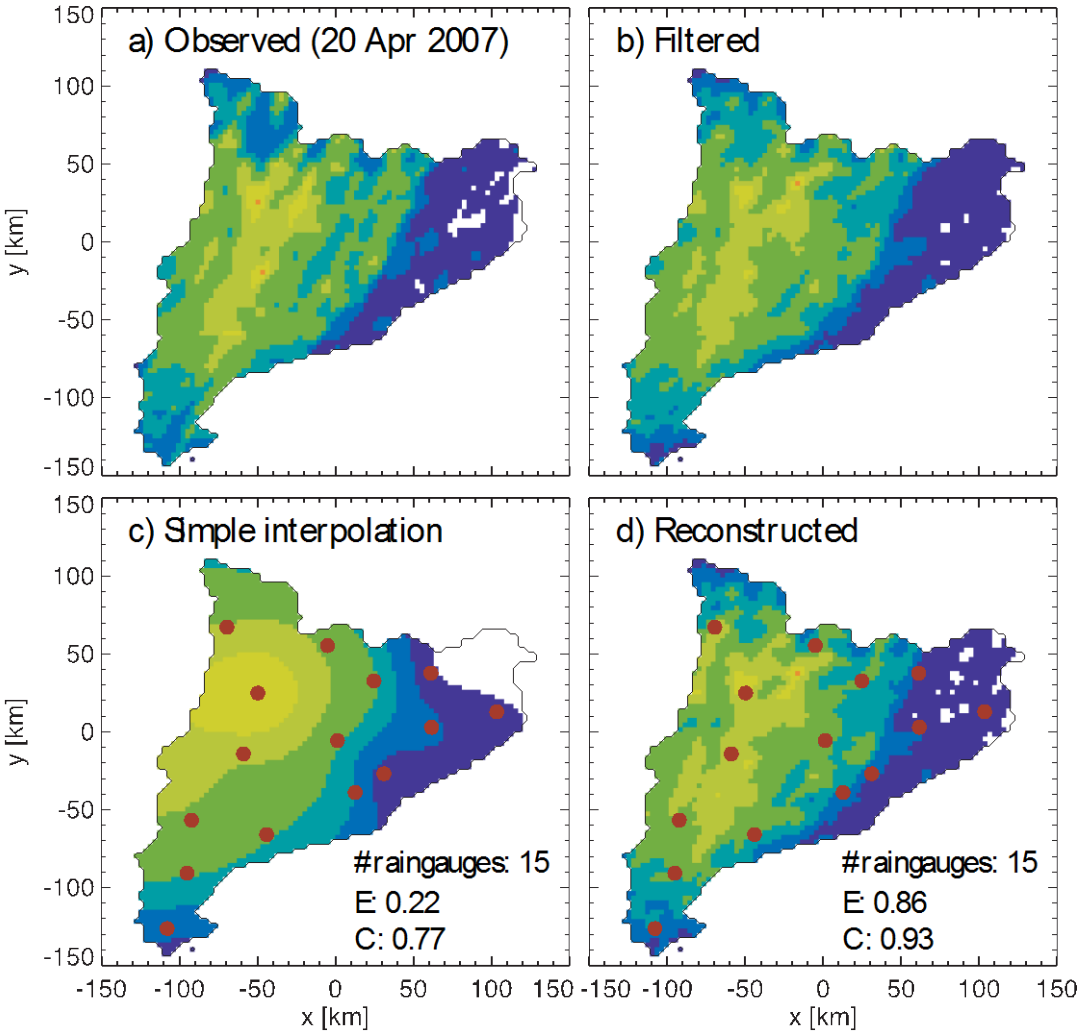

Figure 4.6 Illustration of the reconstruction method for the rainfall accumulation of 20 April 2007. (a) Reference field obtained with the radar-rain gauge blending method of Velasco-Forero et al. (2009), which is used as reference. (b) Rainfall field obtained using the first L=25 principal components in equation (4.4). (c) Field obtained using thin-plate splines to interpolate the (k=15) observations in the locations indicated with the red dots. (d) Same as (c), but with the proposed reconstruction method. In the bottom right corner of panels (c) and (d), E and C indicate the values of Nash efficiency and correlation obtained from the point-to-point comparison with the reference field of panel (a).

Figure **4.6** shows an example of implementation of the method described above, based on a case for which the blended radar-rain gauge product was available. For comparison, Figure **4.6**c shows the reconstruction of the rainfall accumulation map obtained with thin-plate spline interpolation (e.g. Duchon, 1977). Comparison between Figures **4.6**c and **4.6**d shows how the proposed method is able to reproduce the spatial structure of the rainfall field much more satisfactorily than the thin-plate-spline technique, which produces a very smooth field. For this particular case, this is also revealed by the high values of Nash Efficiency and correlation obtained from the comparison of the reconstructed field with the QPE accumulation of Figure **4.6**a.

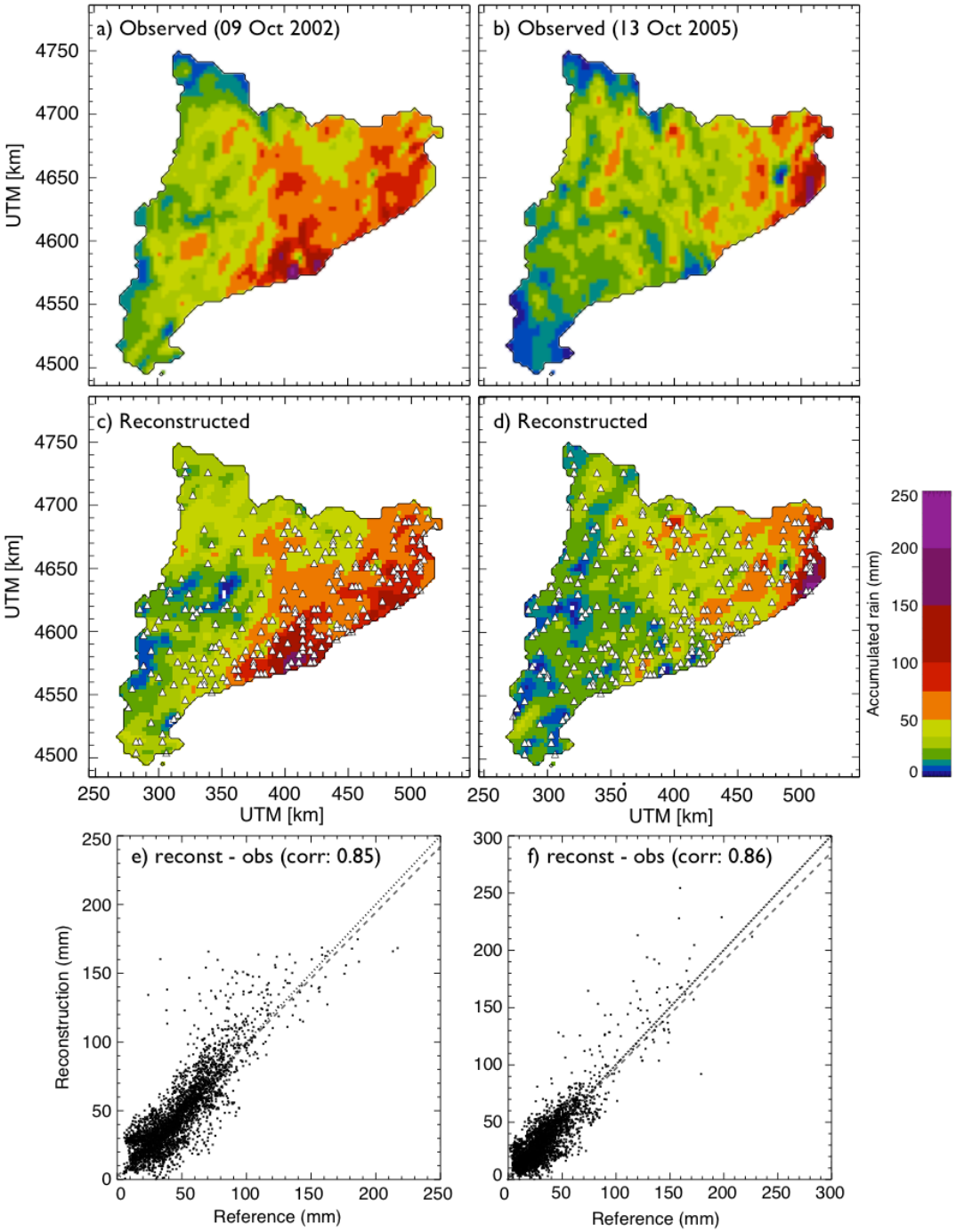

Figure 4.7 Example of the reconstruction of the daily accumulations for the flash-flood-producing precipitation events of 09 October 2002 (left) and 13 October 2005(right). Upper row: Reference daily accumulation obtained with the radar-rain gauge blending method of Velasco-Forero et al. (2009). Middle row: fields reconstructed with the proposed method (the white triangles indicate the locations of the available rain gauges). Bottom row: Scatter plots between the values of the reconstructed and the reference fields.

Similarly, Figure **4.7** shows an example of the reconstruction using the real rain gauge network for two different cases that produced flash floods in the Catalan coast (with

large areas where daily accumulations exceeded 100 mm). Also for these two cases, the spatial variability of the observed rainfall accumulations (Figs. **4.7**a and **4.7**b) is very well captured by the reconstructed fields (respectively, Figs. **4.7**c and **4.7**d), resulting in correlations of the order of 0.85 (Figs. **4.7**e and **4.7**f).

The method has been applied to the historical daily rain gauge records for the period 1940-2010 to reconstruct the daily accumulation maps for this period over Catalonia. These daily rainfall accumulations have been aggregated according to the drainage network in the area of study (the coastal area around the Tordera Delta case study site) to produce a climatology of basin-aggregated daily accumulations at each point of the drainage network. From this information we have performed an annual maximum analysis at each point of the drainage network to characterize the probability of exceedance (or return period) associated to a certain value of the variable basin-aggregated accumulation at each point.

4.5.2 Disaggregation of daily values

As explained in Section 4.2, the variable used for flash flood hazard assessment at a given point of the drainage network is the observed basin-aggregated rainfall integrated over the characteristic concentration time of the drained basin.

Consequently, to estimate the probability of exceedance for the observed accumulations, it is necessary to downscale the Intensity-Frequency curves for basin-aggregated daily accumulations (obtained as described in section 4.5.1c) to shorter durations. Due to the lack of historical rainfall observations for shorter durations, we have downscaled the daily values with the IDF curves used for structural design in Spain (see ACA, 2003):

$$I_D = I_d \cdot F^{\left(\frac{28^{0.1} - D^{0.1}}{28^{0.1} - 1}\right)} \tag{4.6}$$

where I_D (mmh^{-1}) is the mean basin-aggregated rainfall intensity for a duration D, I_d (mmh^{-1}) is the mean daily basin-aggregated rainfall intensity, and F is a regional factor that, for the area of study, takes a value of F=11.

4.5.3 Flash flood hazard assessment

Finally, the flash flood hazard estimated with the FF-EWS module is expressed in terms of the probability of exceedance estimated for the observed basin-aggregated rainfall integrated over the characteristic concentration time of the drained basin.

Section 4.6 demonstrates the performance of the system for two different cases that resulted in flash floods in the area of the Tordera Delta case study site.

4.6 Examples in the Tordera Delta case study site

This section presents the results of the FF-EWS module implemented in the Tordera Delta case study site (see Fig. **4.1**) for two intense rainfall events that produced significant damages in some areas of the case study site.

Radar rainfall estimates were produced with a resolution of 1 km and 10 minutes with the Integrated Tool for Hydrometeorological Forecasting (see section 4.3.1) using the observations of the CDV radar (which is part of the radar network of the Catalan Meteorological Service). Fig. **4.8** shows the rainfall accumulations for the two analyzed

events and the comparison between radar QPE accumulations and the observations of collocated rain gauges. Rainfall forecasts used in these examples were generated with the nowcasting module described in section 4.3.2a, and for forecasting times up to 3 hours.

During the first case (23-24 September 2010) a number of very small scale convective cells developed over the sea and the coastal area starting in the morning of 23 September and organizing into mesoscale convective systems in different areas of the radar domain (those showing the largest accumulations in Fig. **4.8**a) during the day until 02:00 UTC. After this, widespread precipitation affected the east part of the radar domain until 24 September around 07:00. Later, from 12:00 UTC, new convective cells developed in the coastal area, affecting the Tordera Delta case study site (black rectangle in Fig. **4.8**a) from 14:00 to 18:00 UTC and producing the largest rainfall amounts in this area.

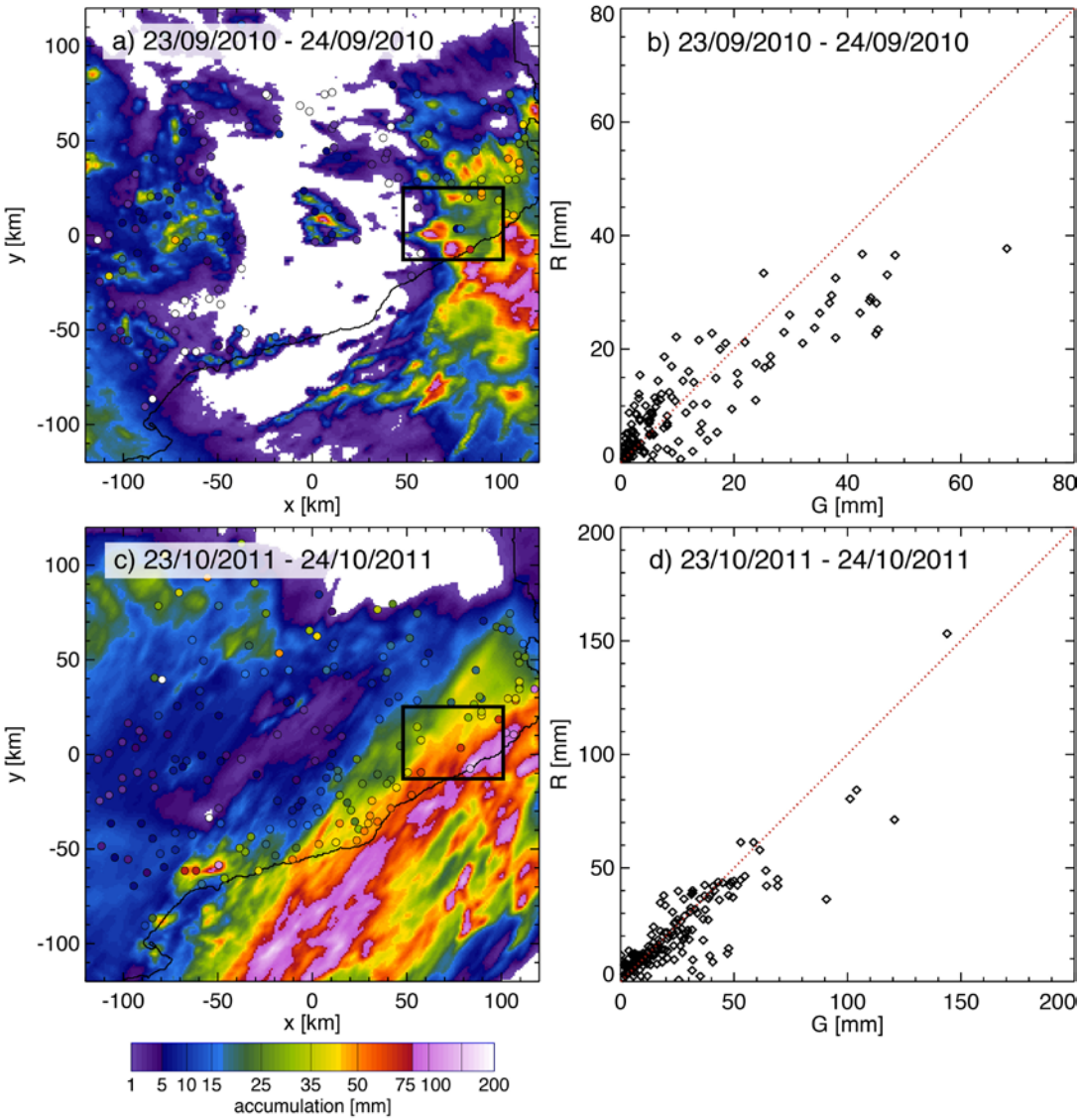

Figure 4.8 Rainfall accumulations for the two events analyzed (23-24 September 2010 and 23-24 October 2011). Left: Radar-based accumulations (the circles indicate

the accumulations observed at rain gauge locations). Right: Scatter plot between collocated radar-based accumulations and rain gauge observations.

The second case is a long-lasting situation of organized mesoscale convective systems continuously propagating over the sea together with new convection initiation. At the end of the event (24 October 2011 from 17:00 to 23:00UTC), a large-scale widespread precipitation system crossed the radar domain from west to east. The largest accumulations in the Tordera Delta case study were due to an MCS propagating parallel to the coast from SW to NE on 24 October 2011 from 00:00 to 04:00 UTC.

23-24 September 2010

In the Tordera Delta case study site, this event caused several damages with numerous flooded areas in several villages south of the Tordera Delta (mainly, Calella, Pineda, Santa Susanna, Malgrat de Mar and Palafolls) due to the overflow of the streams (usually dry) that cross these urban areas (Fig. **4.9**).

The largest observed accumulation in the area was moderate (68.1 mm in Malgrat de Mar), but most of this rain (52.3 mm) was recorded on 24 September between 15:00 and 17:00 UTC. Fire brigades reported 50 warnings in the afternoon and early evening of 24 September (coinciding with the most intense rainfall). The traffic of road N-II was stopped due to the flooding, and several camping sites in this area had to be evacuated.

Figure 4.9 Pictures of the areas flooded in Malgrat de Mar (a, b) and Pineda (c, d) on 24 September 2010. Source: El Punt Diari (a, b), www.tv3.cat (c, d).

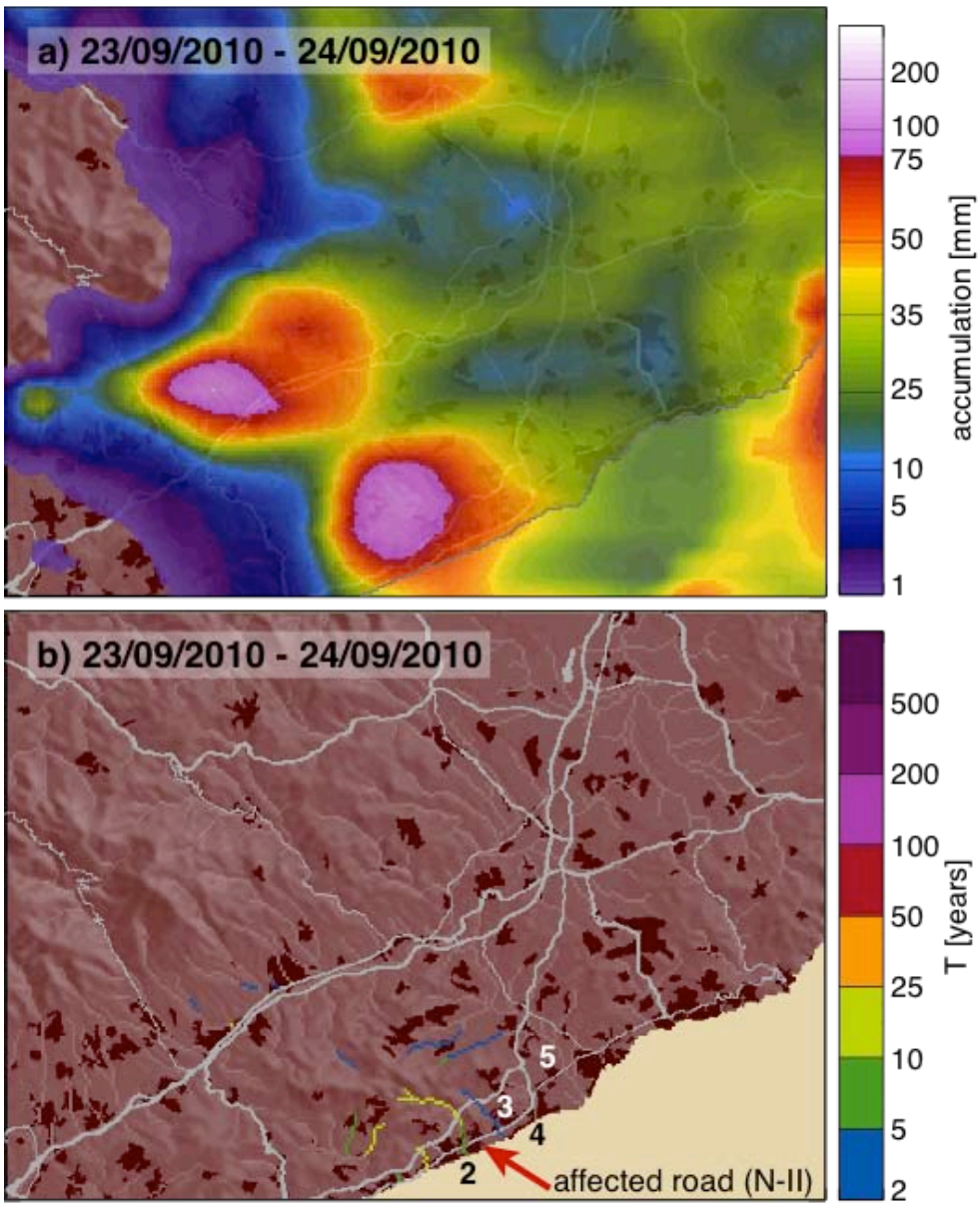

Figure 4.10 Summary of the performance of the FF-EWS module applied to the Tordera Delta case study site for the event of 23 September 2010. (a) Rainfall accumulation obtained with the radar-based QPE products. (b) Maximum return period estimated with the FF-EWS module along the event.

The FF-EWS module implemented here identified very clearly the area most affected by intense precipitation and the streams that flooded Calella, Pineda, Santa Susanna, Malgrat de Mar and Palafolls (respectively, 1-5 in Fig. **4.10**b). The most significant hazard level was triggered by a stationary convective cell that produced large rainfall amounts in the upper part of the catchments of the streams crossing the affected villages (Fig. **4.11**). The cell developed around 15:00 UTC and stayed stationary for about 2 hours, producing most of the total precipitation of the event. Afterwards, the cell weakened very fast as it moved toward the sea.

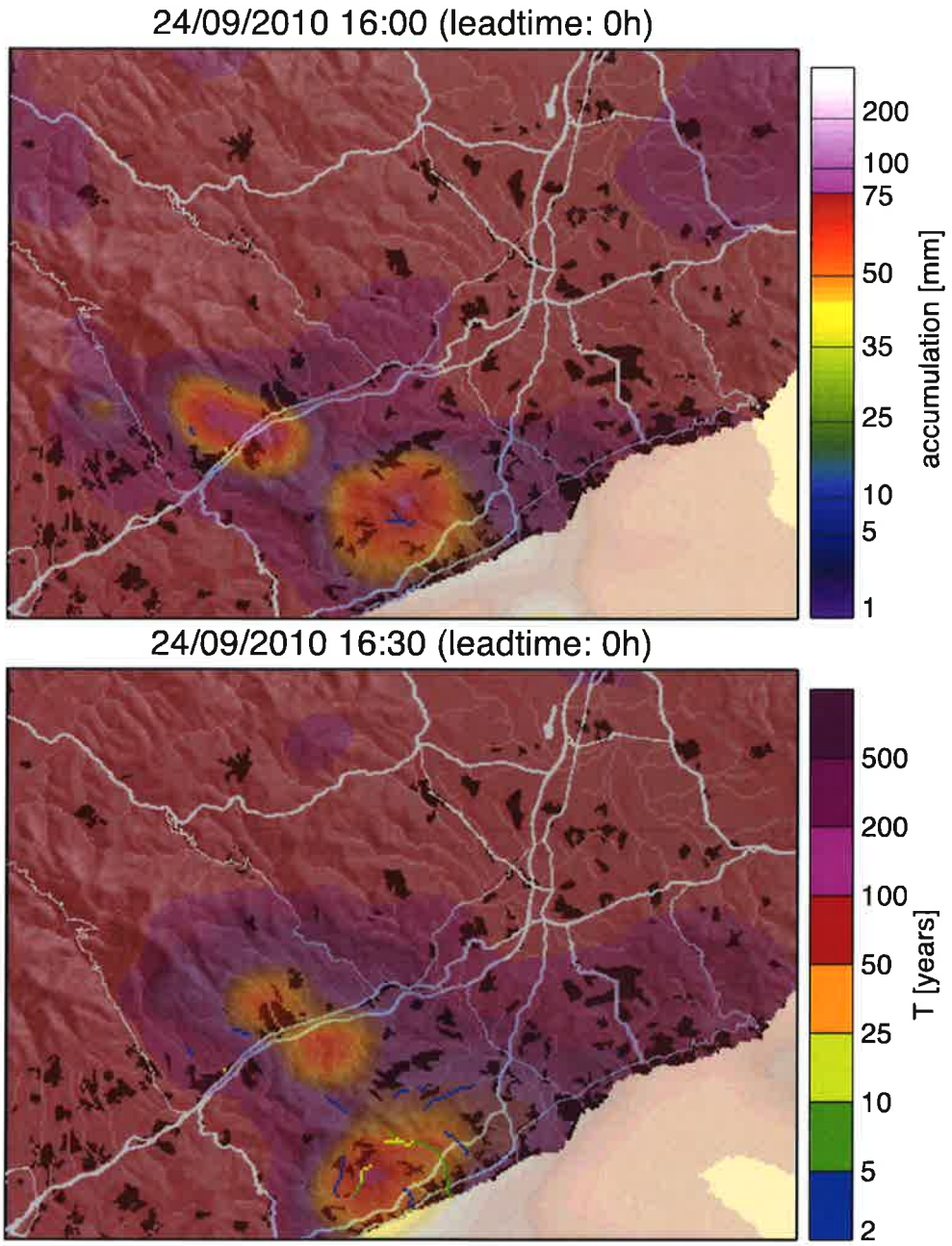

Figure 4.11 Estimated rainfall intensity and hazard level obtained with the FF-EWS module on 24 September 2010 at 16:00 (left) and 16:30 UTC (right).

23-24 October 2011

This event produced large accumulations in the area of the Tordera Delta case study site (the rain gauge in Malgrat de Mar accumulated 144 mm) and the consequences in these area were significant: Civil Protection reported 21 warnings in Malgrat de Mar Palafolls and Blanes (respectively, 1-3 in Fig. **4.12**b) on 24 October from 00:00 to 08:00 UTC of 24 October, mostly for inundated houses. Some streets were cut due to the flooding (the water level reached up to 0.50 m in the city center) and small landslides, and the power supply was cut for up to 12 hours in some neighborhoods (Fig. **4.13**).

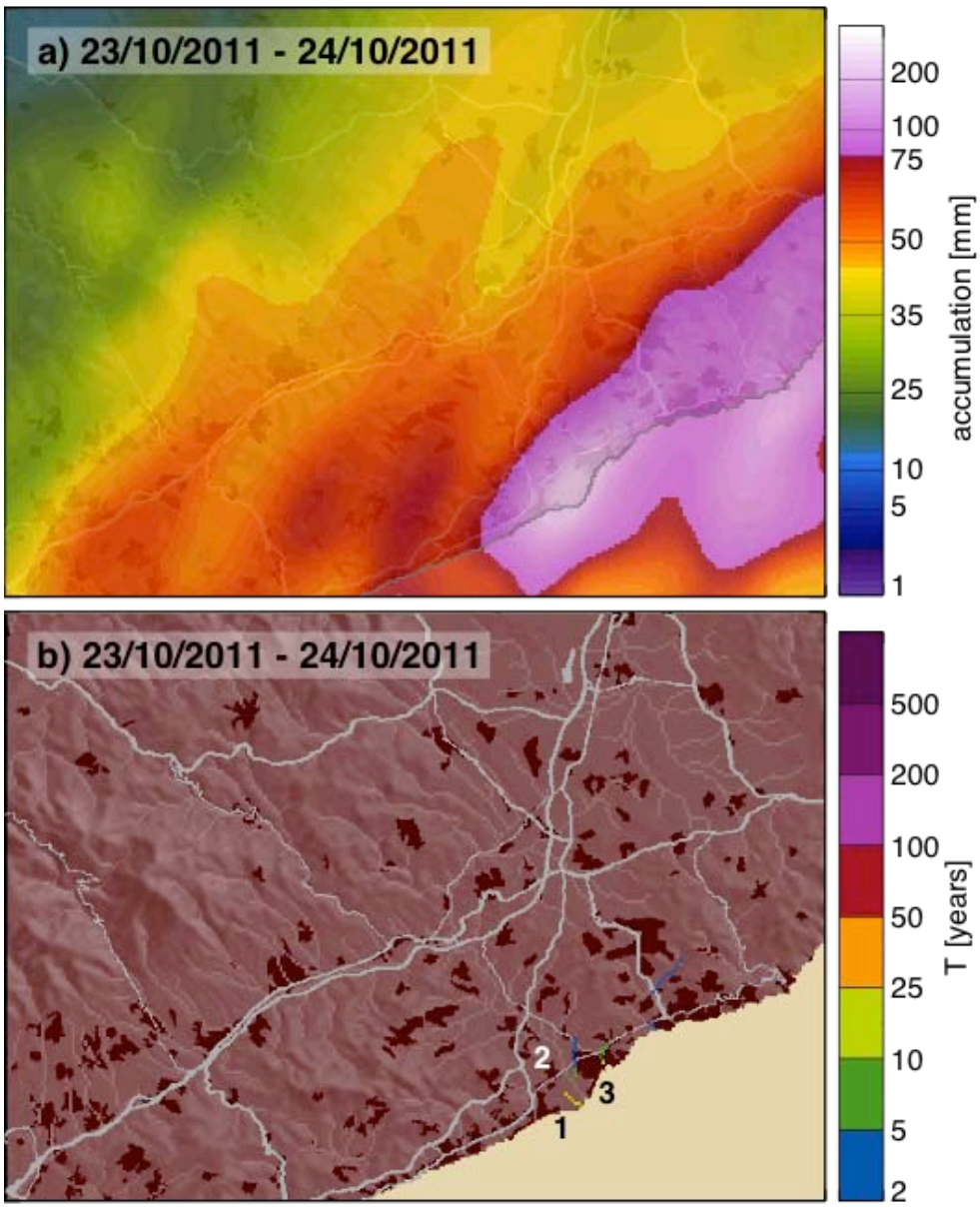

Figure 4.12 Same as Fig. **4.10**, but for the event of 23-24 October 2011.

Figure 4.13 Pictures of the areas flooded in Blanes on 24 October 2011. Source: Dolors Ruiz and Victor Catalan Casas (www.facebook.com)

The FF-EWS module identified the streams most affected by these floods (Fig. **4.12**), mostly due to the large precipitation amounts accumulated between 03:00 and 06:00 UTC associated with the intense cores of a meso-scale convective system that crossed the area producing large accumulations (Fig. **4.14**).

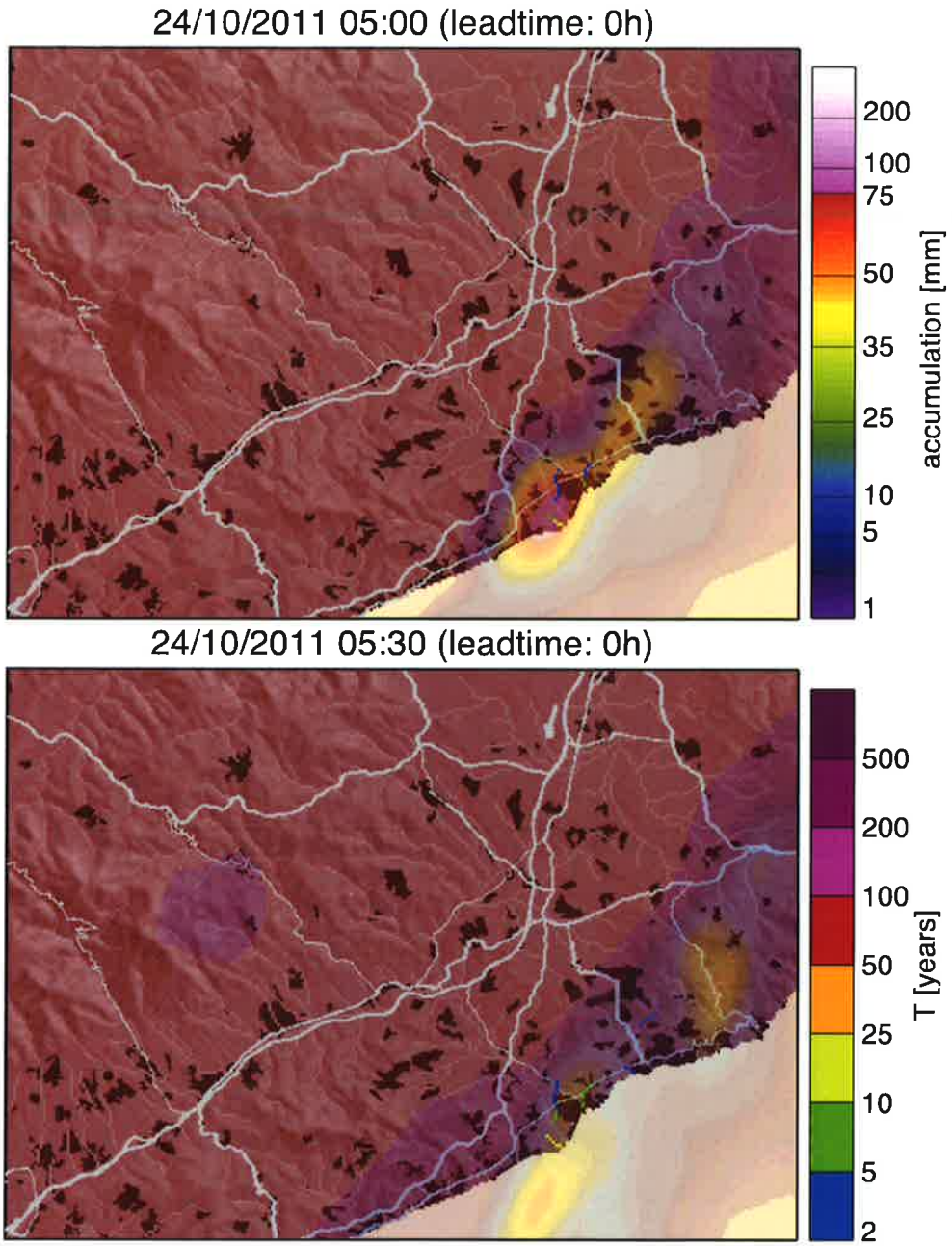

Figure 4.14 Same as Fig. **4.11**, but for 24 October 2011 at 05:00 and 05:30 UTC.

During the two analyzed events, the rainfall field showed a strong spatio-temporal variability, which has been very well captured with radar-based QPE that are the inputs of the FF-EWS module. It is also worthwhile point out at the fact that the improved resolution of the FF-EWS (200 m) allows us to identify very precisely the areas most affected by FF, which coincide remarkably well with the areas where the streams overflowed and significant damages were reported.

4.7 Recipe for the extension of the module to a new domain – requirements for its application to the Bocca di Magra case study site

As part of Work Package 5, CIMA and UPC-CRAHI will collaborate to implement the FF-EWS module described here in the Bocca di Magra case study site to demonstrate the tools developed for flash flood hazard assessment. This demonstration will enable the analysis of the multi-model approach by integrating the FF-EWS module with the systems for flash flood hazard assessment developed in the DRIHM FP7 project. The demonstration will also focus on comparing the performance of these tools using radar-based rainfall nowcasts (for forecasting times between t+0 and t+3h) and NWP rainfall forecasts (for up to a few days in advance). This section provides the recipe and data required for the implementation of the FF-EWS module described above:

Ingredients

Description	Minimum resolution
Digital Elevation Model of the study area.	500 m
Quality-controlled radar QPE products and/or blended radar-rain gauge QPE	2 km, 15 min
NWP rainfall forecasts for forecasting times up to 48 hours.	20 km, 1h
NWP rainfall forecasts downscaled with RainFARM (Rebora et al., 2006), if available	2 km, 15 min
Distributed IDF curves for the study area	10 km
Vectorial river layer (optional)	-

Recipe steps

1	Process the DEM to retrieve the drainage network of the study area
2	Implement the nowcasting algorithm to generate 3-hour precipitation forecasts over the study area.
3	Implement the module to process NWP rainfall inputs (ideally, downscaled to the resolution of radar rainfall observations).
4	Adapt the FF-EWS module to estimate the hazard level from radar-based QPE and QPF: 4.1. Computation of basin-aggregated rainfall accumulations integrated over the characteristic concentration time according to the drainage network. 4.2. Transformation of the IDF curves for point rainfall for the estimation of flash flood hazard based on basin-aggregated rainfall. 4.3. Estimation of the probability of exceedance of the observed and forecasted rainfall.

The performance of the FF-EWS module implemented in the Bocca di Magra case study site will be demonstrated over a few flash flood cases. The results will be compared with the runoff observations available at several points of the basin and with the runoff forecasts obtained with the system developed by CIMA, based on a full rainfall-runoff model using precipitation forecasts obtained from a downscaled Numerical Weather Prediction model.

4.8 Description of the exchange product to be displayed in FEWS

The flash flood hazard assessment products are displayed through the free-ware Coastal FEWS system (Deliverable 3.1) that is being developed as part of Work Package 3 of the project. With this aim, the FF-EWS module implemented in the RISC-KIT case study sites has been adapted to output NetCDF files with the results of the flash flood hazard assessment. A new NetCDF file will be created every time a new QPE map is available.

This section provides detailed description of the variables and format of the exchange NetCDF file with the outputs of the FF-EWS module. As required by the free-ware Coastal FEWS system, the NetCDF files have been built according to the CF-1.6 conventions (http://cfconventions.org). The following tables describe in detail their contents.

Attributes

Name	Type	Example
CONVENTIONS	text	'CF-1.6'
TITLE	Text	'Flash flood data'
INSTITUTION	text	'UPC-CRAHI'
SOURCE	text	'Export archive from UPC-CRAHI'
REFERENCES	text	'http://www.crahi.upc.edu'
HISTORY	text	'2015-04-15 11:13:46 UTC: created by UPC-CRAHI'
METADATA_CONVENTIONS	text	'Unidata Dataset'
SUMMARY	text	'Data created with UPC-CRAHI FF-EWS module'
DATE_CREATED	text	'2015-04-15 11:13:46 UTC'

Dimensions

Name	Values
TIME	1
Y	190
X	265

Variable 1: TIME

Name	Type	Value
STANDARD NAME	text	'time'
LONG_NAME	Text	'time'
UNITS	text	'minutes since 1970-01-01 00:00:00.0 +0000'
AXIS	text	'T'
DATA	double	SCALAR

Variable 2: Y

Name	Type	Value
STANDARD NAME	text	'latitude'
LONG_NAME	Text	'y coordinate according to WGS 1984'
UNITS	text	'degrees north'
AXIS	text	'Y'
DATA	double	ARRAY(265,190)

Variable 3: X

Name	Type	Value
STANDARD NAME	text	'longitude'
LONG_NAME	Text	'x coordinate according to WGS 1984'
UNITS	text	'degrees east'
AXIS	text	'X'
DATA	double	ARRAY(265,190)

Variable 4: CRS

Name	Type	Value
GRID_MAPPING_NAME	text	'latitude_longitude'
LONGITUDE_OF_PRIME_MERI	double	0.0000000
SEMI_MAJOR_AXIS	double	6378137.0
INVERSE_FLATTENING	double	298.25722
DATA	long	SCALAR

Variable 5: ESTIMATED_RAIN

Name	Type	Value
STANDARD NAME	text	'rainfall_rate'
LONG_NAME	Text	'30-min average rainfall rate'
UNITS	text	'm s-1'
_FILL_VALUE	float	-9.90000
COORDINATES	text	'y x'
GRID_MAPPING	text	'crs'
DATA	float	ARRAY(265,190)

Variable 6: ESTIMATED_FF_HAZARD

Name	Type	Value
STANDARD NAME	text	'return_period'
LONG_NAME	Text	'return period estimated from rainfall observations'
UNITS	text	'year'
_FILL_VALUE	float	-9.90000
COORDINATES	text	'y x'
GRID_MAPPING	text	'crs'
DATA	float	ARRAY(265,190)

Variable 7: FORECASTED_FF_HAZARD

Name	Type	Value
STANDARD NAME	text	'return_period'
LONGNAME	Text	'maximum return period estimated from rainfall forecasts'
UNITS	text	'year'
_FILL_VALUE	float	-9.90000
COORDINATES	text	'y x'
GRID_MAPPING	text	'crs'
DATA	float	ARRAY(265,190)

4.9 Summary and conclusions

This Chapter introduces the concepts used for hydrological hazard assessment in the coastal areas used as case study sites of the project prone to flash floods (the Tordera Delta area and Bocca di Magra). The approach presented here takes over the results obtained in the IMPRINTS FP7 project, in which flash flood hazard assessment was based on the basin-aggregated rainfall. This module (FF-EWS) observed rainfall based on radar QPE and can use radar-based nowcasts (for lead times up to a few hours ahead), and NWP rainfall forecasts (for up to a few days ahead). The simplification of relating the probability of occurrence of rainfall with the probability of occurrence of discharges neglects some of the hydrological processes that have an important role in the catchment response (such as the initial moisture state of the catchment). On the other hand, the main advantage of this approach is that it does not use parameters that require calibration. This is an important advantage for areas where the aim is to detect flash flood events in small and medium catchments that are often un-gauged.

The FF-EWS module has been evolved by increasing the resolution of the outputs of the module, and by improving the estimation of the probability of exceedance of the rainfall estimated at a certain moment. The latter has been based on building a climatology of rainfall fields that respect the structure of the rainfall field. This property is crucial to characterize the hydrological impact of rainfall.

The system has been implemented in the area around the Tordera Delta case study site, and its performance has been demonstrated over two rainfall events that produced significant damages in some areas of the domain. The results of the system show its skill to identify the areas most affected by floods for both cases, in part thanks to the increased resolution of the FF-EWS outputs.

This Chapter also establishes the framework for the demonstration of the flash flood warning tools to be carried out in the Bocca di Magra case study site (as part of work package 5). One of the main objectives of this demonstration will be the analysis of the multi-model approach, comparing the FF-EWS module (that will be implemented in the case study site) with the hydrological tools developed as part of the DRIHM project.

Finally, the connection between the FF-EWS module and FEWS will be done through the exchange of NetCDF files summarising the results of the flash flood hazard assessment (as detailed in section 4.8).

4.10 References

Alfieri, L., D. Velasco, and J. Thielen, 2011: Flash flood detection through a multi-stage probabilistic warning system for heavy precipitation events. *Advances in Geosciences*, **29,** 69-75.

Alfieri, L., and J. Thielen, 2012: A European precipitation index for extreme rain-storm and flash flood early warning. *Meteorological Applications*, **22**, 3-13.

Alfieri, L., P. Salamon, F. Pappenberger, F. Wetterhall, and J. Thielen, 2012: Operational early warning systems for water-related hazards in Europe. *Environmental Science & Policy*, **21,** 35-49.

Berenguer, M. and D. Sempere-Torres, 2015: Radar-based probabilistic rainfall nowcasting for flash-flood hazard assessment. In: *Handbook of Hydrometeorological Ensemble Forcasting*, Eds. Q. Duan, F. Pappenberger, J. Thielen, A. Wood, H. C. and J. C. Schaake, Publ. Springer (under review).

Berenguer, M., M. Surcel, I. Zawadzki, M. Xue, and F. Kong, 2012: The Diurnal Cycle of Precipitation from Continental Radar Mosaics and Numerical Weather Prediction Models. Part II: Intercomparison among Numerical Models and with Nowcasting. *Monthly Weather Review*, **140,** 2689-2705.

Berenguer, M., D. Sempere-Torres, and G. G. S. Pegram, 2011: SBMcast - An ensemble nowcasting technique to assess the uncertainty in rainfall forecasts by Lagrangian extrapolation, *Journal of Hydrology*, **404,** 226-240.

Berenguer, M., D. Sempere-Torres, C. Corral, and R. Sanchez-Diezma, 2006: A fuzzy logic technique for identifying nonprecipitating echoes in radar scans. *Journal of Atmospheric and Oceanic Technology*, **23,** 1157-1180.

Berenguer, M., C. Corral, R. Sanchez-Diezma, and D. Sempere-Torres (2005), Hydrological validation of a radar-based nowcasting technique, *Journal of Hydrometeorology*, **6**, 532-549.

Corral, C., Velasco, D., Forcadell, D., & Sempere-Torres, D., 2009: Advances in radar-based flood warning systems. The EHIMI system and the experience in the Besòs flash-flood pilot basin. In: *Flood Risk Management: Research and Practice*, Ed. P. Samuels, S. Huntington, W. Allsop, and J. Harrop. Taylor & Francis, London, UK, 1295-1303.

Delrieu, G., J. D. Creutin, and H. Andrieu, 1995: Simulation of Radar Mountain Returns Using a Digitized Terrain Model. *Journal of Atmospheric and Oceanic Technology*, **12,** 1038-1049.

Duchon, J. (1977) Splines minimizing rotation-invariant semi-norms in Solobev spaces, In: *Construction Theory of Functions of Several Variables,* Springer, Berlin.

Fabry, F., A. Bellon, M. R. Duncan, and G. L. Austin (1994), High-Resolution Rainfall Measurements by Radar for Very Small Basins - the Sampling Problem Reexamined, *Journal of Hydrology*, **161**, 415-428.

Franco, M., R. Sánchez-Diezma, and D. Sempere-Torres, 2006: Improvements in weather radar rain rate estimates using a method for identifying the vertical profile of reflectivity from volume radar scans. *Meteorologische Zeitschrift*, **15,** 521-536.

Franco, M., R. Sánchez-Diezma, D. Sempere-Torres, and I. Zawadzki, 2008: Improving radar precipitation estimates by applying a VPR correction method based on separating precipitation types. Preprints, *5th European Conference on Radar in Meteorology and Hydrology*, Helsinki, Finland, P14.16.

Gaume, E., and Coauthors, 2009: A compilation of data on European flash floods. *J Hydrol*, **367,** 70-78.

Germann, U., G. Galli, M. Boscacci, and M. Bolliger, 2006: Radar precipitation measurement in a mountainous region. *Quarterly Journal of the Royal Meteorological Society*, **132,** 1669-1692.

Germann, U., I. Zawadzki, and B. Turner, 2006: Predictability of precipitation from continental radar images. Part IV: Limits to prediction. *Journal of the Atmospheric Sciences*, **63,** 2092-2108.

Guillot, P. and Duband, D.,1967: La méthode du Gradex pour le calcul de la probabilité des crues à partir les pluies. AISH Publ. 84: 560-569.

Li, L., W. Schmid, and J. Joss, 1995: Nowcasting of Motion and Growth of Precipitation with Radar over a Complex Orography. *Journal of Applied Meteorology*, **34,** 1286-1300.

O'Callaghan, J. F., and D. M. Mark, 1984: The extraction of drainage networks from digital elevation data. *Computer Vision, Graphics, and Image Processing*, **28,** 323-344.

Sánchez-Diezma, R., D. Sempere-Torres, J.-D. Creutin, I. Zawadzki, and G. Delrieu, 2001: An improved methodology for ground clutter substitution based on a pre-classification of precipitaion types. Preprints, *30th International Conference on Radar Meteorology*, Munich, Germany, Amer. Meteor. Soc., 271-273.

Rebora, N., L. Ferraris, J. von Hardenberg, and A. Provenzale, 2006: RainFARM: Rainfall Downscaling by a Filtered Autoregressive Model. *Journal of Hydrometeorology*, **7,** 724-738.

Sempere-Torres, D., 2001: Peculiarities of rainfall runoff modeling in Mediterranean basins. In: *Radar hydrology for real time flood forecasting*, Ed. R. J. Griffith, I. D. Cluckie, G. L. Austin, and D. Han, Publ. Office for Official Publications of the European Communities, 235-243.

Sempere-Torres, D., D. Velasco, and M. Berenguer, 2010: Chapter 4.2: Improving risk management for flash floods and debris flow events. In: *The water framework directive: Action programmes and adaptation to climate change*, Publ. Royal Society of Chemistry, 139-169.

Sempere-Torres, D., D. Velasco-Montes, M. Berenguer et al., 2011: Improving risk management for flash floods and debris flow events. In *The water framework directive: Action programmes and adaptation to climate change*, Ed. P. Quevauviller, U. Borchers, K C. Thompson, T. Simonart, Publ. Royal Society of Chemistry, 139-169.

Silvestro, F., and N. Rebora, 2014: Impact of precipitation forecast uncertainties and initial soil moisture conditions on a probabilistic flood forecasting chain. *Journal of Hydrology*, **519,** 1052-1067.

Velasco-Forero, C. A., D. Sempere-Torres, E. F. Cassiraga, and J. J. Gómez-Hernández, 2009: A non-parametric automatic blending methodology to estimate rainfall fields from rain gauge and radar data. *Advances in Water Resources*, 32, 986-1002.

Versini, P. A., Berenguer, M., Corral, C., & Sempere-Torres, D., 2014: An operational flood warning system for poorly gauged basins: demonstration in the Guadalhorce basin (Spain), *Natural Hazards*, 71, 1355-1378.

Villarini, G., and W. F. Krajewski, 2009: Review of the Different Sources of Uncertainty in Single Polarization Radar-Based Estimates of Rainfall. *Surveys in Geophysics*, **31,** 107-129.